Feature Analysis Methods for Intelligent Breast Imaging Parameter Optimisation using CMOS Active Pixel Sensors

Colin Esbrand

Dept. Medical Physics & Bioengineering
University College London

Submitted for Degree of Doctor of Philosophy

2009

I, Colin Esbrand, confirm that the work presented in this thesis is my own. Where information has been derived from other sources, I confirm that this has been indicated in the thesis.

Abstract

This thesis explores the concept of real time imaging parameter optimisation in digital mammography using statistical information extracted from the breast during a scan. Transmission and Energy dispersive x-ray diffraction (EDXRD) imaging were the two very different imaging modalities investigated. An attempt to determine if either could be used in a real time imaging system enabling differentiation between healthy and suspicious tissue regions was made. This would consequently enable local regions (potentially cancerous regions) within the breast to be imaged using optimised imaging parameters.

The performance of possible statistical feature functions that could be used as information extraction tools were investigated using low exposure breast tissue images. The images were divided into eight regions of interest, seven regions corresponding to suspicious tissue regions marked by a radiologist, where the final region was obtained from a location in the breast consisting solely of healthy tissue.

Results obtained from this investigation showed that a minimum of 82% of the suspicious tissue regions were highlighted in all images, whilst the total exposure incident on the sample was reduced in all instances. Three out of the seven (42%) intelligent images resulted in an increased contrast to noise ratio (CNR) compared to the conventionally produced transmission images. Three intelligent images were of similar diagnostic quality to their conventional counter parts whilst one was considerably lower.

EDXRD measurements were made on breast tissue samples containing potentially cancerous tissue regions. As the technique is known to be able to

distinguish between breast tissue types, diffraction signals were used to produce images corresponding to three suspicious tissue regions consequently enabling pixel intensities within the images to be analysed. A minimum of approximately 70% of the suspicious tissue regions were highlighted in each image, with at least 50% of each image remaining unsuspicious, hence was imaged with a reduced incident exposure.

Table of Content

Abstract 3

List of Figures 10

List of Tables 14

List of Abbreviations 17

Acknowledgements 18

Chapter One 19

Introduction and background to Intelligent Imaging 19

1.1 Introduction 20

1.2 Digital X-ray Mammography 22

1.2.1 Commercially available FFDM systems 23

1.2.2 Automated Exposure Control (AEC) 27

1.2.3 Automated detection: Computer Aided-Detection 29

1.3 Energy dispersive x-ray diffraction 32

1.3.1 Rayleigh Scatter Imaging 32

1.3.2 Coherent Scatter 34

1.3.3 Previous medical EDXRD Work 36

1.3.3.1 Breast tissue 36

1.3.3.4 Bone 37

1.4 X-ray detection systems 39

1.4.1 CMOS APS 40

1.5 The Intelligent Imaging Sensor project 43

1.6 The aim and scope of this thesis 44

Chapter Two 45

Experimental systems and their performance evaluation 45

2.1 Overview 46

2.2 The Intelligent Imaging System (I-ImaS) 47

2.2.1 I-ImaS system components 48

2.2.1.1 The I-ImaS sensors 49

2.2.1.2 The data acquisition card 50

2.2.1.3 The tissue carrying plate stage (TCP) 51

2.2.1.4 The x-ray beam attenuation filters 52

2.2.1.5 The motion control system (MCS) 54

2.3 EDXRD system components 54

2.3.1 The X-ray unit 55

2.3.2 Photon detection 55

2.3.4 EDXRD system optics 56

2.4 EDXRD system configuration 56

2.5 Summary 58

2.6 Specimen evaluation: Radiologist's analysis 60

2.7 X-ray characterisation of the I-ImaS sensors 62

2.7.1 X-ray response 63

2.7.2 Modulation transfer function (MTF) 63

2.7.3 Noise Power Spectrum (NPS) 66

2.7.4 Detective quantum efficiency (DQE) 68

2.8 Materials and Methods 69

2.8.1 X-ray response 69
2.8.2 MTF 70
2.8.3 NPS 70
2.9 Results 71
2.9.1 X-ray response 71
2.9.2 MTF 72
2.9.3 NPS 73
2.9.4 DQE 76
2.10 Summary 77

Chapter Three 79
Feature extraction using statistical feature functions & EDXRD 79
3.1 Introduction 80
3.2 Materials 82
3.2.1 Database images 82
3.2.2 Statistical feature functions for abnormality detection algorithm 83
3.2.3 Tissue differentiation: Threshold levels 85
3.3 Testing of the statistical feature functions 86
3.3.1 Preliminary feature function testing: Database images 86
3.3.2 Results of preliminary investigation 88
3.4 Imaging parameter modulation 101
3.5 Feature extraction 103
3.5.1 Transmission imaging 103
3.6 Working limitations of the combined feature function 105
3.7 Effect of the scanning ROI size used for statistical analysis 125

3.8 Feature function threshold optimisation 129
3.8.1 $SynF_1$ threshold optimisation 129
3.8.2 $SynF_2$ threshold optimisation 132
3.9 Summary 134
3.10 EDXRD Introduction 135
3.11 Methodology 136
3.11.1 Diffraction profiles 136
3.11.2 EDXRD imaging 138
3.11.3 Data analysis procedure 140
3.12 Setup optimisation 141
3.12.1 Threshold determination 141
3.12.2 Statistical quality of data 144
3.12.3 The effect of x-ray beam collimation size 147
3.13 Stepping ROI size 155
3.14 Summary 160

Chapter Four 162
Intelligent Images 162
4.1 Intelligent Image production 163
4.2 Combined feature function results 164
4.3 Summary 171
4.4 EDXRD results 172
4.5 Comparison of both methods 177
4.6 Summary 180

Chapter Five 181
Conclusion 181
5.1 Overview 182
5.2 Intelligent imaging based on low exposure scout images 183
5.3 EDXRD based intelligent imaging 185
5.4 Conclusion 186
Reference List 189

List of Figures

Figure 1.1 Illustration of the characteristic peaks of pure adipose tissue and cancerous tissue. 33
Figure 1.2 Comparison of three similar diffraction peaks pertaining to three different tissue types found within the breast. 37
Figure 1.3 Schematic of basic three transistor (3T) CMOS APS pixel circuitry. 42
Figure 2.1 Schematic illustrating functionality of the prototype I-ImaS imaging system. 47
Figure 2.2 The data acquisition components used by the I-ImaS system. 49
Figure 2.3 Tissue carrying plate used to scan breast samples across sensor arrays. 51
Figure 2.4 I-ImaS x-ray beam attenuation filter used to optimise the exposure incident on the breast sample. 53
Figure 2.5 Laboratory based EDXRD system setup used to acquire diffraction profiles of tissue samples. 55
Figure 2.6 Schematic illustrating the geometry of the EDXRD system used in this investigation. 57
Figure 2.7 Illustration of intelligent concept using low exposure scout image to derive system intelligence (option 1), and EDXRD concept (option 2). 59
Figure 2.8 Photographs of the excised breast samples used to simulate the I-ImaS intelligent images. 61
Figure 2.9 Breast tissue regions marked as suspicious by radiologist. 62
Figure 2.10 Illustration of perpendicular integrals for slit normalisation procedure correcting for slit imperfections. 65
Figure 2.11 Determination of the traverse profile maximum along slit length 65
Figure 2.12 The normalised oversampled LSF of the I-ImaS sensor 66
Figure 2.13 Sensor x-ray response 72
Figure 2.14 The presampled MTF plot of the I-ImaS sensor coupled to a 100µm structured CsI:TI scintillator. 73
Figure 2.15 2-D NPS for all exposures investigated 75

Figure 2.16 Comparison of 1-D normalised noise power spectrum obtained at all exposure settings investigated.....76
Figure 2.17 The DQE of I-ImaS sensor 77
Figure 3.1 Schematic of stepping ROI. 87
Figure 3.2 Strip of database mammogram containing a microcalcification cluster embbed in adipose tissue.....89
Figure 3.3 Strip of database mammogram containing a circumscribed lesion embbed in adipose tissue, graphs depict results of the statistical feature functions.....90
Figure 3.4 Illustration of a mammogram containing a benign circumscribed mass embedded in adipose tissue downloaded from MIAS database 94
Figure 3.5 Results of statistical analysis yielded by $SynF_1$ and $SynF_2$ corresponding to figure 3.4. 95
Figure 3.6 Illustration of a mammogram containing a benign microcalcification embedded in fatty glandular tissue downloaded from MIAS database 97
Figure 3.7 Results of statistical analysis yielded by $SynF_1$ and $SynF_2$ corresponding to figure 3.6. 98
Figure 3.8 Illustration of a mammogram containing a benign circumscribed mass embedded in fatty glandular tissue downloaded from MIAS database 99
Figure 3.9 Results of statistical analysis yielded by $SynF_1$ and $SynF_2$ corresponding to figure 3.8. 100
Figure 3.10 Simplified schematic illustrating the experimental setup used to acquire x-ray images of breast samples one and two using the I-ImaS system. 104
Figure 3.11 Regions of interest obtained from breast samples one and two used to evaluate the abnormality detection algorithm. 107
Figure 3.12 Contrast of sample 1 sections 1 and 2 at each incident exposure.....109
Figure 3.13 Contrast of sample 1 sections 3 and 4 at each incident exposure.....110
Figure 3.14 Regions corresponding to sample 1 section 5 at each incident exposure...111
Figure 3.15 Contrast of sample 2 section 1 at each incident exposure 111
Figure 3.16 Contrast of sample 2 sections 2 and 3 at each incident exposure.....112

Figure 3.17 Regions of tissue flagged as suspicious by the combined feature function corresponding to figure 3.12 114
Figure 3.18 Regions of tissue flagged as suspicious by the combined feature function corresponding to figure 3.13 117
Figure 3.19 Regions of tissue flagged as suspicious by combined feature function corresponding to figure 3.14. 119
Figure 3.20 Regions of tissue flagged as suspicious by the combined feature function corresponding to figure 3.15. 121
Figure 3.21 Regions of tissue flagged as suspicious by the combined feature function corresponding to figure 3.16. 123
Figure 3.22 Diffraction profile obtained from suspicious tissue region within sample one demonstrating the effect of tissue superimposition within the scattering volume. 137
Figure 3.23 EDXRD image of an ROI located within breast sample one obtained using a solid angle of 0.23msr. 140
Figure 3.24 Schematic of stepping ROI used in EDXRD. 141
Figure 3.25 EDXRD image of sample 1, 2a and 2b 142
Figure 3.26 Effect the number of photon counts has on visibility of suspicious tissue region in sample one 145
Figure 3.27 Effect the number of photon counts has on pixel column intensity. 146
Figure 3.28 EDXRD images of sample 1 obtained using a solid angle of 0.23,0.43 and 0.98msr 149
Figure 3.29 EDXRD images of sample 2a obtained using a solid angle of 0.23,0.43 and 0.98msr 151
Figure 3.30 Column intensity profile of sample 2a 152
Figure 3.31 EDXRD images of sample 2b obtained using a solid angle of 0.23,0.43 and 0.98msr 154
Figure 3.32 EDXRD images of sample 1 corresponding to the area's analysed by three different scanning ROI sizes 156

Figure 3.33 EDXRD images of sample 2a corresponding to the area's analysed by three different scanning ROI sizes 157
Figure 3.34 EDXRD images of sample 2b corresponding to the area's analysed by three different scanning ROI sizes 157
Figure 4.1 Exposure maps obtained from transmission scout images 165
Figure 4.2 Transmission I-ImaS intelligent images. 167
Figure 4.3 Conventional images corresponding to figure 4.2. 167
Figure 4.4 Line profiles across conventional and I-ImaS intelligent image 171
Figure 4.5 Exposure maps obtained fron EDXRD image analysis 173
Figure 4.6 EDXRD Intelligent images 175
Figure 4.7 Convetional transmission images corresponding to EDXRD regions 176
Figure 4.8 Feedback technique comparison 176

List of Tables

Table 1.1 Comparison of the differing specifications possessed by eleven commercially available DM systems. 25

Table 2.1 Physical characteristics of an individual I-ImaS sensor where x-ray sensitivity is increased using a scintillator. 50

Table 2.2 I-ImaS x-ray beam attenuation filter construction for use with a 30kV, W anode source. 53

Table 3.1 Results of the combined feature function analysis obtained from database mammograms. 91

Table 3.2 Results obtained from Sample 1 section 1 analysis illustrating proportion of tissue highlighted as suspicious for a given level of exposure. 115

Table 3.3 Results obtained from Sample 1 section 2 analysis illustrating proportion of tissue highlighted as suspicious for a given level of exposure. 115

Table 3.4 Results obtained from Sample 1 section 3 analysis illustrating proportion of tissue highlighted as suspicious for a given level of exposure. 118

Table 3.5 Results obtained from Sample 1 section 4 analysis illustrating proportion of tissue highlighted as suspicious for a given level of exposure. 118

Table 3.6 Results obtained from Sample 1 section 5 analysis illustrating proportion of tissue highlighted as suspicious for a given level of exposure. 120

Table 3.7 Results obtained from Sample 2 section 1 analysis illustrating proportion of tissue highlighted as suspicious for a given level of exposure. 121

Table 3.8 Results obtained from Sample 2 section 2 analysis illustrating proportion of tissue highlighted as suspicious for a given level of exposure. 124

Table 3.9 Results obtained from Sample 2 section 3 analysis illustrating proportion of tissue highlighted as suspicious for a given level of exposure. 124

Table 3.10 Performance characteristics of scanning ROI size investigation for sample 1 section 1 using an incident exposure of 19.0μCkg^{-1}. 126

Table 3.11 Performance characteristics of scanning ROI size investigation for sample 1 section 2 using an incident exposure of 19.0μCkg^{-1}.....126
Table 3.12 Performance characteristics of scanning ROI size investigation for sample 1 section 3 using an incident exposure of 19.0μCkg^{-1}.....126
Table 3.13 Performance characteristics of scanning ROI size investigation for sample 1 section 4 using an incident exposure of 19.0μCkg^{-1}.....126
Table 3.14 Performance characteristics of scanning ROI size investigation for sample 2 section 1 using an incident exposure of 19.0μCkg^{-1}.....127
Table 3.15 Performance characteristics of scanning ROI size investigation for sample 2 section 2 using an incident exposure of 19.0μCkg^{-1}.....127
Table 3.16 Performance characteristics of scanning ROI size investigation for sample 2 section 3 using an incident exposure of 19.0μCkg^{-1}.....127
Table 3.17 Results obtained from sample 1 section 1 depicting effect of threshold ROI size analysis for SynF1 using an incident exposure of 19.0μCkg^{-1}.....129
Table 3.18 Results obtained from sample 1 section 3 depicting effect of threshold ROI size analysis for SynF1 using an incident exposure of 19.0μCkg^{-1}.....130
Table 3.19 Results obtained from sample 2 section 1 depicting effect of threshold ROI size analysis for SynF1 using an incident exposure of 19.0μCkg^{-1}.....130
Table 3.20 Results obtained from sample 2 section 2 depicting effect of threshold ROI size analysis for SynF1 using an incident exposure of 19.0μCkg^{-1}.....130
Table 3.21 Results obtained from sample 1 section 1 depicting effect of SynF2 threshold analysis using an incident exposure of 19.0μCkg^{-1}.....132
Table 3.22 Results obtained from sample 1 section 2 depicting effect of SynF2 threshold analysis using an incident exposure of 19.0μCkg^{-1}.....133
Table 3.23 Results obtained from sample 1 section 3 depicting effect of SynF2 threshold analysis using an incident exposure of 19.0μCkg^{-1}.....133
Table 3.24 Results obtained from sample 1 section 4 depicting effect of SynF2 threshold analysis using an incident exposure of 19.0μCkg^{-1}.....133
Table 3.25 Results obtained from sample 2 section 1 depicting effect of SynF2 threshold analysis using an incident exposure of 19.0μCkg^{-1}.....133

Table 3.26 Results obtained from sample 2 section 2 depicting effect of SynF2 threshold analysis using an incident exposure of 19.0μCkg^{-1}.....134
Table 3.27 Results obtained from sample 2 section 3 depicting effect of SynF2 threshold analysis using an incident exposure of 19.0μCkg^{-1}.....134
Table 3.28 Effect of threshold settings on breast sample 1 suspicious tissue detection. 143
Table 3.29 Effect of threshold settings on breast sample 2a suspicious tissue detection. 143
Table 3.30 Effect of threshold settings on breast sample 2b suspicious tissue detection. 143
Table 3.31 Experiment results obtained from sample one depicting the statistical quality of the four images investigated. 144
Table 3.32 Effect of the statistical quality of data used to obtain EDXRD images of sample 1 on abnormality detection. 147
Table 3.33 Effect solid angle has on abnormality detection within sample one. 150
Table 3.34 Effect solid angle has on abnormality detection within sample 2a. 153
Table 3.35 Effect solid angle has on abnormality detection within breast sample 2b. ..153
Table 3.36 Performance characteristics of three different ROI sizes used to investigate the suspicious tissue region within sample 1. 159
Table 3.37 Performance characteristics of three different ROI sizes used to investigate the suspicious tissue region within sample 2a. 159
Table 3.38 Performance characteristics of three different ROI sizes used to investigate the suspicious tissue region within sample 2b. 159
Table 4.1 Image quality and incident exposure results obtained from breast samples one and two intelligent images obtained using a scout exposure of 19.0μCkg^{-1}. 169

List of Abbreviations

AEC	Automatic Exposure Control
CAD	Computer Aided Detection
CCD	Charged Coupled Device
CMOS APS	Complimentary Metal Oxide Semi-conductor Active Pixel Sensor
CNR	Contrast to Noise Ratio
CmI-TI	Thalium dope Ceasium Iodide
DAQ	Data Acquisition System
DN	Digital Number
DQE	Detective Quantum Efficiency
EDXRD	Energy Dispersive X-Ray Diffraction
EUS	End User Survey
FFDM	Full Field Digital Mammography
FPGA	Field Programmable Gate Array
I-Imas	Intelligent Imaging System
IMRT	Intensity Modulated Radio Therapy
LAXS	Low Angle X-Ray Scatter
MAPS	Monolithic Active Pixel Sensor
MCA	Multi Channel Analyser
MCS	Motion Control System
MTF	Modulation Transfer Function
NNPS	Normalised Noise Power Spectrum
NPS	Noise Power Spectrum
PMMA	Polymethyl-methacrylate
SFM	Screen Film Mammography
SynF	Synthetic Feature Function
TCP	Tissue Carrying Plate
TV	Threshold Value

Acknowledgements

I sincerely wish to thank my principal supervisor Professor Robert Speller and Dr Gary Royle for the endless levels of support, advice and encouragement they have bestowed both academically, and as friends over the duration of the course.

I greatly appreciate the support of the Radiation Physics group as the advice sought was priceless. In particular, thanks go to Dr Marinos Metaxas as he always brought a smile to my face (and still does!) regardless of the circumstances. Dr Emily Cook and Dr Costas Arvanitis as their expertise aided me greatly; Dr Sarah Bohndiek as her endless support through discussion was inspiring. Mr Ben Price and Mr Walid Ghoggali for all the laughs, long talks and the mutual moral support provided over hot chocolates. Dr Alassandro Olivo and Dr Jennifer Griffiths for all their suggestions which made my work stronger.

Finally, I would like to say a very special thank you to my family and fiancée Janine Griffith as without their constant stream of love, I could not have dreamed of completing such a task.

Chapter One

Introduction and background to Intelligent Imaging

1.1 Introduction

Breast cancer is the most commonly diagnosed cancer in the UK among women. More than 45,000 women and approximately 300 men are diagnosed with the disease each year (Cancer Research UK). The NHS Breast Screening Programme (NHSBSP) initiated by Professor Sir Patrick Forrest began screening in 1988 and has since screened more than 19 million women. It is estimated that 1.5 million women are now screened in the UK annually (NHSBSP). Cancer Research UK has reported an increase of approximately 50% in breast cancer incidence rates in Britain between the period 1977-2006 where a 14% increase was seen over the last 10 years alone. This indicates that the screening programme is beneficial, as prior to this, many cancers were going undetected. Also, this implies that, since the introduction of full field digital mammography (FFDM), approximately 10 years ago, cancer detection rates have increased further.

The benefits of using FFDM compared to screen film mammography (SFM) are not only reflected through the results yielded from research groups and screening programmes which were setup to compare the two methods (Lewin et al (2002), Pisano et al (2005), Skaane and Skjennald (2004)), but also through its rapid implementation into routine screening. In December 2006, FFDM units made up 15.0% of the accredited mammography units in use in the USA; this increased to 50.3% by April 2009 (Food and Drug Administration).

Unlike SFM where image acquisition, processing and displaying are all coupled together, FFDM enables the separation of each of these steps therefore allowing the optimisation of each (James et al (2004) and Monnin et al (2007)). As a result, FFDM has the advantages of having a wider dynamic range enabling higher contrast resolution, higher quantum efficiency, allows visual adjustments

of the image for viewing (such as brightness, contrast and black/white inversion), instantaneous image recovery greatly reducing processing time, as well as allowing rapid distribution of images between locations worldwide (Cooper III et al (2003), Parikh (2005) and Fischer et al (2006)). As the images are of digital format, storage of high volumes of images becomes less cumbersome therefore space efficient.

As one would expect, full digitisation of mammographic imaging potentially acts to revolutionise the imaging procedure as a whole, providing a platform for advanced applications. The use of computer aided diagnosis/detection (CAD) has been under investigation ever since the introduction of 'digital mammography' (Chan et al (1988), Vyborny and Giger (1994)); where now, it clinically acts as an aid to the radiologist, potentially enabling the elimination of the need for double readings hence the need for the presence of a second reader (Lauria et al (2005)). The use of automated exposure control (AEC) is now a standard means of image optimisation where the imaging parameters are automatically selected based on pre-scan information obtained using a digital detector (Williams et al (2008)). Also, the movement from analogue to digital has enabled mammography to take advantage of image enhancement techniques once foreign to the speciality. Modalities currently under investigation include contrast enhanced dual-energy subtraction mammography, which is used to detect angiogenesis in cancerous tissue (Dromain et al (2006), Dromain et al (2009)), dual-energy subtraction mammography which enables the removal of obstructing tissue structures from an image using a weighted subtraction method (Lemacks et al (2002), Brandan. M-E and Ramírez-R (2006)), breast tomosynthesis, a current modality which promotes 3D mapping of tissue structures as opposed to the currently available 2D mapping used by FFDM imagers. This consequently reduces tissue overlap (Sechopoulos et al (2007),

Andersson et al (2008), Sechopoulos and Ghetti (2009)) enabling a more accurate diagnosis to be made. Techniques such as energy dispersive and angular dispersive x-ray diffraction (ADXRD) are also under investigation (Taibi et al (2003), Hermann et al (2002)). All techniques attempt to further increase cancer detection rates whilst decreasing the rate of false-positives hence unnecessary biopsies and recalls.

1.2 Digital X-ray Mammography

Until recently, conventional SFM has been the modality of choice for screening programmes across the world (Yamada (2003)). However, as more and more FFDM systems appear on the market, it becomes apparent that FFDM is to be the next step in the evolution of x-ray mammography facilitating the realisation of the 'digital hospital'.

Over the last decade, a large quantity of research has been undertaken comparing FFDM to SFM in an attempt to determine whether FFDM increases cancer detection rates among women. A majority of the comparison studies published involve large population based breast screening programmes where women have been invited to attend the programme having been chosen from a specific age group, usually between 45-69 years. They have then been randomly selected for screening using either SFM or FFDM (Lewin et al (2001)). A large majority of the results from these clinical screening programmes (Osbenauer et al (2002), Vigeland et al (2007), Skaane and Skjennald (2004)) as well as others including laboratory based investigations (Berns et al (2002)), consistently indicate that FFDM increases cancer detection and characterisation amongst post-menopausal (aged 50-69) women whilst providing comparable detection

rates for women aged 45-49 (Skaane and Skjennald (2004) and Pisano et al (2005)).

Recently, Vigeland et al (2007) conducted a population-based screening programme in order to compare currently available FFDM units to SFM. The results indicated a higher breast cancer detection rate was achievable when implementing FFDM as opposed to SFM. It has become apparent that over the years as a result of continuous technological development, cancer detection rates are increasing and it is inevitable that in the near future statistical significance will be established clearly making FFDM the new standard for mammography.

As the literature concludes that the diagnostic accuracies of FFDM and SFM are similar, initially it may be thought that making the switch over from an analogue system to a digital one would have little benefit and prove costly. However, this would be a naive assumption as FFDM offers several significant advantages over SFM. The ability to greatly facilitate new applications increasing cancer detection rates by overcoming problems seen with conventional SFM such as contrast limitations, tissue obstructions etc are all made possible by FFDM and are currently under investigation (Fass (2008), Reiser et al (2006), Kappadath and Shaw (2004)).

1.2.1 Commercially available FFDM systems

There are currently at least eleven FFDM systems commercially available which all differ in performance and specifications (KCARE (2005), Fischer et al (2006), Monnin et al (2007), Williams et al (2008) and Ghetti et al (2008)). These include a Scanning Phosphor Charged-Coupled Device (CCD) system, Flat-Panel Phosphor

system and a Flat-Panel amorphous Selenium (a-Se) system. Each detector makes use of either an indirect x-ray detection method where a scintillator is implemented in an attempt to improve the detector x-ray sensitivity or a direct method where x-rays are converted directly to charge eliminating the light conversion process. In doing so an increase in performance is seen (Pisano and Yaffe (2005)). Table 1.1 compares the specifications of FFDM units.

A large percentage of the published screening programmes used in evaluating FFDM have been undertaken using a Flat-Panel phosphor system namely the Senographe 2000D manufactured by General Electric Medical systems (GE) (Fischer et al (2002), Osbenauer et al (2002), Obenauer (2003), Yamada (2003), and Skaane and Skjennald (2004)). It is thought that this system was extensively used as radiologists quickly became familiar with it due to it being the first FFDM system to receive Food and Drug Administration (FDA) approval, hence making it readily available (Fischer et al (2002)). The more recent introduction of the Senographe DS and Senographe Essential which, both consist of a similar detector design whilst incorporating additional improved features such automated exposure control (AEC) and a larger imaging area, have helped to ensure the implementation of over 1500 systems into everyday clinical screening procedures worldwide (Young (2006)).

Never the less, it cannot be overlooked that Flat-Panel direct detection systems are of growing interest as they are able to provide an increased spatial resolution and higher detection efficiency in comparison to indirect detection methods (Samei and Flynn (2003)), Gomi et al (2006)). The first system to implement such technology and receive FDA approval was the LoRad Selenia manufactured by

Table 1.1 Comparison of the differing specifications possessed by eleven commercially available DM systems.

System	Manufacture	Detector type	Detection Mechanism	Pixel Size (µm)	Array Size (pixels)	AEC
Senographe 2000D	GE Medical	Amorphous Silicon	Indirect	100	1900 × 2300	YES[§]
Senographe DS	GE Medical	Amorphous Silicon	Indirect	100	1900 × 2300	YES[§]
Senographe Essential	GE Medical	Amorphous Silicon	Indirect	100	2400 × 3070	YES[§]
SenoScan	Fisher Imaging	Scanning CCD	Indirect	54	4095 × 5625	YES
LoRad Selenia	Hologic Inc.	Amorphous Selenium	Direct	70	3328 × 4096	YES
Novation DR	Siemens AG	Amorphous Selenium	Direct	70	3428 × 4142	YES
Novation s	Siemens AG	Amorphous Selenium	Direct	-	-	YES

MammoDiagnost FD Eleva	Philips Medical / Fisher Imaging	Amorphous Selenium/ Photon counting	Direct	50	4096 × 5625	YES
MicroDose	Sectra	Crystalline Silicon wafers	Direct	50	4800 × 5200	NO
Giotto Image MD/SD-SDL	Internazionale Medico Scientifica	Amorphous Selenium	Direct	85	2048 × 2816	YES
Sophie Nuance	Planmed	Amorphous Selenium	Direct	85	2016 × 2816/ 2816 ×3584	YES

§ Has optimal exposure setting which determines kV and mAs based on breast thickness.
- Not specified

Hologic inc. with companies such as Siemens and Planmed following with the Novation S, DR (Williams et al (2008) and Siemens Healthcare) and Nuance (Planmed) respectively.

Several research groups have investigated the use of a-Se based direct digital detectors and results show their implementation in mammography to be beneficial (Zhao et al (1997), Stone (2002) and Belev and Kasap (2004)).

1.2.2 Automated Exposure Control (AEC)

Ever since the commercial success of artificial intelligence (AI) during the early 1980's, the concept has been implemented across a vast amount of industries. Its use ranges from the management of investments in stocks and properties in the banking sector to its implementation within the military for tracking of soldiers (Ferandez (2000)). The use of AI, in the form of automated exposure control (AEC), has also been implemented within the medical imaging sector, namely in mammography, in an attempt to enhance the detection of abnormalities within the female breast.

Prior to the implementation of AEC into mammography, the radiographer would determine the imaging parameters (kVp, mAs, exposure time) manually based on the nature of the breast in an attempt to optimise the x-ray beam quality used. This optimisation would seek to produce films with the correct optical density (OD) by optimising the exposure time and tube current with regards to the limited dynamic range (Meeson et al (1999) and Åslund et al (2005)) SFM provids. It was later demonstrated that x-ray beam optimisation could be achieved not only by the selection of an adequate tube voltage, tube current and

exposure time, but also via the selection of a more appropriate anode/filter material combination (Fahrig and Yaffe (1994) and Dance et al (2000)). Today, AEC acts to ensure adequate image quality is maintained via the use of an optimised x-ray beam.

AEC refers to the automatic selection of the optimum imaging parameters to be used during the image acquisition procedure (Elbakri (2005)). Current techniques consider global exposure control only, taking no account of tissue pathology. Conventionally, this was done by placing radiation sensors, such as ionisation chambers or semiconductor diodes, underneath the film cassette and the exposure was then monitored. The AEC circuitry implemented acted to terminate the exposure once a set threshold was reached, therefore limiting the exposure time (Elbakri (2005)). As the implementation of digital mammography increases, acting to slowly replace the traditional screen-film procedure, the way in which AEC is implemented within a digital detection system is differing slightly as reported by Åslund et al (2005); where the actual digital detector is used both as the AEC sensor and the imaging device.

AEC can be implemented in one of two ways: in a fully automated manner in which all the exposure parameters (kVp, anode/filter material, mAs etc) are selected without user intervention (Young (1996)) or in a semi-automated fashion where the system requires the user's input in selecting specified parameters (Young (1997)). It appears that, regardless of the extent to which the AEC is implemented, both methods work in a similar fashion as they both require a low dose pre-exposure image to be acquired to determine the optimal imaging conditions. The literature also indicates that assumptions are made regarding the relationship of patient dose, image contrast and noise in the selection of the

beam quality and that optimal beam quality is defined as achieving a target contrast to noise ratio (CNR) for the lowest mean glandular dose (MGD) possible.

AEC has proven to be an important and beneficial tool used in mammography, as it enables optimum images to be consistently acquired suggesting that the problems of over-exposure and under-exposure can be avoided. Young et al (2006) demonstrated that images acquired using some form of AEC resulted in a slightly higher dose (MGD) to the breast however the images were found to be significantly better in terms of image quality having a higher CNR. Consequently, a trade off is required, a slightly increased patient dose for a significant contrast improvement.

1.2.3 Automated detection: Computer Aided-Detection

Computer aided detection (CAD) is a post acquisition technique used to detect breast abnormalities by implementing the use of artificial intelligences (Astley and Gilbert (2004)). Its purpose is to act solely as an aid to the radiologist as an indicator identifying potential lesions in the mammogram such as masses and clustered microcalcifications, highlighting them therefore drawing the attention of the radiologist to potential carcinomas (Ko et al (2006)). This is achieved by using a statistical approach where probabilistic calculations are performed assessing the likelihood that a structure contains malignancy-induced abnormalities (Malich et al (2006)); authors have reported computational algorithms used (Wei et al (2005) and Ge et al (2007)).

A vast amount of research has been done in an attempt to develop, evaluate and compare both commercially available and prototype CAD systems. The majority of this work has been undertaken retrospectively using digitised mammograms

produced conventionally by SFM systems (Freer (2001) and Lauria et al (2005)). This comes as a result of (1) there being a large volume of data readily available as this technique has been in use for several decades and (2) FFDM is still a relatively new modality hence only a limited amount of data is available. The studies that have been done on the implementation of CAD in FFDM report mainly on the comparison between the two techniques. For instance, Baum and Fischer et al (Baum et al (2002)) report seeing a 3.7% increase in sensitivity and a decrease in the number of false positives per image in the FFDM technique as well as several other beneficial advantages. Other authors report similar findings (Marx et al (2003) and Nishikawa (2007)).

The studies undertaken thus far on the effect of CAD in mammography have used a range of different materials and techniques as there are no certified standard evaluation protocols in place. Different CAD systems, software versions, radiologists and protocols have been used, therefore making it difficult to accurately determine its overall effectiveness in a systematic comparison. Much of the literature indicates that the level of experience possessed by the reviewing radiologist was significant in determining the effectiveness of the CAD system implemented (Gur et al (2004), Malich et al (2006) and Rangayyan et al (2006)), with the level of experience directly related to the number of cancers missed by the radiologist, which were subsequently identified by the automated system, these being abnormalities that an experienced reader may have spotted.

This indicates that some breast cancers go undetected simply due to them being overlooked when viewed by a single radiologist, with perceptual errors, lack of experience or masking by larger tissue structures all coming into play. As a result, double reading is frequently implemented in an attempt to reduce the number of cancers that initially go undetected. Studies show an increase of up to 15% in

the number of screening-detected breast cancers achieved when this technique is implemented (Morton et al (2006)). As the option of having a second, or even third, reader is an expensive one and most small hospitals/medical centres cannot afford to implement this option, a CAD system would be an ideal alternative. As a reduction in processing time is also seen with FFDM CAD systems in comparison to SFM due to the eradication of the digitisation step, it seems it could also potentially be an attractive alternative for larger busier practices and hospitals.

There have been published reports, such as that produced by Gur et al (2004), where researchers have concluded that the implementation of CAD in mammography has an insignificant effect on the abnormality detection rate. Gur et al (2004) reports seeing only a 1.9% increased abnormality detection rate in comparison to when the CAD system was not implemented. This small increase could be due to a variety of reasons such as the radiologists' level of experience (quite high in this case), the nature of the mammograms chosen to make up the study (how they were chosen), the way in which the reported evaluation parameters were determined (Nishikawa, 2007) or simply because a refining of the computational algorithms used may be required.

When summarising the literature, a general trend can be seen throughout where the implementation of CAD in digital mammography (DM) results in a 1.9% - 15.0% increase in cancer detection rates. This suggests that a significant number of successful biopsies may have been performed if CAD was used where malignancies had initially gone undetected. The performance of CAD systems is increasing as dedicated teams of researchers continue to develop, test and evaluate systems resulting in a continuous evolution of software. Due to these

on-going technological advancements, it is inevitable that CAD will become a standard aid for mammography in the future.

1.3 Energy dispersive x-ray diffraction

Histopathology is the gold standard for tissue classification. Surgical specimens or biopsy aspirations are microscopically examined by a pathologist leading to a diagnosis. Although a well accepted technique, it requires surgical removal of tissue therefore is an invasive procedure. A non invasive means of tissue classification has been developed and is currently under investigation by research groups across the globe (Bohndiek et al (2008) and Castro et al (2005)). The technique makes use of the scattered photons present during x-ray imaging.

1.3.1 Rayleigh Scatter Imaging

Scatter has traditionally been seen as a problem within medical x-ray imaging as it acts to degrade image quality therefore hindering abnormality detection. A significant amount of research has been undertaken over the past two decades attempting to characterise and make use of this ever present 'unwanted' radiation (Johns and Yaffe (1982) and Kosanetzky et al (1987)). It has been shown that information regarding a material's atomic and molecular structure is obtainable when scattered radiation is acquired (Hukins (1983)). This information due to the atomic structure of the material arises in the form of a diffraction profile (fig 1.1). Different molecular arrangements produce different diffraction patterns. Thus, by measuring the diffracted signal at small angles as well as the transmitted signal, valuable information can be obtained. This material specific

signature has proven to play a pivotal role within medical physics enabling ADXRD and EDXRD to become topics of research giving rise to novel applications.

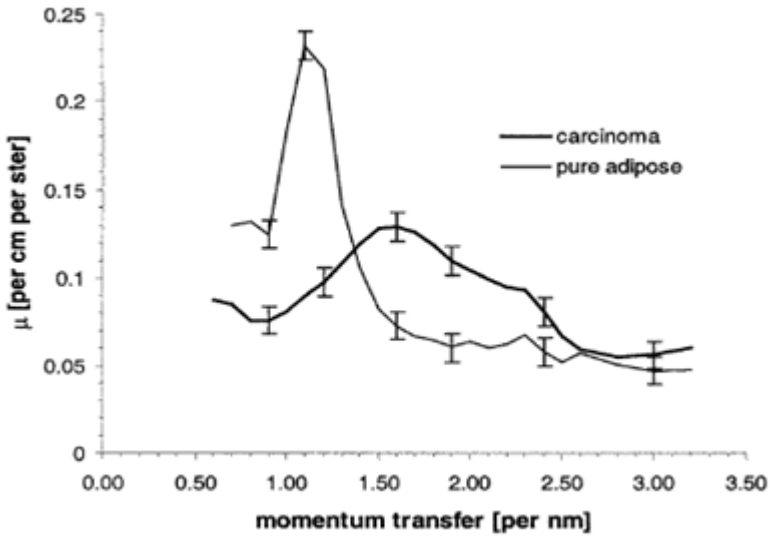

Figure 1.1 Illustration of the characteristic peaks of pure adipose tissue and cancerous tissue (Kidane et al (1999)).

At diagnostic energies (<100keV), coherent scatter dominates among the low scattering angles (approximately $<10°$) exposing the molecular structure of a material. This information has enabled research groups worldwide to extract, characterise, and therefore diagnose pathological tissue conditions (Kosanetzky et al (1987), Poletti et al (2001), Changizi et al (2005) and Theodorakou et al (2008)). Many tissue types have been investigated ranging from brain, kidney, muscle, uterus, colon, prostate and liver (Theodorakou et al (2008)) however the two main areas that have received significant attention are those pertaining to the breast and bone.

1.3.2 Coherent Scatter

Coherent scatter is an elastic scatter process that arises when the electric field of an electromagnetic wave interacts with the electrons within an atom in close proximity causing it to vibrate, resulting in radiation emission. As no energy is transferred to the atom, the photon is scattered with an energy equivalent to that of the incident photon; the differential cross section for coherent scatter is expressed as shown in equation 1.1 below:

$$\frac{d\sigma_{coh}}{d\Omega} = \left(\frac{d\sigma_{coh}(\theta)}{d\Omega}\right)F^2(x, Z) \quad m^2sr^{-1} \text{ per atom} \qquad \text{(Eq. 1.1)}$$

Where $\left(\frac{d\sigma_{coh}(\theta)}{d\Omega}\right)$ is the Thomson cross section, $F^2(x, Z)$ is the elastic scatter form factor accounting for interference between x-rays scattered from various electrons within the atom and is related to the Fourier transform of the atomic charge density which has been tabulated in Hubbell et al (1975). Z is the atomic number and *x* is the momentum transfer.

The Thomson cross section gives rise to the angular distribution of the scattered x-ray photons (Eq 1.2):

$$\frac{d\sigma_{coh}(\theta)}{d\Omega} = \frac{r_0^2}{2}(1 + \cos^2\theta) \quad m^2sr^{-1} \text{ per } e^- \qquad \text{(Eq. 1.2)}$$

Where $\frac{d\sigma_{coh}(\theta)}{d\Omega}$ represents the probability of an x-ray photon being coherently scattered, $r_0 = 2.818 \times 10^{-15}m$ is the classical electron radius and $(1 + \cos^2\theta)$ is the averaged polarisation where θ represents the photon scattering angle.

Constructive interference between x-ray photons occurs when Bragg's law is satisfied, the latter stating that the difference in path length between two

scattering planes must be an integer value *n* of wavelengths λ, is satisfied (Eq 1.3):

$$n\lambda = 2dsin(\theta) \quad \text{(Eq. 1.3)}$$

Where λ is the photon wavelength, *d* is the spacing between scattering planes in a crystal and θ is the photon scatter angle.

This constructive interference results in the manifestation of a material specific intensity profile formally known as an x-ray diffraction profile, and is a function of momentum transfer (Eq 1.4).

$$\mathrm{x} = \frac{E}{hc} sin\frac{\theta}{2} \quad \text{(Eq. 1.4)}$$

Where E is the incoming photon energy, *h* is Planck's constant*, c* is the speed of light and θ is the photon scatter angle.

These material specific characteristic peaks are therefore dependent on *d*. Crystalline materials are characterised by their narrow, sharp peaks yielded by their long range order. The opposite is true for amorphous materials where a broad peak is observed as a consequence of their short range order. As these peaks are material specific, it is possible to identify the spacing's between the scatter sites, which leads to inference of the constituting materials.

1.3.3 Previous medical EDXRD Work

1.3.3.1 Breast tissue

Speller and Horrocks (1990) shed light on the fact that x-ray diffraction patterns were first observed in 1912 and have since been utilised within the field of material sciences to evaluate the structures of biochemical molecules. Since then, Speller (1999), Royle et al (1999), Kidane et al (1999), Poletti et al (2002) and Bohndiek et al (2008) are just a few of the authors to demonstrate the potential uses and applications specific to medicine of coherent scatter.

Konsanetzky et al (1987) extracted the differential scatter cross sections from the measured x-ray diffraction patterns of a range of biological and tissue-equivalent materials. It was shown that water and Lucite exhibited typical amorphous material scatter patterns. Royle et al (1999) not only showed that EDXRD could be used to characterise crystalline tissues, such as bone, but also that classification between healthy and diseased amorphous tissue could also be achieved. Both Poletti et al (2002) and Kidane et al (1999) concluded that the shape and height of diffraction peaks were two important properties that could be used to enhance cancer detection with respect to clinical mammography. The authors obtained the diffraction patterns (linear differential scattering coefficient versus momentum transfer) from seven (four adipose and three glandular) and one hundred breast tissue samples (sixty one normal and thirty nine neoplastic) respectively, where it was seen that the characteristic peaks for adipose and carcinoma tissue occur at approximately $1.6nm^{-1}$ and $1.1nm^{-1}$ respectively (fig 1.1). The latter study demonstrated that the characteristic peak for carcinoma tissue is similar to that of glandular tissue at approximately $1.6nm^{-1}$ (fig 1.2). Castro et al (2004) and Changizi et al (2005) experimentally confirmed these

findings, however they did so on a limited number of samples compared to Kidane et al (1999).

Bohndiek et al (2008) demonstrated that diffraction imaging was possible using a CMOS active pixel sensor based system and suggested that 'on-the-fly' diffraction pattern recognition was possible. Scatter patterns from eleven different materials were obtained spanning three medical applications including breast cancer diagnosis. It was concluded that CMOS APS detectors were suitable for diffraction imaging. The findings by those mentioned above, as well as others (Griffiths et al (2007), Ryan and Farquharson (2007) and Theodorakou and Farquharson (2008)) prompts further application specific investigations with respect to the use of coherently scattered x-ray photons in medicine.

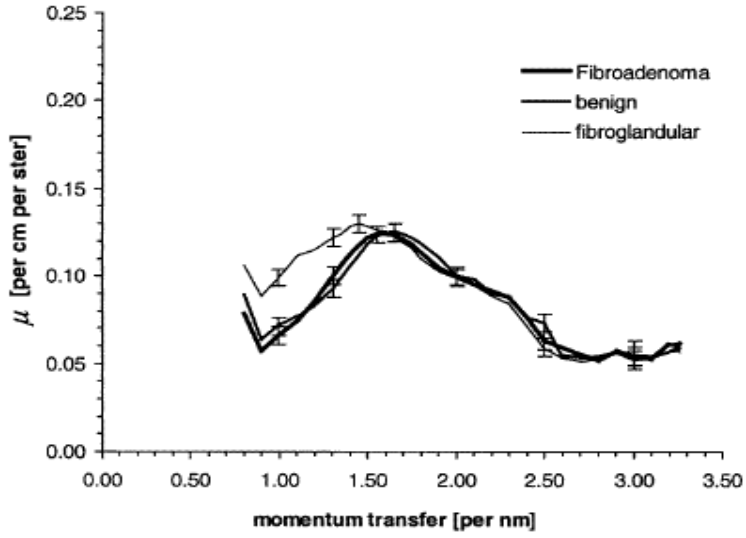

Figure 1.2 Comparison of three similar diffraction peaks pertaining to three different tissue types found within the breast (Kidane et al (1999)).

1.3.3.4 Bone

The composition of bone is collagen and hydroxylapatite in the form of mineral salts (Batchelar et al (2006)). Bone disease, namely osteoporosis, is a metabolic disorder affecting bone strength and homeostatic regularitory ability arising from an imbalance of bone formation and reabsorption (Bono and Einhorn (2003)). Bone mineral density (BMD) serves as an important indicator in determining the condition of the bone, i.e. healthy or diseased where a reduction in mineral mass due to adipose replacement is observed in trabecular bone (Justesen et al (2001)). Authors have demonstrated the benefits of using coherent scatter in determining the mineral content of bone (Royle et al (1991), Newton et al (1992) and Barroso et al (2007)) therefore indicating the presence of osteoporosis.

Royle et al (1991) not only demonstrated that the changes in bone substitute concentration was more apparent using EDXRD as opposed to ADXRD, implying an increased sensitivity to bone mineral changes in the former technique, but also showed that the bone mineral content from both archaeological diseased tissue and fresh excised femoral heads could be scientifically estimated (Royle et al (1999)). Farquharson and Speller (1997) demonstrated that it was possible to quantitatively detect and perform analysis on archaeological human bone samples using EDXRD. They showed that Low angle X-ray scatter (LAXS) performed better at correlating BMD to pre-obtained values than other imaging methods investigated. More recent investigations demonstrated that it is possible to quantitatively obtain the collagen-mineral ratio from intact bone phantoms utilising coherent-scatter computed tomography (CSCT) (Batchelar et al (2006)) enabling the monitoring of changes in the bone indicative of bone disease.

1.4 X-ray detection systems

Although EDXRD and ADXRD ultimately give rise to the same information, the requirements, therefore the experimental setup, for obtaining scatter profiles differ for each technique. EDXRD is reliant on the detection of x-ray scatter from the sample using a high resolution energy-resolving detector, namely, a high purity Germanium (HPGe) positioned at a fixed angle. The spectrum incident on the sample is collimated to a parallel pencil beam which is stepped across the tissue sample. A collimator is placed at the entrance to the detector consequently limiting the scatter angle. The scatter profile is obtained as a function of energy.

Unlike EDXRD, traditional ADXRD is carried out using a monoenergetic pencil beam such as that of a synchrotron. However, as such facilities are inaccessible for routine analysis, it has been demonstrated, as seen with diffractometry, that a standard laboratory x-ray tube consisting of a copper anode with nickel filtration can be used giving rise to a quasi-monoenergetic x-ray beam. Scatter profiles are then measured as a function of angle. As the x-ray beam is of inherently low energy (8 keV) resulting from the K_α lines of copper, penetration depth is severely limited therefore restricting samples to be of a small powdered nature.

Planar x-ray imaging differs significantly from EDXRD or ADXRD. Whereas the detection of x-rays scattered from a sample are of interest for the latter techniques, ideally, planar imaging makes use of transmitted x-rays only, therefore rendering contrast reliant on the intensity of the x-rays traversing the sample without interaction. For the purpose of mammography, either a

molybdenum, rhodium or tungsten target with adequate filtration is used depending on the nature of the breast to be imaged.

1.4.1 CMOS APS

Over the last two decades, Complementary Metal Oxide Semiconductor Active Pixel Sensors (CMOS APS) have received a lot of attention as research groups have focused on enhancing this technology. Since the invention of the CMOS sensor in 1967 (Weckler (1967)), before that of the Charge Coupled Device (CCD) (Smith and Boyle (1970)), the architectural design of the CMOS sensor has been developed, enhancing its capabilities. As a result of the movement from passive to active, CMOS APS devices have found their way into a broad spectrum of modern day applications ranging from mobile phone cameras and baby monitors (Fossum (1997)) to aero-space ((Bai et al (2003) and Buonocore et al (2005)), automotive and medical applications. Both Schanz et al (2000) and Hosticka et al (2003) demonstrated that CMOS APS sensors meet the requirements inherently imposed within the automotive imaging industry, which requires imaging sensors to have a wide dynamic range and to be able to function at temperatures in excess of 85°C. Both authors measured dynamic ranges of 120dB by using skip logic and logarithmic type read outs. Sandini et al (2000) and Schwartz et al (1999) both demonstrated that the advantages accompanied by CMOS sensors could also be used within the biomedical sector, with both research groups demonstrating that CMOS sensors can be used as the key components in retina-like implant systems fulfilling special requirements including sub-region addressing, low power consumption and a high dynamic range.

The simplest CMOS APS structure comprises of four components per pixel; a photodiode, and three transistors (3T), as illustrated in figure 1.3 (Gamal and Eltoukhy (2005) and Hoffman et al (2006)). The photodiode is responsible for charge generation and charge collection, where the former is related to the sensor's ability to detect in-coming photons and generate a representative signal, whilst charge collection governs the sensors ability to reproduce an image (Janesick et al (2003)). Ideally, 100% of the optical photons incident on the sensor would be detected and then converted to a corresponding voltage; however, due to the inherent nature of the sensor, this is not possible. This quantum efficiency (QE) loss is predominantly due to three mechanisms; absorption, reflection and transmission losses. Absorption losses are a result of the optically opaque structures located within and above the pixel such as the transistors and metal bus lines used to inter-connect the transistors, structures which act to reduce the fill factor of the detector consequently the image quality (Bigas (2006)). Reflection losses are contributed to by the insulating layers directly above the epitaxial layer where losses due to transmission occur when a photon passes through the thin epitaxial layer without interacting therefore goes undetected (Janesick and Putnam (2003)). Methods of increasing the fill factor have been investigated and near 100% fill factors have been reported (Dierickx et al (1997)).

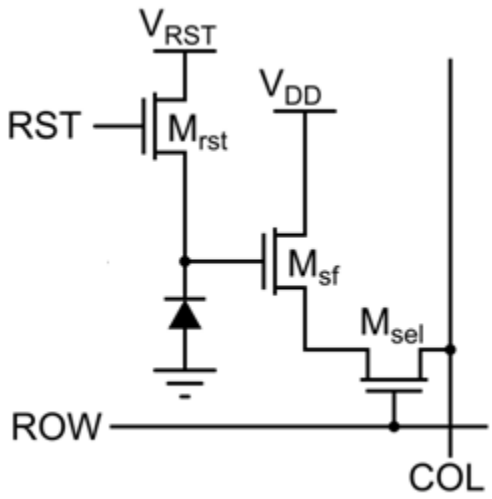

Figure 1.3 Schematic of basic three transistor (3T) CMOS APS pixel circuitry.

The three transistors, reset (M_{rst}), source follower (M_{sf}) and row select (M_{sel}) implemented within a 3T APS are illustrated above (fig 1.3). The M_{rst} transistor enables the V_{RST} voltage to pass through to the photodiode consequently recharging its capacitance to a reference level. It is then opened enabling integration of the photocurrent incident on the sensitive node. As the photodiode is reversed biased, the capacitor discharge is proportional to the integration time therefore a bright pixel gives rise to low voltage and vice versa (Yadid-Pecht and Etienne-Cummings (2004)). The M_{sf} transistor acts to isolate the sense node from the column bus capacitance whilst buffering the voltage from the node which is then read out via the row select transistor to the column bus (Gamal and Eltoukhy (2005)).

Although CMOS APS devices excel in performance when it comes to power consumption, production costs, reliability, anti-blooming, windowing, radiation tolerance and read out speed, CCD technology still dominates the market with regards to medical imaging devices. This is mainly due to the fact that CMOS active pixel sensors suffer from an increased noise level in comparison to that of

CCDs. This is due to the numerous transistors located within each pixel. This architectural structure also acts to inhibit the fill factor of the devices in comparison to the 100% fill factor commonly achievable by the CCD (Bigas et al (2006)).

1.5 The Intelligent Imaging Sensor project

The Intelligent Imaging Sensor project (I-ImaS project) was a three year, EU funded project consisting of a European consortium spread across five EU countries. The aim of the project was to develop a new generation of active pixel sensors that would revolutionise the data acquisition phase, and therefore enhance the diagnostic quality, of medical x-ray images.

The project was split into three phases, the design, manufacture and evaluation of a prototype system which had the potential to optimise imaging parameters in real time during a scan via the implementation of an intelligent feedback mechanism. At the close of the project, only a limited system evaluation had been performed. A preliminary investigation into possible implementable feature functions had been undertaken (and is discussed further in chapter three) which gave rise to potentially useful implementable statistical functions (I-ImaS (2005)). The feature extraction performances of a selection of the suggested functions have been investigated further along with several new feature functions consequently forming the basis of this thesis. Also, this thesis looks at a novel method of feature extraction using EDXRD imaging, where the highly specific nature of the diffraction signature is used to optimise data acquisition.

1.6 The aim and scope of this thesis

This thesis firstly explores the concept of real-time image optimisation based on grey level pixel values using a feedback mechanism made available via the use of CMOS APS sensing devices. A prototype digital mammography system, the I-ImaS system, is characterised then used to explore real-time image optimisation. A low exposure 'scout' image is acquired, statistically interrogated and used as a control function which is fed back through the feedback system 'on-the-fly' enabling real time optimisation of the exposure incident on the sample which is being acquired simultaneously. As a result, an 'intelligent' image made up of various incident exposures is produced consequently acting to reduce the incident exposure to healthy, unsuspicious tissue regions within the breast whilst increasing it to suspicious, potentially cancerous regions. In doing so, it is thought that the contrast between normal and suspicious tissue regions will increase, therefore enhancing the diagnostic quality of the image.

Secondly, the thesis explores the use of energy EDXRD to guide the enhancement process. EDXRD is a proven technique able to clearly differentiate between breast tissue types i.e. healthy and cancerous (Kidane et al (1999)). The use of EDXRD signals as a means of parameter guidance guiding the exposure optimisation procedure is also explored. EDXRD images of breast samples are acquired, analysed and then the analysis results are fed back into the imaging system, consequently governing exposure modulation.

Chapter Two

Experimental systems and their performance evaluation

2.1 Overview

As described in chapter one, the migration of mammographic imaging from SFM to FFDM has enabled mammography to take on a new form where by the introduction of various imaging enhancement techniques is now possible. This has consequently revolutionised the way in which mammography is performed. This chapter describes the imaging systems and, where appropriate, the configurations used to undertake the experimental investigations described in chapters three and four of this thesis.

The implementation of intelligent imaging within digital mammography is a concept waiting to be explored. The ability of an imaging system to identify suspicious tissue regions enabling imaging parameter optimisation in real time during the data acquisition phase of mammography to local tissue regions would prove to be highly desirable, this would minimise the dose to healthy tissue. Such a system would not only require the ability to collect data, as is conventionally done, but also to analyse it, that is, to differentiate between healthy and diseased tissue types, and then optimise the collection of the data, all in real-time during data acquisition.

Two experimental systems are used within this investigation. The two systems differ as one was designed for transmission imaging only (the I-ImaS system), and the other was designed for x-ray scatter detection only (EDXRD system). Both are discussed below where x-ray characterisation of the I-ImaS sensor is reported.

2.2 The Intelligent Imaging System (I-ImaS)

The prototype I-ImaS system is a medical imaging unit that has been specifically designed and developed for intelligent mammographic imaging. It is a scanning system comprising of five major components which work together enabling the production of intelligent x-ray images. The use of a staggered dual array of CMOS monolithic active pixel sensors (MAPS) enables image optimisation, where the first sensor array, the 'scout' array, is used to acquire a low exposure, scout image of the sample whilst the trailing sensor array, the 'ImaS' array, is used simultaneously to acquire an optimised exposure image of the corresponding sample region that had previously been imaged with the first sensor array as shown in figure 2.1 below.

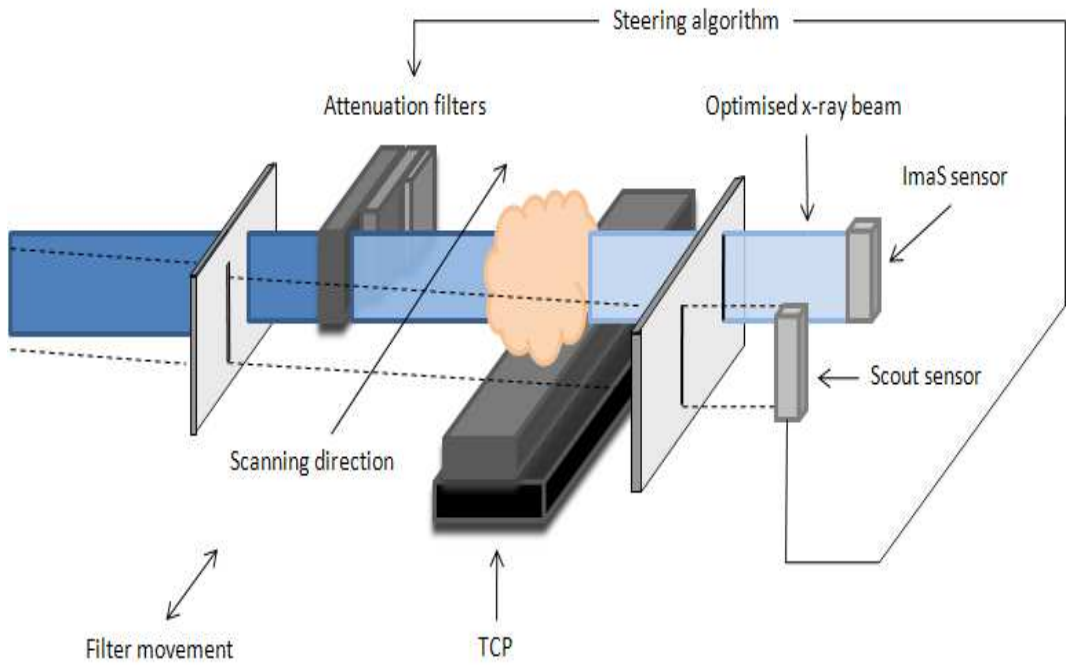

Figure 2.1 Schematic illustrating functionality of the prototype I-ImaS imaging system.

The scout image is statistically interrogated using feature functions resulting in the extraction of information from the image. This information is then fed back through the system, aiding optimisation of the incident exposure on the portion of the breast being imaged by the ImaS array. X-ray beam modulation is achieved using a set of attenuation filters designed to alter the beam intensity. These filters are aligned with the individual Imas array sensor and stepped in and out of the x-ray path accordingly as determined by the feedback (steering algorithm) mechanism (fig 2.1). The final optimised image, the 'I-ImaS' image, is the sum of both the scout and the Imas image.

2.2.1 I-ImaS system components

The I-ImaS system is an assembly of sophisticated electronic and mechanical components (fig 2.2). They co-operate enabling the constant relaying of information throughout the system ensuring the critical functioning of each component during the data acquisition, data analysis and optimisation phase of the imaging process. A description of the functionality of each individual component is given below.

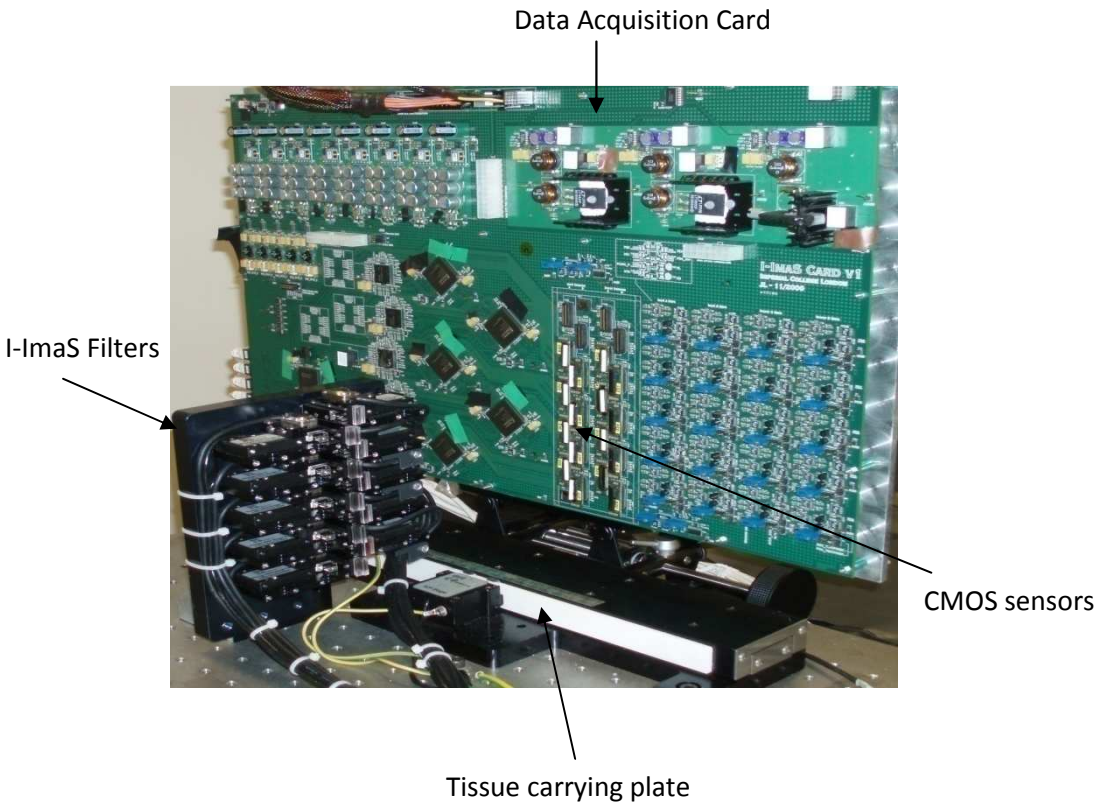

Figure 2.2 The data acquisition components used by the I-ImaS system.

2.2.1.1 The I-ImaS sensors

The I-ImaS sensors were specifically designed, developed and optically characterised by Rutherford Appleton Laboratory (Turchetta et al (2007)). The intelligent imaging system can use up to twenty integrating 3T CMOS APS devices for x-ray detection where x-ray sensitivity is increased using a thallium doped caesium iodide (CsI:TI) scintillator. Sensor characteristics are given in table 2.1.

Table 2.1 Physical characteristics of an individual I-ImaS sensor where x-ray sensitivity is increased using a scintillator.

Specification	I-ImaS Sensor
Detector Type	CMOS MAPS
Detection Mechanism	Indirect
Pixel Size (μm)	32×32[a]
Readable Array Size (Pixels)	520×40[a]
Dynamic Range	72dB[a]
Reset Type	Flushed[b]
Read out	Rolling shutter[b]
Array Dimensions (mm)	16.64×1.26[b]
Epitaxial layer (μm)	14[b]
Full Well Capacity (e^-)	$\approx 10^5$
Scintillator Type	Structured CsI:TI
Scintillator Thickness (μm)	100
Fibre optic plate thickness (mm)	1
Scint. Light Yield (Pho/MeV)	≈ 66 000[c]
Scint. Density (g/cm^3)	4.51[c]
Maximum Emission wavelength (nm)	≈ 550 [c]

[a]Fant et al (2007)
[b]Turchetta et al (2007)
[c]Nikl (2006)

2.2.1.2 The data acquisition card

The data acquisition (DAQ) card plays a crucial role within the imaging system. It is responsible for analysing the acquired scout images and running the intelligent image processing algorithms, consequently governing the imaging parameter modulation process. It also houses and runs the dual array of twenty CMOS APS sensors that are used to acquire the images and the system's field programmable logic arrays (FPGA's), whilst acting as a power source to the sensors and providing a means of direct communication to the motion control system (MCS) and imaging system control station (a PC). A communication protocol is used between the DAQ and the MCS enabling firstly, the defining of the system configuration commands used to set the experimental parameters, followed by

active experiment commands which set the positioning of the tissue carrying plate (TCP) and the x-ray beam attenuation filters.

2.2.1.3 The tissue carrying plate stage (TCP)

The current system utilises a stationary x-ray beam and scans the sample across the beam on the TCP depicted in figure 2.3. However, a clinical system would hold the breast stationary and scan the x-ray beam, attenuation filters and CMOS sensors. The custom built TCP (ANCO) has a maximum travel distance of 160mm across the sensors and can be positioned with an accuracy of ±3µm. It communicates its true position back to the MCS via an encoder (MicroE M1550-40). The encoder keeps track of the TCP position using an encoder tape mechanism which is inscribed with lines 0.5µm apart.

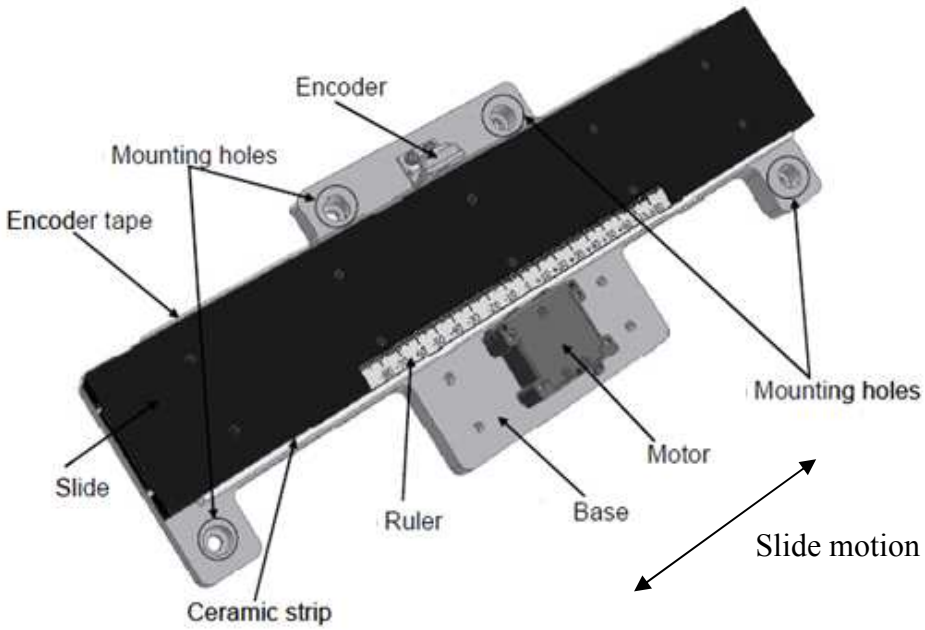

Figure 2.3 Tissue carrying plate used to scan breast samples across sensor arrays (I-ImaS D27 (2006)).

2.2.1.4 The x-ray beam attenuation filters

The x-ray beam attenuation filters modulate the exposure incident on the breast in real time during the data acquisition phase. The filters have a step wedge structure constructed from varying thicknesses of poly-methylmethacrylate (PMMA) and aluminium (Al) layers which act to provide nominal x-ray absorption ratios ranging from 20% to 100% for a 30kV tungsten (W) anode x-ray source (fig 2.4 and table 2.2). Each step of the filter corresponds to the size of a single ImaS sensor enabling the exposure modulation of a sensor sized region of interest (ROI) to be achieved. The relevant segment of the filter is stepped in front of the sample in line with the corresponding ImaS sensor when required and is governed by the steering algorithm. The precise movement of the filters is controlled in an identical manner to that of the TCP, utilising an encoder and piezo-ceramic motors. The system comprises ten rows of filters corresponding to the I-ImaS sensor array.

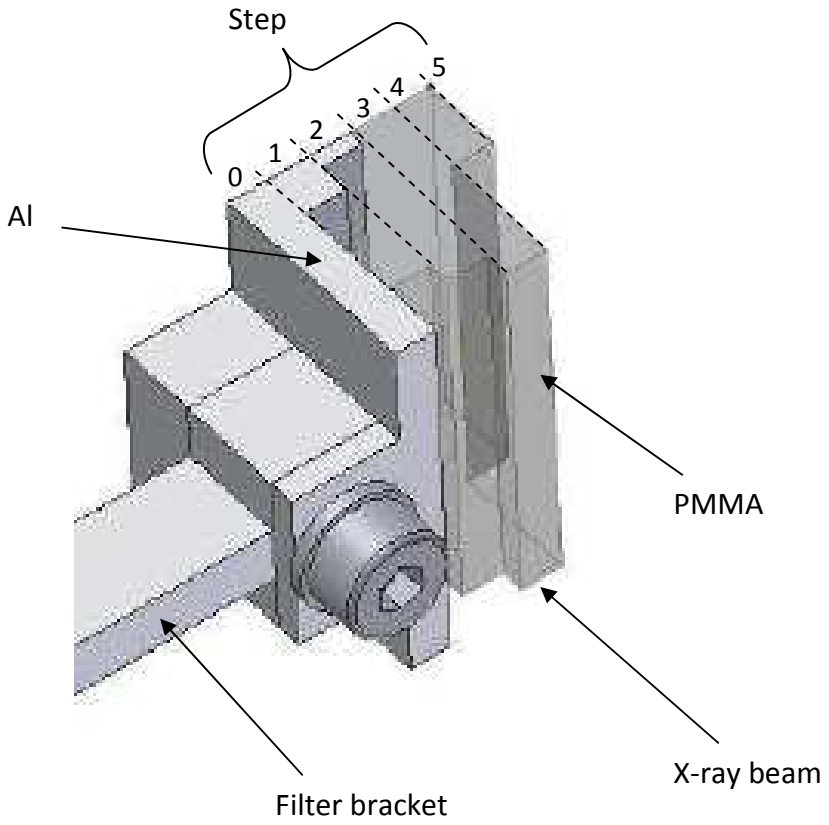

Figure 2.4 I-ImaS x-ray beam attenuation filter used to optimise the exposure incident on the breast sample (I-ImaS D27 (2006)).

Table 2.2 I-ImaS x-ray beam attenuation filter construction for use with a 30kV, W anode source.

Filter Position	Actual Beam attenuation (%)	Filter Structure (mm)
0	100	8 Al
1	85	1.8 Al + 4 PMMA
2	67	0.6 Al + 6 PMMA
3	46	7.5 PMMA
4	23	3 PMMA
5	0	No filtration

2.2.1.5 The motion control system (MCS)

The MCS houses all the necessary electronic components for the implementation of the motion functions for the system. It is responsible for the motion controller's precise movement of both the TCP and the x-ray beam attenuation filters. The twelve motion controllers (Nanomotion LTD AB1A) receive feedback signals pertaining to the actual position of the stage from the encoders device enabling correction of the command in order to ensure the specified translation distance is achieved. It also determines the torque required for precise movements.

2.3 EDXRD system components

As the custom built I-ImaS system was designed and developed for transmission imaging only, a separate experiment was set up in order to investigate the use of EDXRD signals as a means of intelligence for the I-ImaS imaging system. This system was a laboratory based EDXRD system and is described below (fig 2.5).

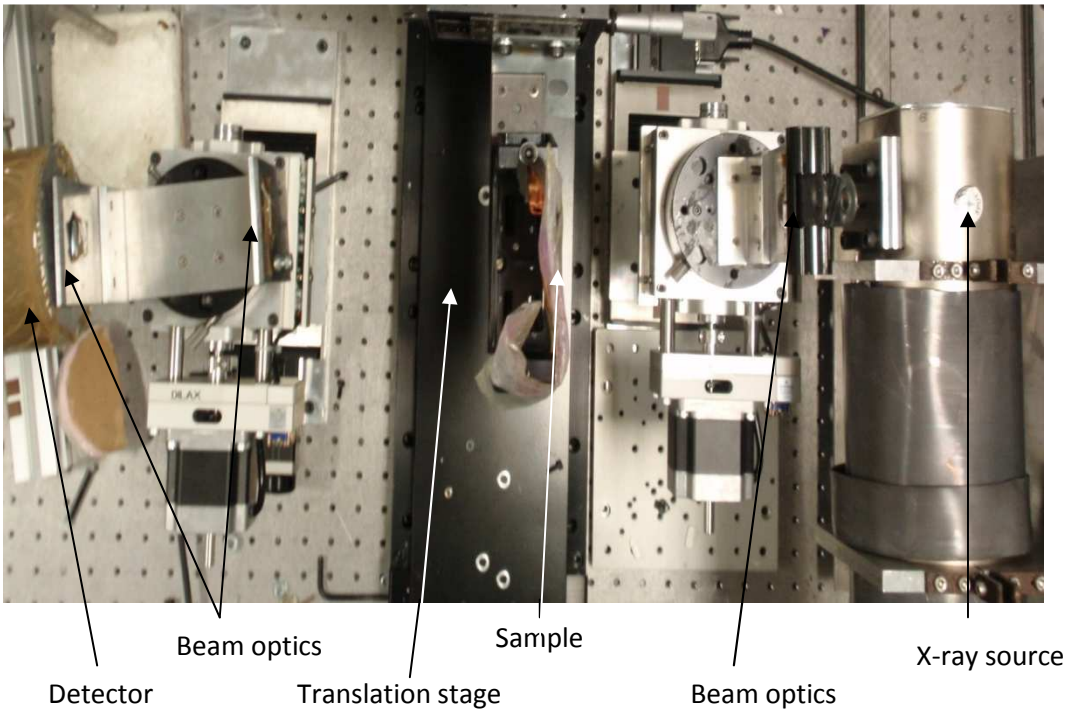

Figure 2.5 Laboratory based EDXRD system setup used to acquire diffraction profiles of tissue samples.

2.3.1 The X-ray unit

The x-ray source used was a 30kW W anode industrial x-ray tube (AGO installations, UK) with a maximum voltage of 160kVp. It was operated in fluoroscopy mode at a maximum potential of 60kVp and 5mA and thus avoiding production of the characteristic k-lines of W whilst ensuring a detector dead time of < 10%.

2.3.2 Photon detection

The x-ray photons scattered by the sample were detected using a high purity electronically cooled germanium (HPGe) detector with a planar crystal of diameter 36mm and depth 10mm (GLP-36360/13P, Ortec, USA). It was

controlled by a DSPEC Jr 2.0 (Ortec) multichannel analyzer (MCA) and used Maestro software (Ortec) for data collection which assigned the detected photons to one of the 512 available channels. The energy resolution of the detector was measured to be 0.59keV at 59.9keV where system calibration was achieved using an Amerciuam-241 source.

2.3.4 EDXRD system optics

The collimators used to define the x-ray beam were interchangeable allowing the effect of spatial resolution on abnormality detection to be investigated. The solid angles of the collimators used were 0.23, 0.43 and 0.98msr. Each collimator was made of 3mm lead with 3mm aluminium backing. A nominal scatter angle of 6^{o} was selected as it has been shown to be optimal for EDXRD breast tissue studies (Kidane et al (1999)).

2.4 EDXRD system configuration

The resolution of the EDXRD system is governed by both the angular resolution of the system and the energy resolution of the detector (eq 2.1) and is measured in terms of momentum transfer. Figure 2.6 depicts the geometry used to obtain the EDXRD signals. The system optics were interchangeable therefore changing the angular resolution hence the resolution of the system along with the incident exposure level.

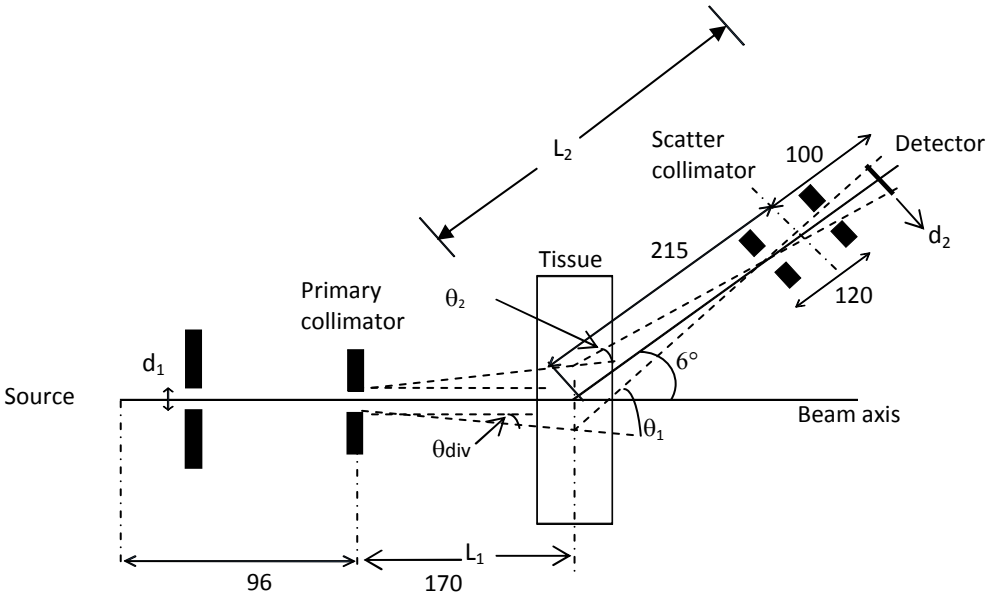

Figure 2.6 Schematic illustrating the geometry of the EDXRD system used in this investigation (units of mm).

$$\frac{\Delta x}{x} = \sqrt{\left(\frac{\Delta\theta}{\theta}\right)^2 + \left(\frac{\Delta E}{E}\right)^2} \qquad \text{(Eq. 2.1)}$$

Where $\frac{\Delta E}{E}$ represents the energy resolution of the detector and $\frac{\Delta\theta}{\theta}$ is the angular resolution of the system (eq 2.2) defined by the collimation width and source-sample-detector distances.

$$\frac{\Delta\theta}{\theta} = \frac{\theta_1 - \theta_2}{\theta} \qquad \text{(Eq. 2.2)}$$

Where according to Cook (2008), θ is the nominal scatter angle and θ_1 and θ_2 are the maximum scatter angles that a photon can undergo and still reach the detector. These are computed using equation 2.3 and 2.4.

$$\theta_1 = tan^{-1}\left[\frac{L_2\tan(\theta) + \frac{d_2}{2}\cos(\theta) + \frac{h}{2}}{L_2 - \frac{d_2}{2}\sin(\theta)}\right] + \theta_{div} \qquad \text{(Eq. 2.3)}$$

$$\theta_2 = tan^{-1}\left[\frac{L_2\tan(\theta)-\frac{d_2}{2}\cos(\theta)-\frac{h}{2}}{L_2+\frac{d_2}{2}\sin(\theta)}\right] - \theta_{div} \qquad \text{(Eq. 2.4)}$$

Where $h=d_1 + 2L_1 tan(\theta_{div})$

Theoretically, the above calculations consider the most extreme outer edge photon acceptance range. However, it has been shown by Luggar et al (1996) that different regions within the scattering volume subtend differing angular ranges at the detector. Consequently, extreme scatter angles are less probable than the angles immediately surrounding the nominal scatter angle.

With the distances indicated in figure 2.6 and a collimation width of 1mm, an angular resolution of 0.3 is obtainable. As the collimation width is increased to 2mm and then 3mm, $\frac{\Delta\theta}{\theta}$ becomes 0.7 and 1.0 respectively. Considering this, it becomes apparent that a compromise must be reached between the angular resolution of the system and the photon flux reaching the detector.

2.5 Summary

The data acquisition systems used to explore the intelligent imaging concept have been described. The custom built I-ImaS system is able to acquire transmission images only; therefore two separate experiments had to be setup in order to have acquired and investigated the use of EDXRD signals as a means of intelligent input. These diffraction signals would govern parameter optimisation as opposed to the statistical information extracted from the low exposure mammogram obtained by the I-ImaS system (fig 2.7). X-ray beam modulation is

achieved using attenuation filters which are stepped in and out of the x-ray beam path consequently optimising incident exposure to the breast as deemed appropriate by the steering algorithm. The EDXRD system makes use of an electronically cooled HPGe detector which has good energy resolving capabilities enabling the detection of scattered photons from a restricted angular range.

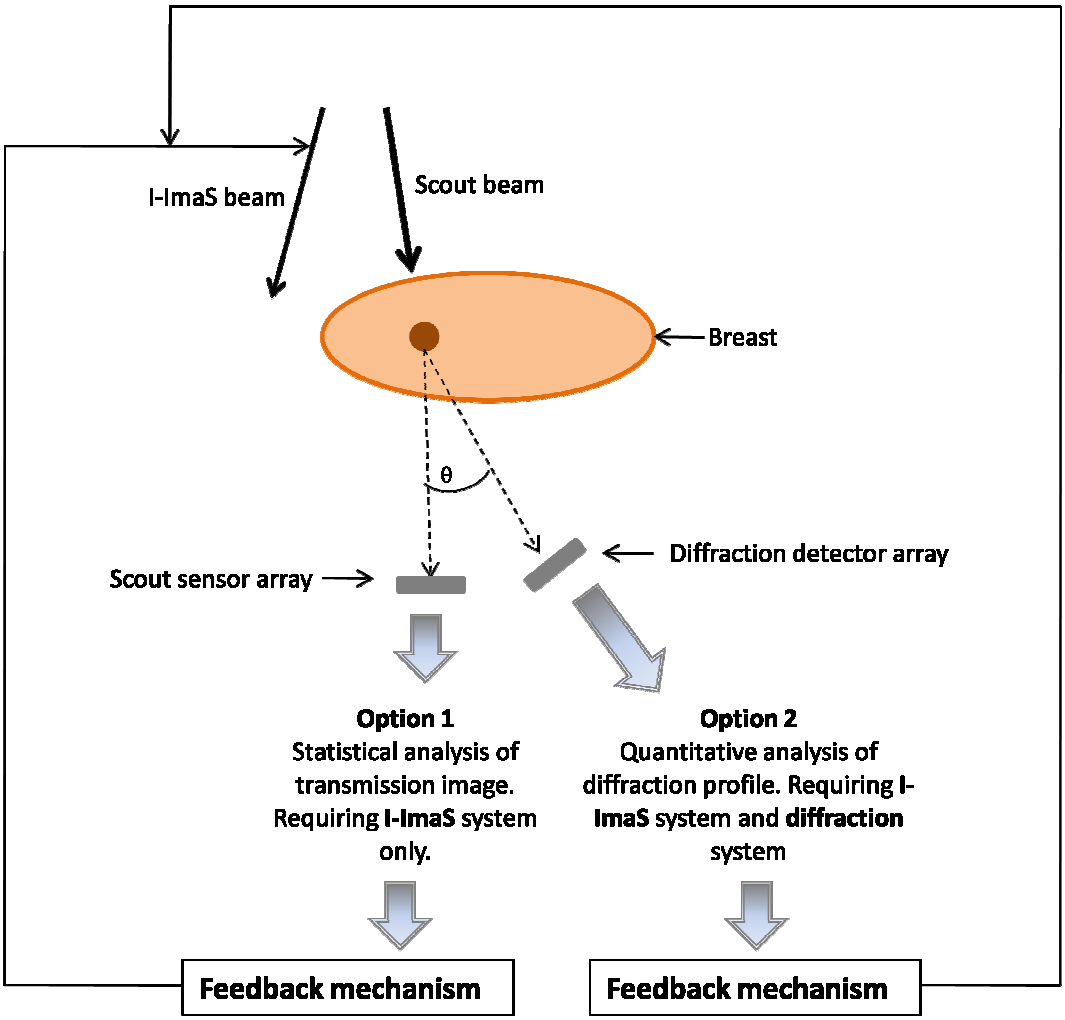

Figure 2.7 Illustration of intelligent concept using low exposure scout image to derive system intelligence (option 1), and EDXRD concept (option 2).

The indirect photon integrating mechanism of the I-ImaS system sensor was seen to greatly differ to that of the direct photon counting detection mechanism used within the EDXRD system. Unlike the CMOS APS devices, the germanium detector did not require an intermediate step of x-ray photon to light conversion therefore eliminating the need for a scintillator. However, both the I-ImaS system and the EDXRD system were both scanning systems requiring breast tissue samples to be either scanned across the face of the detector as was the case in the I-ImaS system, or scanned across the face of a collimator, as was the case in the EDXRD setup.

2.6 Specimen evaluation: Radiologist's analysis

Two breast tissue samples were used (fig 2.8) which were obtained from patients who had undergone mastectomies at least three years prior to this investigation. These samples were collected by Professor A.M Hanby at the academic Unit of pathology, St James' University hospital, Leeds. Both breast specimens referred to as sample one and sample two, were excised formalin fixed specimens individually sealed in polythene packs that had been stored at room temperature. The thickness of each sample was measured to be 10.2mm ± 0.5mm and 14.3mm ± 0.5mm respectively throughout their central region.

As the role of the intelligent feedback mechanism is to differentiate between suspicious and healthy tissue regions, classification of such regions first had to be made. A radiologist (Kazantzi) was used to first examine x-ray images of both samples identifying suspicious regions therefore determining those worth looking at more closely. Figure 2.9 illustrates the regions marked as suspicious. Sample one appeared to vary greatly between glandular and adipose tissue

whilst sample two appeared to be of a predominantly adipose nature. It was concluded that a severe fibrocystic element was present within sample one (as depicted in figure 2.8a) unlike sample two where the abnormality was embedded in a fairly homogeneous layer of adipose tissue. This diagnosis therefore indicated that sample one would act to test the extreme functionality of the statistical feature functions while sample two would determine whether the basic concept was feasible.

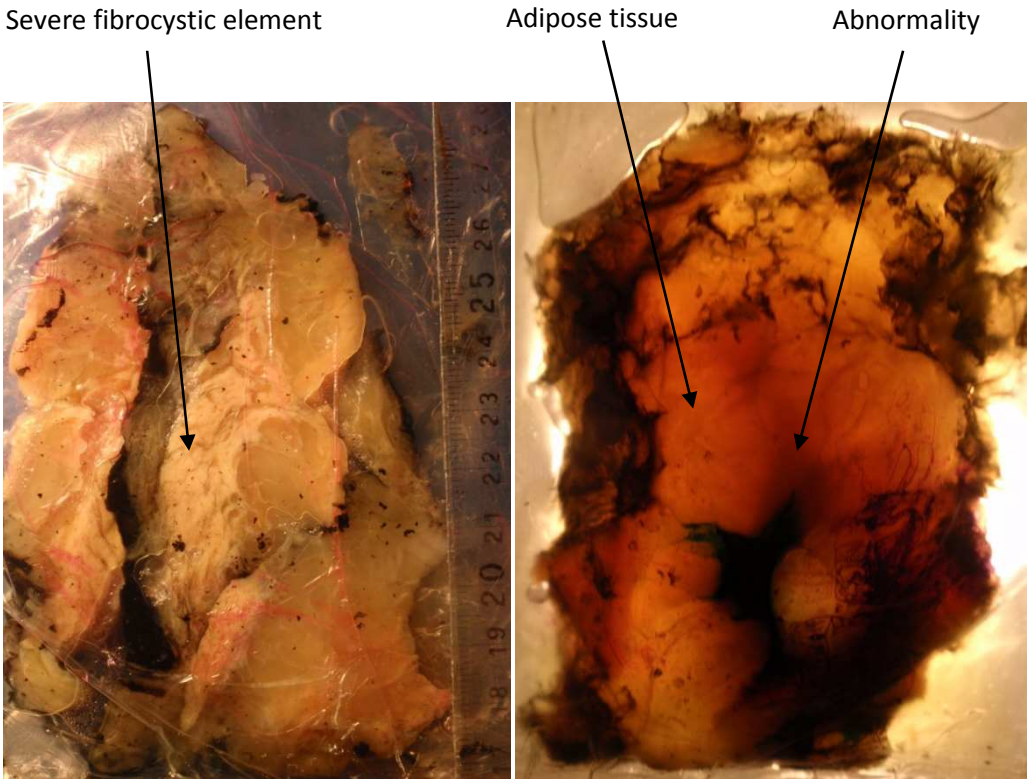

(a) (b)

Figure 2.8 Photographs of the excised breast samples used to simulate the I-ImaS intelligent images. (a) sample one (b) sample two.

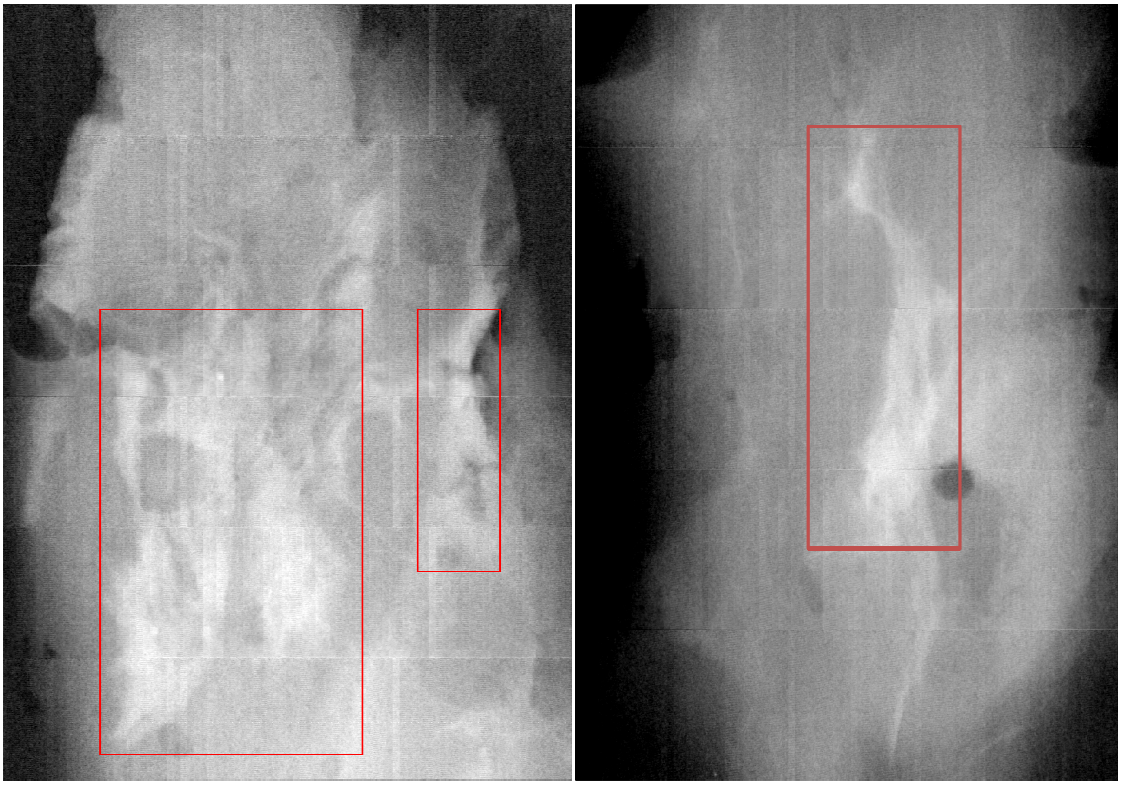

(a) (b)

Figure 2.9 Breast tissue regions marked as suspicious by radiologist. (a) Corresponding to sample 1 and (b) corresponds to sample 2.

2.7 X-ray characterisation of the I-ImaS sensors

This section describes the x-ray characterisation methods used to evaluate the I-ImaS sensors in the frequency domain. Parameters investigated include the Modulation Transfer Function (MTF), Noise Power Spectra (NPS) and the Detective Quantum Efficiency (DQE) which are descriptors of detector spatial resolution, system noise transfer and total signal transfer through the imaging system respectively.

2.7.1 X-ray response

As the detector within a digital imaging system has to have a linear response in order to investigate its performance using Fourier analysis, the I-ImaS detector response was measured using a range of mAs settings for a given kV consequently giving rise to a response curve. The region of the detector with a linear response was determined.

2.7.2 Modulation transfer function (MTF)

The MTF describes a system's response to an input signal (single frequency sinusoid (u)) over a range of spatial frequencies:

$$\mathrm{MTF_d}\,(u) = \frac{|FT_d(u)|}{|FT_{in\,(u)}|} \qquad \text{(Eq. 2.5)}$$

Where FT_{in} and FT_d are the amplitudes of the sinusoid before and after sampling respectively (Dobbins (1995)). The MTF is obtained by a Fourier transform (FT) of a finely sampled line spread function (LSF) (Eq 2.6).

$$\mathrm{MTF}_d(u) = FT\{LSF(x)\} \qquad \text{(Eq. 2.6)}$$

Where LSF(*x*) is the line spread function.

In order to obtain a true estimate of the characteristic frequency response of a digital imaging system, i.e. the MTF, it is required that the imaging system have a linear response, where the output data from the system is linearly related to the input data. Also, the avoidance of aliasing due to undersampling is required as it

results in the MTF no longer being the transfer amplitude of a single frequency component. Aliasing causes frequencies sampled above the Nyquist frequency to mimic frequencies below the Nyquist frequency. This occurs when the signal is not sampled finely enough to record the entire frequency spectrum.

The oversampled LSF can be measured using the slanted slit technique described in detail by Fujita et al (1992). The slit is carefully placed in front of the detector at a slight angle with respect to the detector pixels of approximately 2°. The slit image is corrected for sensor offsets and beam nonuniformities as expressed in equation 2.7 (Elbakri et al (2009) and Arvanitis et al (2007)):

$$\bar{I}_{cor}(x,y) = \frac{\bar{I}_{raw}(x,y) - \bar{I}_{dk}(x,y)}{\bar{I}_{wi}(x,y) - \bar{I}_{dk}(x,y)} \times \overline{(\bar{I}_{wi} - \bar{I}_{dk})} \qquad \text{(Eq 2.7)}$$

Where $\bar{I}_{cor}$ is the average corrected image, $\bar{I}_{raw}$ is the average raw image, $\bar{I}_{dk}$ is the averaged dark field value and $\bar{I}_{wi}$ is the average flat field image.

The slit image is then normalised with the integral of the digital values perpendicular to the slit in order to correct for any edge inhomogeneities or variations in slit width (fig 2.10) (Dobbins et al (1995) and Beutel et al (2000)). The angle is determined using a plot of the transverse profile maximum along the length of the slit (Dobbins et al (1995)) as shown in figure 2.11 .The local minima represents the point at which the slit centre is half way between two pixels whilst the local maxima indicates where the centre of the slit is directly above the centre of the pixel. The pixel distance (d) between local minima consequently enables the slit angle to be computed:

$$\tan(\theta) = \frac{1}{d} \qquad \text{(Eq. 2.8)}$$

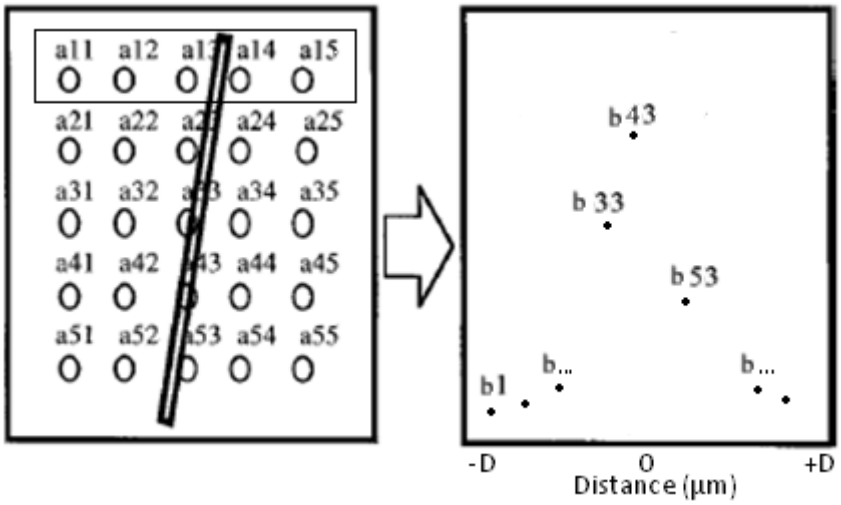

$$\mathrm{b1} = \frac{a11}{(a11 + a12 + a13 + a14 + a15)}$$

Figure 2.10 Illustration of perpendicular integrals for slit normalisation procedure correcting for slit imperfections.

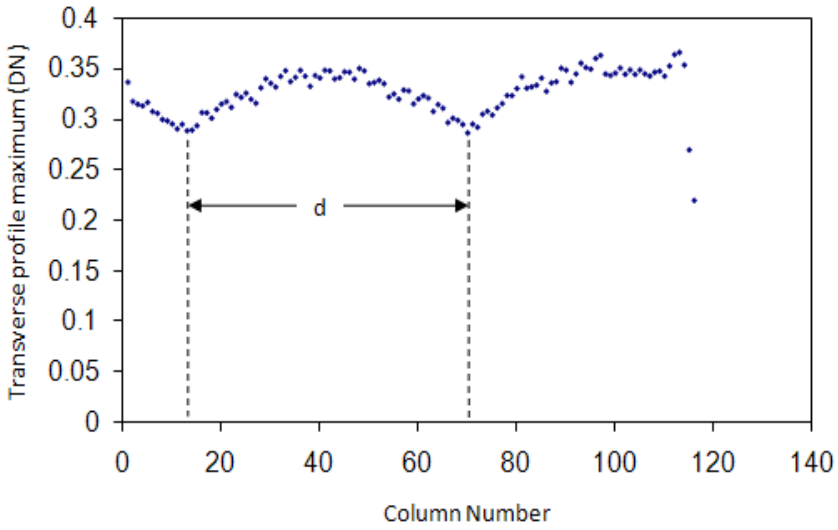

Figure 2.11 Determination of the traverse profile maximum along the length of the slit.

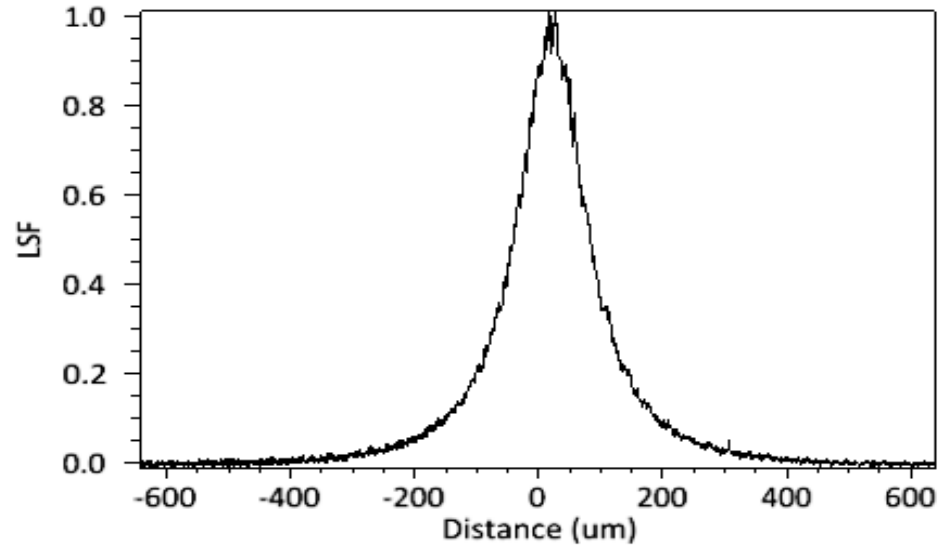

Figure 2.12 The normalised oversampled LSF of the I-ImaS sensor coupled to 100µm CsI.

The LSF (fig 2.12) is computed by plotting the image intensity versus distance from the centre of the slit for each pixel in a ROI surrounding the slit (Dobbins et al (1995)). The LSF is then Fourier transformed giving rise to the MTF which is then normalised at its maximum to unity. The MTF is then deconvolved in the frequency domain using the sinc function giving rise to the true presampled MTF (eq 2.9).

$$\mathrm{MTF}_{\mathrm{true}}(f) = \frac{MTF_d\,(f)}{Sinc_{slit}\,(f)} \qquad \text{(Eq. 2.9)}$$

Where $\mathrm{sinc}_{\mathrm{slit}}(f)$ estimates the slit width.

2.7.3 Noise Power Spectrum (NPS)

The noise power spectrum is a two dimensional spectral decomposition of the variance which may be estimated either from the Fourier transform of the autocorrelation function (indirect method) or from the square of the modulus of

the Fourier transform of the raw data as shown below (direct method) (William et al (1999)):

$$\mathrm{NPS}(u,v) = \frac{\langle |FT(u,v)|^2 \rangle}{N_x . N_y} . \Delta_x . \Delta_y \qquad \text{(Eq. 2.10)}$$

Where $\langle |FT(u,v)|^2 \rangle$ represents the ensemble average of the squares of the FT data, N_x and N_y are the number of elements in the x and y direction respectively (which is equal to the size of the ROI used), Δ_x and Δ_y are the pixel pitch in the x and y direction respectively.

The NPS is commonly estimated using the direct method according to Samei (2003) where the 1-D normalised noise power spectrum (NNPS) is derived from the measured 2-D NPS as shown below (eq 2.11).

$$\mathrm{NNPS}(f) = \frac{NPS(u,v)}{(Mean\ ROI\ signal)^2} \qquad \text{(Eq. 2.11)}$$

Where $(Mean\ ROI\ signal)^2$ is expressed in digital units.

The 1-D NNPS is used as it enables the computation of the DQE estimation. The direct method is used as it gives rise to both, the 1-D NNPS and the 2-D NPS therefore provides additional noise information such as the presence or absence of any off axis noise peaks that may not have been visible if only the 1-D NNPS was observed.

The 1-D NNPS is one of the most common metrics describing the noise properties of an imaging system serving as a noise characteristic estimate of the true NPS. This estimate is obtained rather than the true NPS, as in practice, only

a finite amount of data is available for analysis, therefore leading to a finite number of samples making up the ensemble average (William et al (1999)). Consequently, a compromise must be established between the size of each ROI and the number of ROIs in the ensemble average (Dobbins et al (2006)).

In order to suppress offset and background trends such as those introduced by the heel effect, leakage current or mains pickup which can artificially inflate the low frequency NPS (Vedantham et al (2000)), a second-order polynomial fit is used in an attempt to eliminate these trends (Arvanitis et al (2007)). Such detrending techniques have been proven to be highly effective at reducing the low frequency noise power from within the spectrum as shown by several authors (William et al (1999), Vedantham et al (2000) and Arvanitis et al (2007)).

In order to compute a smooth one-dimensional plot, the 1-D NNPS is estimated from a thick slice of the 2-D NPS comprised of eight lines on either side of the u and v axis (excluding the axis) grouped into frequency bins 0.1mm^{-1}. The frequency for each data value (*u, v*) is computed as $\sqrt{(u^2 + v^2)}$.

2.7.4 Detective quantum efficiency (DQE)

Traditionally, detective quantum efficiency (DQE) describes the efficiency with which the signal-to-noise ratio (SNR) is transferred from the input to the output of an imaging system (Kandarakis et al (1997)) as expressed in equation 2.12. It is commonly computed as a function of frequency (Nishikawa and Yaffe (1990) and Monnin et al (2007)) and is written as expressed in equation 2.13.

$$\mathrm{DQE} = \frac{\mathrm{SNR}_{\mathrm{out}}^2}{SNR_{in}^2} \qquad \text{(Eq. 2.12)}$$

$$\mathrm{DQE}(f) = \frac{\mathrm{MTF}^2(f)}{\mathrm{NNPS}(f).q} \qquad \text{(Eq. 2.13)}$$

Where SNR_{out} and SNR_{in} are the output and input SNR, MTF(*f*) represents the modulation transfer function, NNPS(*f*) is the normalised one-dimension noise power spectrum and q is the x-ray photon flux per unit area incident on the detector (x-ray photons/mm^2).

The photon flux per unit area was determined using the measured exposure integrated over the normalised spectral distribution (Johns and Cunningham (1983)). The x-ray spectrum was simulated using commercially available spectrum generator software (Nowotny and Hvfer (1985) and Meyer et al (2004)) which was normalised and scaled with the measured exposure. The exposure measurements were made in air where the ion chamber was placed at the source to detector distance replacing the detector.

2.8 Materials and Methods

2.8.1 X-ray response

The detector response curve was generated by acquiring flat field images over a range of mAs settings at 30kV. Mean pixel values were then determined from a centrally located, 35 pixel × 100 pixel region of interest enabling the sensor pixels to be averaged. This rectangular area was chosen as the sensor itself was only 40 pixels × 512 pixel in size. The exposure values were measured using a 15cc calibrated Fluke Biomedical ionisation chamber (model: 96035B) along with a KEITHLEY electrometer (model: 35050A). The chamber was calibrated at 70kV

and 30kV where calibration is traceable to Physikalishc-Technische Bundesantalt calibration report number 24969-1. It was positioned in place of the detector at the same source to detector distance used to acquire all subsequent experimental data. In an attempt to replicate a clinical spectrum the x-ray beam was hardened using a 38mm block of PMMA (simulating a thin compressed breast) which was mounted onto the x-ray tube housing in order to reduce the amount of scatter introduced by the PMMA block reaching the detector. PMMA was used as it is a well accepted breast tissue equivalent material (White and Tucker (1980)). The values of mean pixel intensity (DN) were then plotted against incident exposure.

2.8.2 MTF

The presampled modulation transfer function was measured using the slanted slit technique described in detail by Fujita et al (1992) and summarised in section 2.7. The slit camera comprised of a 1.5mm thick tantalum disk incorporating a 10µm (±1µm) wide by 5.5mm long slit (MA4976 Gammex rmi). It was carefully placed 2mm in front of the detector (leading to a magnification of 1.006 hence removing the effect of focal spot size) at a small angle (<2°) with respect to the vertical pixel array. The slit was imaged using x-ray tube setting of 40kV and 10mAs.

2.8.3 NPS

The NPS was estimated using the direct method according to Samei (2003) where the 1-D NNPS was estimated from the measured 2-D NPS. The effect of exposure on the NNPS was investigated where fifty five flat field images were acquired at five different incident exposure settings (0.00, 0.09, 0.30, 0.45 and

1.00μCkg^{-1}). A constant source to detector distance of 630mm was maintained. The exposures were determined experimentally using the 15cc calibrated Fluke Biomedical ionisation chamber (model: 96035B) attached to the KEITHLEY electrometer (model: 35050A) which was positioned in place of the detector; these measurements were made in air. The flat field images were output from the imaging system as raw data. Due to sensor size limitations, 15 32 pixel × 32 pixel non-overlapping ROIs were taken from each image for all 55 images providing 825 ROIs. Consequently, the NPS was an ensemble of 825 spectra; this resulted in a standard error of 3.4%. The 1-D NNPS was estimated from a thick slice of the 2-D NPS comprised of 8 lines on either side of the axis therefore providing 8 lines × 2 sides × 32 frequency bins = 512 data values per 0.1mm^{-1} frequency bin.

2.9 Results

2.9.1 X-ray response

The measured characteristic curve of a single I-ImaS sensor element is shown in figure 2.13. It is observed that the response has a correlation coefficient value (R^2) of 0.9997 at low pixel intensity values. This therefore enables the assumption that the sensor is linear within reason for a given range (at low pixel intensity levels) to be made. Using this linear region for the remainder of the sensor characterisation investigation therefore accounts for any non-linearity's associated with the sensor.

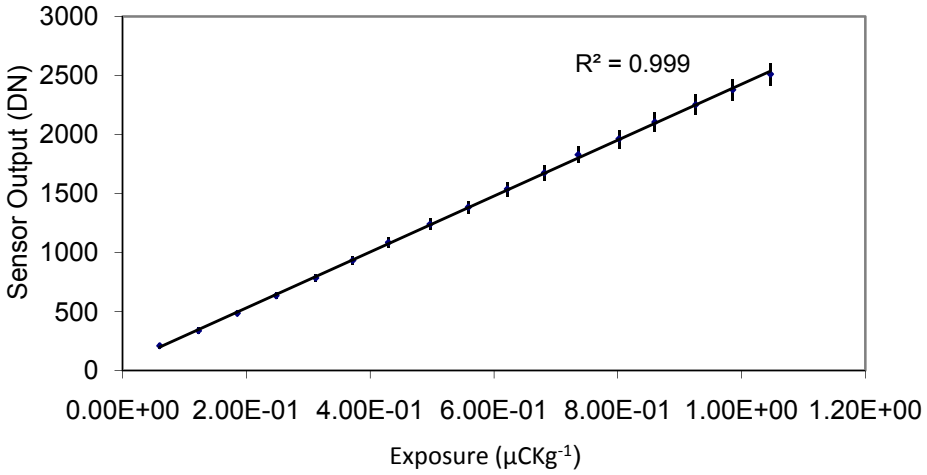

Figure 2.13 Sensor x-ray response where data points represent the mean intensity of the image expressed in digital numbers.

2.9.2 MTF

The measured presampled MTF of the I-ImaS system is shown in figure 2.14. The MTF of the system appears to fall to 10% at approximately 6 lp/mm. This is believed to be partly due to the imperfect coupling of the scintillator to the sensor. Another possible factor restricting the resolution is the quality of the columns within the structured CsI itself. Imperfections in the columnar structure would result in undesirable light diffusion through the path of the scintillator towards the sensor consequently contributing to MTF degradation. Although the MTF is an important descriptor of an imaging system's spatial resolution performance, this parameter alone does not act as a complete performance indicator. The NPS and DQE metrics provide additional information which should be considered.

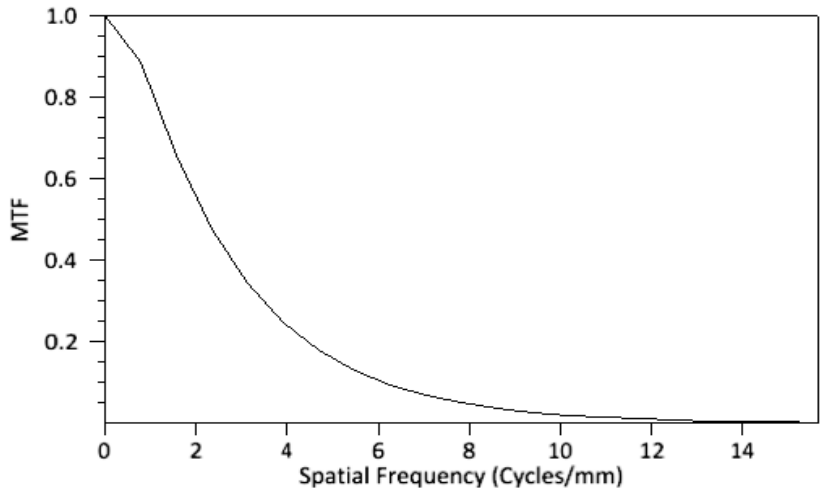

Figure 2.14 The presampled MTF plot of the I-ImaS sensor coupled to a 100µm structured CsI:TI scintillator.

2.9.3 NPS

The 2D NPS obtained at 0.00, 0.09, 0.30, 0.45 and 1.00µCkg^{-1} are shown in figure 2.15. These results illustrate a common fact seen throughout the literature, (William et al (1999) and Samei and Flynn (2003)) that is noise increases as exposure is increased. However when normalised with the mean signal, the reverse is true as can be seen from figure 2.16. It is seen that at higher exposures (Fig 2.15d and 2.15e) the NPS appears noisier than those obtained at lower exposures (Fig 2.15a and 2.15b) which possess the characteristic grain like effect as a result of the relative amount of quantum noise on the detector.

It is thought that the quantum noise along with contributions from CsI mottle noise is the reason for the varying shape of the curves with exposure where a more elliptically shaped noise contribution is seen at 0.09µCkg^{-1} and 0.30µCkg^{-1} in contrast to higher exposures where the noise component appears to be contributed to more equally in all directions as the spectra appear to be more

radial in shape. The higher noise component seen on the vertical axis at zero frequency is thought to be associated with nonstationary electromagnetic fluctuations (pick up noise) arising from the row select transistors of the imager during readout (Siewerdsen et al (1998)). Spikes commonly associated with uncorrected fixed pattern noise or fiber optic plate mismatches are observed (Williams et al (1999) along the horizontal axis appearing at approximately 4 and 8 cycles/mm. It is also observed from the 2D NPS that noise spikes are present in the corners of the images, as these spikes are present in the dark images it is likely that they are a form of internal high frequency EMI noise arising from one of the numerous electronic components on the DAQ. The results shown in figure 2.16 provide indication that once normalised, the noise is inversely proportional to the exposure level, and also that at lower spatial frequencies, a higher noise content is exhibited. The noise amplitude fluctuations are seen at approximately 4 cycles/mm and 8 cycles/mm and are believed to be associated with FOP mismatches.

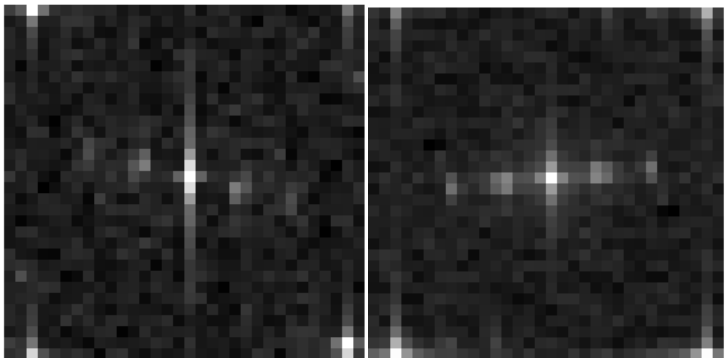

(a) (b)

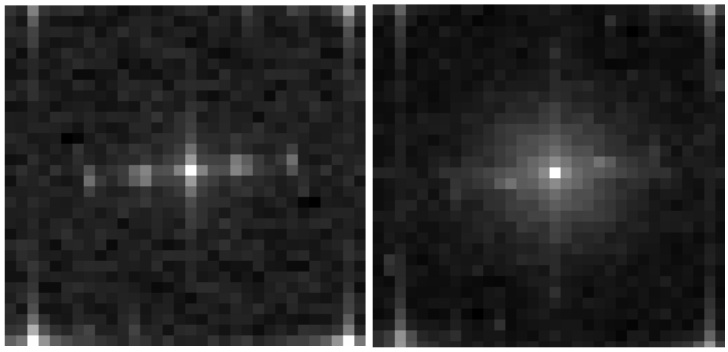

(c) (d)

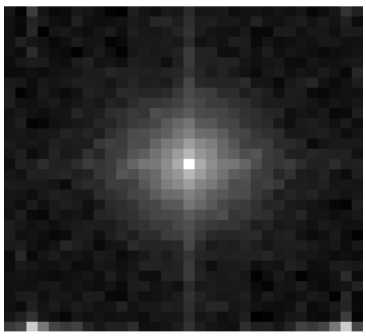

(e)

Figure 2.15 2-D NPS for all exposures investigated illustrating noise components not seen in 1-D spectrum where (a) illustrates the 0.00 (b) 0.09 (c) 0.30 (d) 0.45 and (e) 1.00μCkg^{-1}

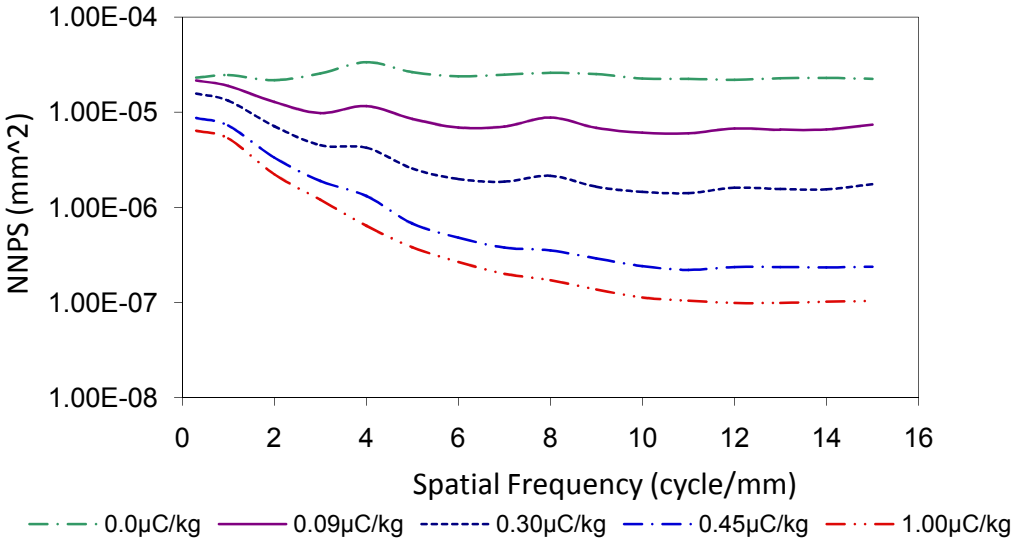

Figure 2.16 Comparison of 1-D normalised noise power spectrum obtained at all exposure settings investigated.

2.9.4 DQE

The DQE was determined according to equation 2.13 and the result is displayed in figure 2.17. The DQE close to zero frequency was 0.30 with a detector entrance exposure of 0.45µCkg^{-1}, the measured x-ray photon flux incident on the detector was 3.2×10^5 photons/mm^2. The drop in DQE seen at 4 cycles/mm is consistent with the 1D NNPS discussed above and is thought to be due to low frequency noise components arising from electromagnetic pick up noise. The low DQE value at higher spatial frequencies is associated with the non ideal CsI sensor coupling. It is thought that a higher DQE at lower spatial frequencies may be obtainable if a thicker fiber optic plate and better scintillator coupling was introduced.

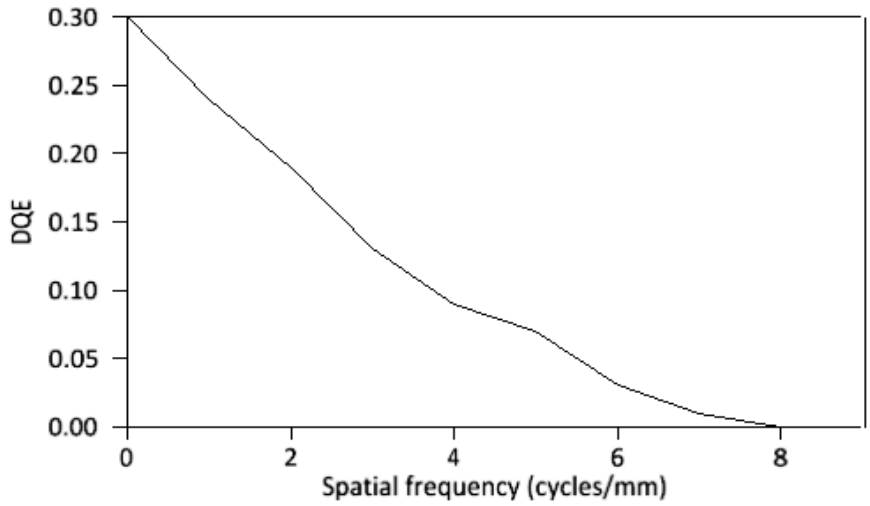

Figure 2.17 The DQE of system configuration utilising the I-ImaS sensor coupled to the structured CsI:TI scintillator. Obtained with a sensor surface exposure of 0.45µCkg^{-1}.

2.10 Summary

Care was first taken in determining the exposure response of the system as a linear-system response is generally necessary to characterise the system using Fourier analysis. The spatial resolution offered by the CsI:TI coupled I-ImaS sensors is superior (6 lp/mm at 10% MTF) to the Sensographe 2000D (5 lp/mm at 10% MTF) which is the most commonly used commercially available indirect digital mammography imager (Monnin et al (2007) . The NPS indicates that the use of a higher incident exposure would be desirable reducing the noise power at mid to high spatial frequencies consequently increasing the likelihood of Microcalcification detection. As this system was intended for use in mammography, the exposure is therefore limited due to strict dose constraints. The DQE was estimated to be 0.3 at close to zero frequency. This indicates that for low dose mammography, the system is not very efficient at using the incident quanta to form an image. Consequently, as DQE increases with exposure, an increased exposure is recommended. The overall performance characteristics of

the I-ImaS system suggest that the system has the capabilities to be used as a medical imaging system and should be investigated further.

Chapter Three

Feature extraction using statistical feature functions & EDXRD

3.1 Introduction

This chapter explores the intelligent imaging concept. It has been proposed that the imaging parameters used to obtain a mammogram can be optimised in real time. This optimisation procedure would be implemented in one of two ways, either via a feedback mechanism based on information extracted from a low exposure image during the imaging process, or, via the feedback of an EDXRD signal.

The former technique would therefore require a means of extracting information contained within the partial mammogram and determining whether the tissue is suspicious or not. As this decision making feedback loop would have to be performed in real-time, excessive computational times would have to be avoided requiring the mechanism to be of low computational complexity.

As discussed in chapter one, the use of automated global image enhancement is currently available in the form of Automated Exposure Control (AEC), which acts to find and set the optimal imaging conditions for a given breast (Pisano and Yaffe (2005)). This technique often results in over and under exposed tissue regions which are far from ideal (Elbakri et al (2005)). The technique proposed by the I-ImaS system of first extracting then identifying information signatures from the content rich image in an attempt to optimise the imaging parameters to local as opposed to global tissue regions overcomes this limitation. This would consequently result in an image being obtained with more than one incident exposure, an 'intelligent image'. The ability to control the imaging parameters for a given region of interest would ultimately result in a more efficient exposure distribution where diseased tissue regions could be imaged at higher exposure to that of healthy tissue regions. As a consequence of this exposure optimisation,

risk to healthy tissue would be minimised whilst maintaining or potentially increasing the contrast between healthy and suspicious tissue regions.

The investigation as to whether the real time parameter optimisation technique is possible is considered in this chapter where it has been experimentally demonstrated that the proposed concept is possible using simple statistical feature functions as a means of information extraction.

An alternative breast tissue information extraction technique for implementation into the I-ImaS parameter control system was also investigated. The proven tissue differentiation capability of EDXRD is considered**.** As the I-ImaS system was custom built for transmission imaging only, it was therefore necessary to conduct a separate experiment in order to extract and determine whether EDXRD signals could serve as an intelligent input parameter, controlling the imaging parameters of the I-ImaS system in real time. Two experiments were setup, an EDXRD system in order to extract the coherent diffraction profiles from two breast tissue samples, and the second experiment used the I-ImaS imaging system in order to obtain conventional transmission images at several different incident exposures of the corresponding tissue regions pertaining to the same specimens consequently enabling the simulation of EDXRD guided intelligent transmission images.

The ultimate goal of this investigation is to demonstrate that the concept of using EDXRD signals obtained from the breast during a scan, therefore identifying suspicious tissue regions, can be used to optimise the imaging parameters in real time during data acquisition. This therefore introduces the potential to optimise the imaging parameters of a mammogram, via the use of an intelligent imaging system in real time during a scan. The ability to provide an increased or even

similar image quality whilst reducing the incident exposure to the breast would also prove desirable. However, in practice, this concept appears to be hindered by the fact that the exposure required to obtain diffraction signals from the breast is higher than the exposure used to obtain the conventional mammograms. This therefore means that the exposure used to obtain an EDXRD guided intelligent I-ImaS image, by default would require an increased incident exposure therefore requiring the optimisation of the EDXRD procedure.

3.2 Materials

3.2.1 Database images

To supplement the two tissue sample images, thirty three mammograms obtained from the publicly accessible Mammographic Image Analysis Society (MIAS) Mini-Mammographic Database were used (Suckling et al (1994)). The purpose of this investigation was to test the statistical feature functions on conventionally acquired mammograms, providing indication as to which feature functions could possibly be implemented into the steering algorithm; therefore used to generate intelligent I-ImaS images. As the database was specifically compiled in order for researchers to test and compare their algorithms, each mammogram had been digitised using a 200μm pixel where each image was of 1024 × 1024 pixels. Each mammogram was accompanied by appropriate information providing sample details such as background tissue type, abnormality type, abnormality location, abnormality size etc enabling various abnormality types and conditions to be investigated for the I-ImaS analysis.

3.2.2 Statistical feature functions for abnormality detection algorithm

The feedback mechanism used to drive the intelligence is of paramount importance and should ideally be based on information obtained from the breast itself. It is intended that the use of statistical functions that are able to consistently highlight changes in grey level trends, i.e. pixel intensities, be implemented into the feedback algorithm.

A preliminary study was undertaken within the I-ImaS consortium attempting to determine potentially useful statistical measures that could be eventually implemented into the feedback algorithm (I-ImaS (2005)). The investigation involved the evaluation of twenty statistical feature functions where nine of them were basic functions such as the mean, max, min, entropy etc. The remaining eleven were synthetic functions created by combining one or more of the original nine. Their capability to track image quality fluctuations with parameter change was investigated. It was concluded that eight of the twenty functions evaluated had the potential for I-ImaS system implementation subject to further verification (I-ImaS (2005)). The work presented here follows on from this preliminary investigation. A set of eight feature functions have been investigated with respects to their ability to consistently detect suspicious regions within mammograms, in order to find the best candidates for implementation into the real time image analysis procedure. Four of the eight functions were the same as some of those used previously (eq 3.1 – eq 3.4), and were selected firstly, based on their performance, and secondly, their simplicity. The remaining four functions were newly combined synthetic functions created by combining two of the initial four functions together. All eight functions were selected as they were simplistic, therefore having low computational times

complying with the strict time restraints, along with their potential suitability for grey level differentiation.

The statistical functions used for tissue information extraction are listed below:

- Minimum value

$$I_{min} = min\{I(x,y)\} \quad \text{(Eq. 3.1)}$$

- Maximum value

$$I_{max} = max\{I(x,y)\} \quad \text{(Eq. 3.2)}$$

- Mean Value

$$\mu = \frac{1}{N}\sum_{\mathrm{J}=0}^{\mathrm{N}-1} \mathrm{x_j} \quad \text{(Eq. 3.3)}$$

- Standard deviation

$$\sigma = \sqrt{\frac{1}{N-1}\sum_{\mathrm{J}=0}^{\mathrm{N}-1}(\mathrm{x_j} - \mu)^2} \quad \text{(Eq. 3.4)}$$

- Synthetic function 1

$$SynF_1 = (I_{max} - \mathrm{I_{min}})\mathrm{I_{max}}^2 \quad \text{(Eq. 3.5)}$$

- Synthetic function 2

$$SynF_2 = \frac{\mathrm{I_{max}}^2}{\mu} \quad \text{(Eq. 3.6)}$$

- Synthetic function 3

$$SynF_3 = (\mu \times I_{max})I_{max} \quad \text{(Eq. 3.7)}$$

- Synthetic function 4

$$SynF_4 = \mu \times \sigma \quad \text{(Eq. 3.8)}$$

3.2.3 Tissue differentiation: Threshold levels

The ability to differentiate between healthy and suspicious tissue regions from within a mammogram based on pixel intensity requires the use of a threshold value. This threshold serves as a trigger where once exceeded, the corresponding tissue region is then classified as suspicious. This differentiation procedure would usually be undertaken by a radiologist who would view mammograms of both the right and the left breast side by side before concluding whether the breast contained any potentially cancerous tissue regions; therefore possibly leading to re-examination.

The technique posed by the I-ImaS system makes use of a mammogram of a single breast obtained with a low exposure, first extracting and identifying information signatures from within the image prior to image parameter optimisation. The method used to derive the threshold values for each function was experimentally determined hence developed and optimised as the investigation went on.

In order for the system to highlight a region as suspicious, the thresholds of all the selected feature functions corresponding to the same tissue region have to be flagged as suspicious as to minimise the flagging of healthy regions incorrectly flagged by an individual function. This combining of individual functions ultimately leads to a single secondary feature function, the combined feature function.

3.3 Testing of the statistical feature functions

3.3.1 Preliminary feature function testing: Database images

The performance characteristics of the eight statistical feature functions were investigated using mammograms obtained from the MIAS Mammography database in an attempt to identify the most robust, stable and consistently performing functions within the set. This part of the study concentrated on the detection of microcalcifications and both malignant and benign well defined/circumscribed masses. These conditions were selected for investigation as microcalcifications indicate the presence of early breast cancer whilst circumscribed masses are commonly encountered. Once the database images were downloaded, they were categorised and placed into one of three appropriate folders based on the nature of the tissue type surrounding the abnormality (adipose, fatty glandular and dense glandular). A total of thirty three different mammograms were investigated. The images were then divided into strips (fig 3.4) corresponding to the height of the stepping ROI. Two strips from within each mammogram were selected and pertained to two different breast tissue regions, one containing an abnormality as shown in figure 3.4b, and the other comprised of healthy tissue alone (fig 3.4c). Two different regions were selected in order to have investigated the behaviour of the statistical functions both in the presence and absence of any abnormalities.

The underlying principle of the data processing procedure was to increase the pixel intensity difference between the healthy and suspicious tissue in order to allow statistical differentiation of the two regions. A global histogram equalization approach was used as it was an effective method of enhancing an entire low contrast image (Cheng et al (2006)). The pixels within each image

investigated within this chapter were re-assigned values between 0 and 255 where 0 presented the lowest pixel value and 255 represented the maximum pixel value within the image.

Statistical information from within a mammogram in the form of grey level pixel intensities was extracted using a stepping region of interest. The size of this ROI remained constant for all the database images investigated. They were analysed using a 5 × 75 pixel stepping region of interest whilst corresponded to a 1mm × 15mm I-ImaS pixel area. The ROI was stepped across the image in one pixel column steps where the feature functions were computed giving rise to a single representative value for that ROI (fig 3.1). Each ROI value yielded was independent of any previously obtained values and was solely governed by the pixel values within the immediate ROI being analysed. This value was compared to the threshold where it was determined whether the ROI was suspicious or not.

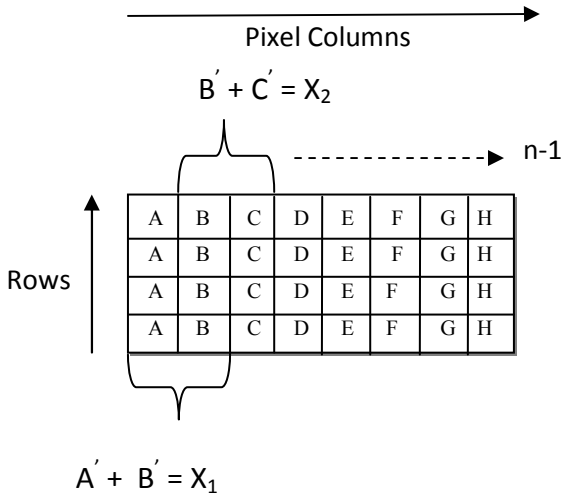

Figure 3.1 Schematic of stepping ROI where statistical results obtained from within ROI is stepped one column at a time.

3.3.2 Results of preliminary investigation

Selection of the best performing feature functions to be used within the I-ImaS feedback system was done by visually identifying numerical trends from within the feature function profiles as seen in figures 3.2 and 3.3. The feature functions that were able to enhance the grey level pixel intensity difference between healthy and suspicious tissue regions were selected. The profiles of all thirty three database mammograms were investigated.

The mammogram strip presented in figure 3.2 depicts a microcalcification cluster imbedded in adipose tissue. It can be observed from the feature function profiles that Max, $SynF_1$, $SynF_2$ and $SynF_3$ show distinct peaks corresponding to the abnormality only. The remaining feature functions prove ineffective at differentiating healthy from suspicious regions. Depicted in figure 3.3 is a mammogram strip containing a circumscribed lesion imbedded in adipose tissue. From the graphs, it can be seen that the Max, standard deviation and all of the synthetic feature functions are able to detected the abnormal region, however, it appears that $SynF_1$, $SynF_2$, $SynF_4$ and the standard deviation are able to distinctively highlight the suspicious region only. Consequently the max, $SynF_1$ and $SynF_2$ are the three common feature functions in both examples that consistently perform as required. Table 3.1 depicts the abnormality detection performance of using $SynF_1$ and $SynF_2$ as a combined feature function on all thirty three mammograms. It can be seen that this combined feature function has a 73% detection success rate hence will be the combined feature function used throughout this investigation.

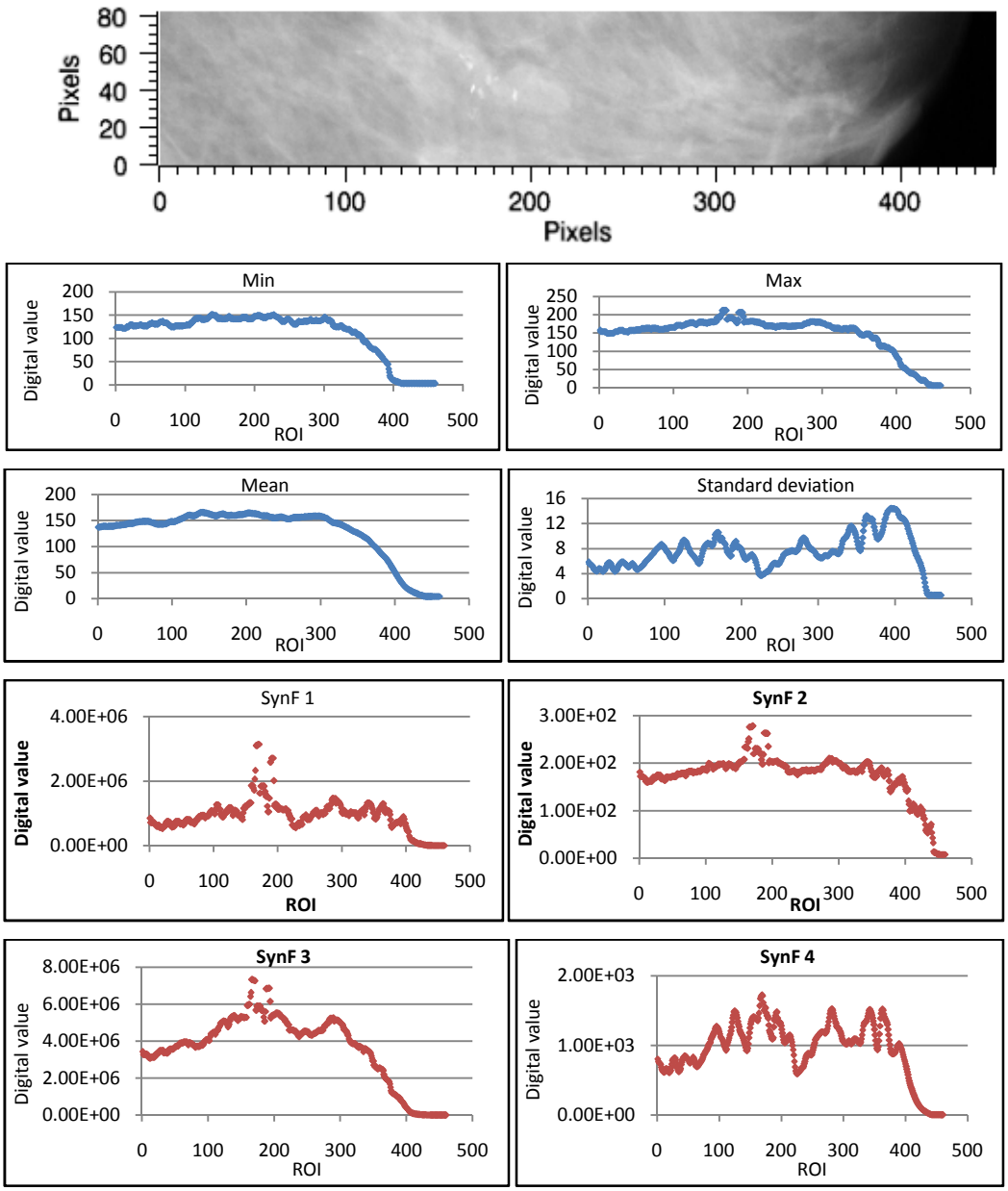

Figure 3.2 Strip of database mammogram containing a microcalcification cluster embedded in adipose tissue. Graphs depict results of the statistical feature functions.

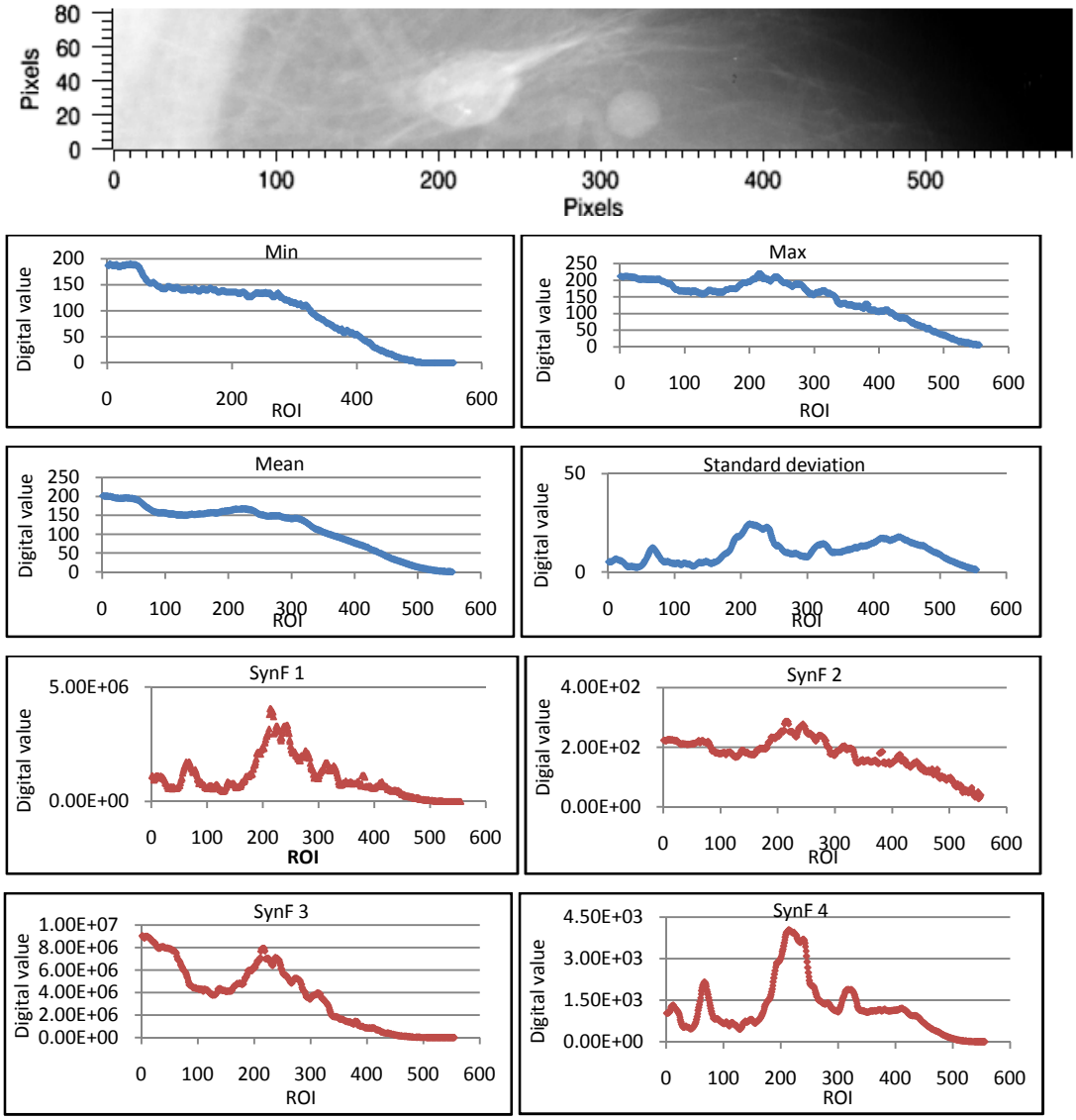

Figure 3.3 Strip of database mammogram containing a circumscribed lesion embedded in adipose tissue. Graphs depict results of the statistical feature functions.

Table 3.1 Results of the combined feature function analysis obtained from database mammograms.

Strip ID	Abnormality Type	Background tissue	Combined detection
1	μCal	Adipose	Yes
2	μCal	Adipose	Yes
3	μCal	Adipose	Yes
4	μCal	Adipose	Yes
5	μCal	Adipose	Yes
6	Circumscribed	Adipose	Yes
7	Circumscribed	Adipose	Yes
8	Circumscribed	Adipose	Yes
9	Circumscribed	Adipose	Yes
10	Circumscribed	Adipose	Yes
11	Circumscribed	Adipose	No
12	μCal	Fatty glandular	Yes
13	μCal	Fatty glandular	Yes
14	μCal	Fatty glandular	Yes
15	μCal	Fatty glandular	Yes
16	μCal	Fatty glandular	Yes
17	μCal	Fatty glandular	Yes
18	μCal	Fatty glandular	Yes
19	μCal	Fatty glandular	Yes
20	μCal	Fatty glandular	Yes
21	μCal	Fatty glandular	Yes
22	μCal	Fatty glandular	Yes
23	Circumscribed	Fatty glandular	No
24	Circumscribed	Fatty glandular	No
25	Circumscribed	Fatty glandular	Yes
26	Circumscribed	Fatty glandular	Yes
27	μCal	Dense glandular	Yes
28	μCal	Dense glandular	No
29	μCal	Dense glandular	No
30	μCal	Dense glandular	No
31	Circumscribed	Dense glandular	No
32	Circumscribed	Dense glandular	No
33	Circumscribed	Dense glandular	No
Total 33			**Detected: 24**

The threshold value pertaining to $SynF_1$ and $SynF_2$ were derived by either manipulation of the feature function itself as seen in equation 3.10, or observationally determined from analysing the results yielded from the database plots (eq 3.11). The ROI (eq 3.9) used to derive the threshold in equation 3.10 was taken from either the initial 32 pixel columns or final 32 pixel columns of breast tissue within each mammogram. This was done as the I-ImaS system would require the area immediately under the skin (edge of breast image) to be used as opposed to regions found mid way within the breast ensuring the maximum amount of tissue is scanned.

$$X_{ROI} = \frac{1}{NM}\sum_{x=1}^{N}\sum_{y=1}^{M} ROI(x,y) \qquad \text{(Eq. 3.9)}$$

Where X_{ROI} is the average value of the ROI comprised of N and M rows and columns respectively.

$$TV_{SynF1} = \left[\frac{1}{E}\sum_{e=1}^{E} X_{ROI}\,(e)\right] \times 1.5 \qquad \text{(Eq. 3.10)}$$

Where E=32

$$TV_{SynF2} = 250\ DN \qquad \text{(Eq. 3.11)}$$

Presented in figures 3.5, 3.7 and 3.9 are the results of both, the combined and selected individual feature functions obtained from figures 3.4, 3.6 and 3.8.

Figures 3.5a, b and c correspond to segment 3.4b and show that the benign well-defined/circumscribed mass, embedded in adipose tissue, is accurately highlighted as suspicious by both feature functions therefore the combined feature function also. Whilst highlighting the abnormal region, it can be seen that

the individual functions do well to minimise false flagging of the healthy tissue regions, therefore providing indication that the combined function has good specificity when used to analysis breast consisting predominantly of adipose tissue. Figures 3.5d, e and f correspond to the healthy image segment (3.4c) and illustrate that the condition governing the combined feature function is not satisfied. It can be observed that this is due to the fact that although both individual functions (fig 3.5d and e) flag regions within the image as suspicious, they do not correspond to a given location hence does not satisfy the combined feature functions predetermined condition.

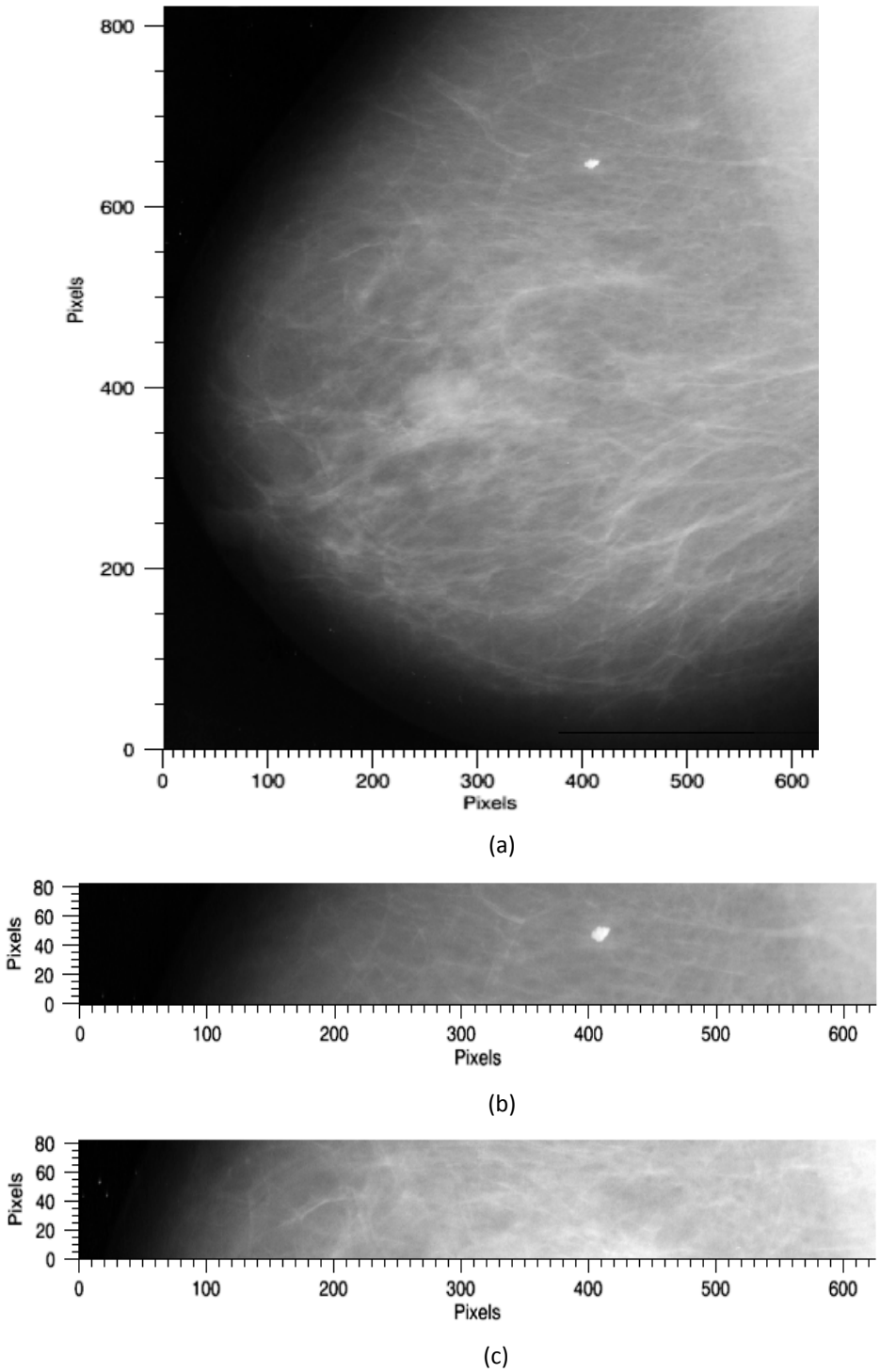

Figure 3.4 (a) Illustration of a mammogram containing a calcification embedded in adipose tissue downloaded from MIAS database (b) section of

mammogram containing abnormality analysed by statistical feature functions

(c) healthy segment of mammogram analysed by feature functions.

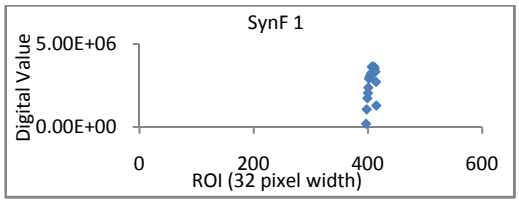

(a) Results from $SynF_1$ pertaining to 3.4b

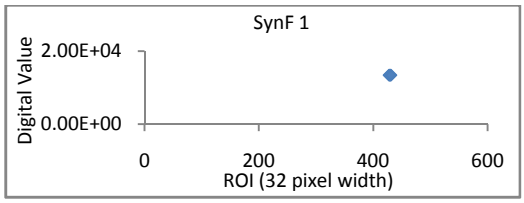

(d) Results from $SynF_1$ pertaining to 3.4c

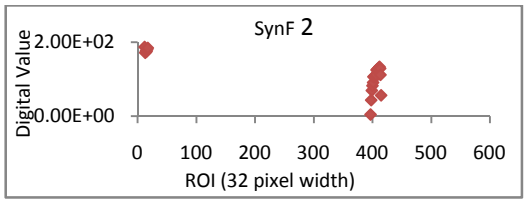

(b) Results from $SynF_2$ pertaining to 3.4b

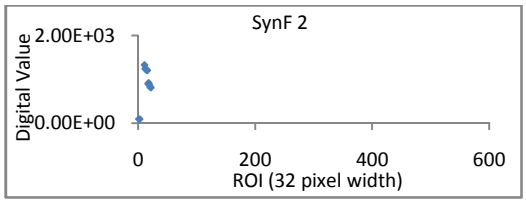

(e) Results from $SynF_2$ pertaining to 3.4c

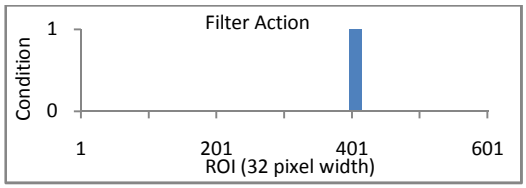

(c) Combined feature function figure 3.4b.

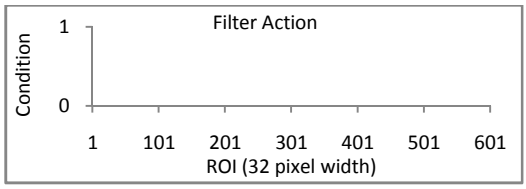

(f) Combined feature function figure 3.4c.

Figure 3.5 Results of statistical analysis yielded by $SynF_1$ and $SynF_2$ corresponding to figure 3.4.

Figure 3.6a shows a mammogram consisting of a benign calcification embedded in fatty glandular tissue (fig. 3.6b). The results of the statistical investigation corresponding to this abnormality are shown in figures 3.7a, b and c. Again, all three figures correlate well with the abnormality. The combined feature function does well to highlight this suspicious region only, regardless of the fact that both $SynF_1$ and $SynF_2$ flag other regions as suspicious. However, the healthy region incorrectly flagged by $SynF_1$ appears to correspond to the immediate surrounding tissue hence may potentially not be seen as a problem. The healthy

segment of the mammogram (fig 3.5c) appears to comprise of both adipose and glandular tissue types. A glandular region is seen to occupy the segment between approximately 190 pixels to 240 pixels and is reflected by $SynF_1$ (fig 3.6d). However, as this region goes undetected by $SynF_2$, no x-ray beam modulation is required (fig 3.6f).

Figure 3.8a depicts a mammogram containing a well-defined/circumscribed mass embedded in fatty glandular tissue as can be seen more closely in figure 3.8b. Both statistical feature functions highlight the suspicious mass only, as seen in figures 3.9a and b, therefore satisfying the predetermined condition which states that both feature functions must be flagged for a given location before an increase in exposure can be administered; hence figure 3.9c. Figure 3.9f shows that the healthy tissue segment is at no point treated as suspicious. However, it can be seen for a second time, that $SynF_1$ flags regions within the healthy tissue as suspicious therefore suggests that it is more sensitive to tissue changes than $SynF_2$.

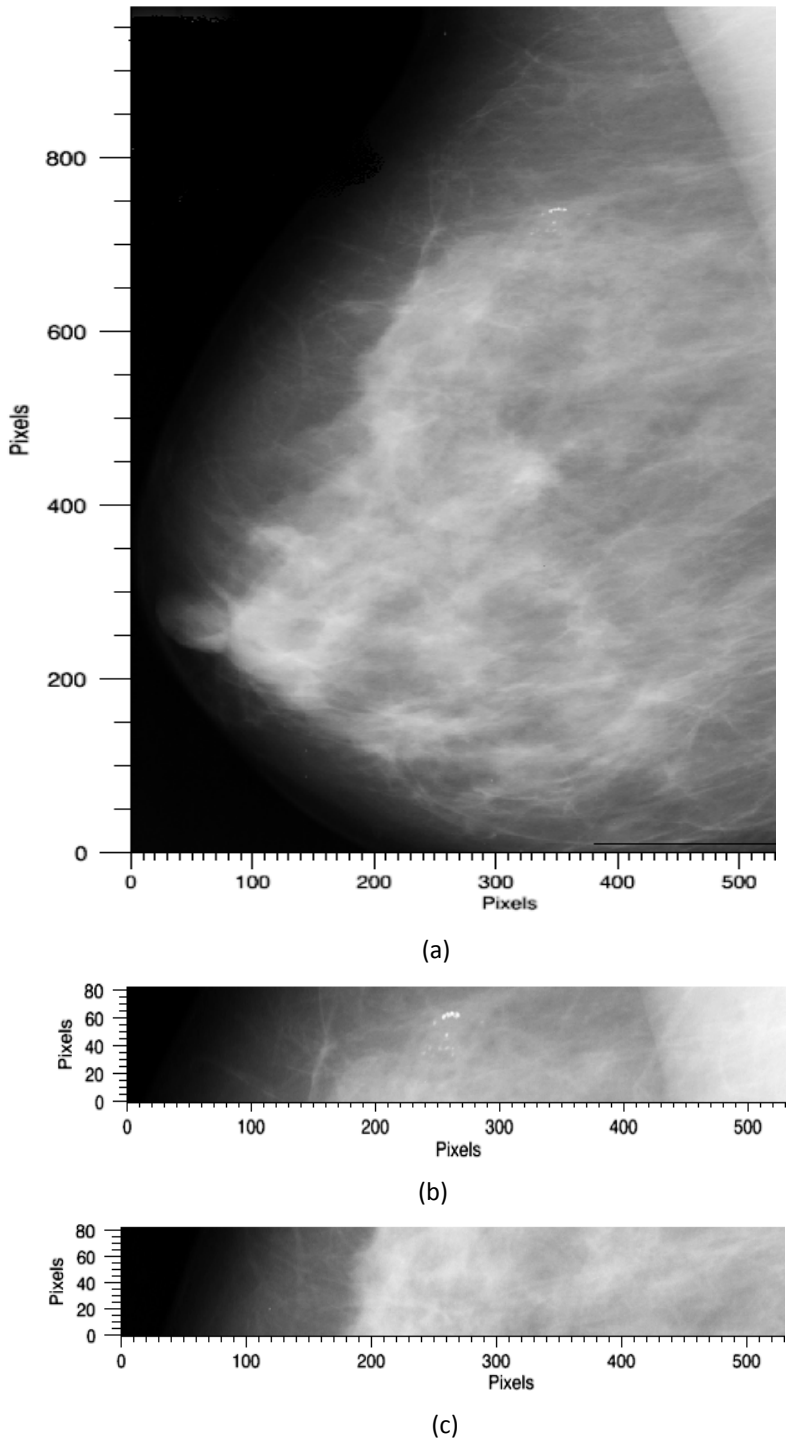

Figure 3.6 (a) Illustration of a mammogram containing a benign microcalcification embedded in fatty glandular tissue downloaded from MIAS database (b) section of

mammogram containing abnormalities analysed by statistical feature functions (c) healthy segment of mammogram analysed by feature functions.

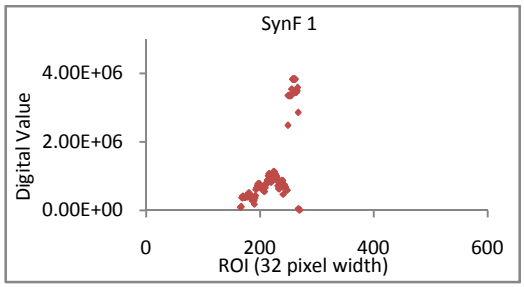

(a) Results from $SynF_1$ pertaining to 3.5b

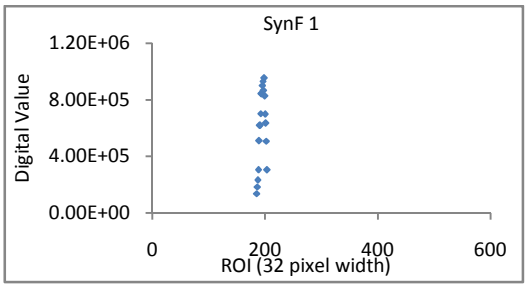

(d) Results from $SynF_1$ pertaining to 3.5c

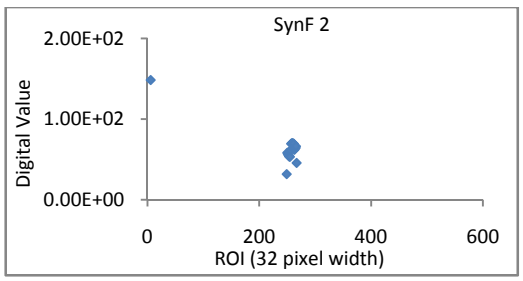

(b) Results from $SynF_2$ pertaining to 3.5b

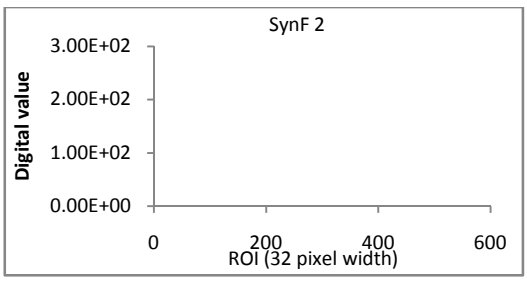

(e) Results from $SynF_2$ pertaining to 3.5c

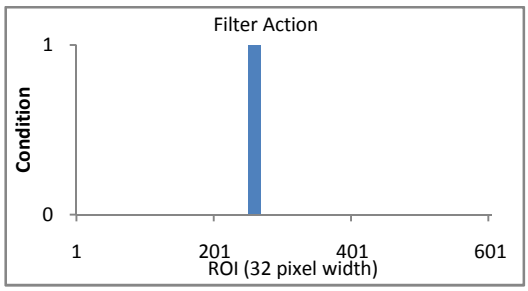

(c) Combined feature function yielded from a and b.

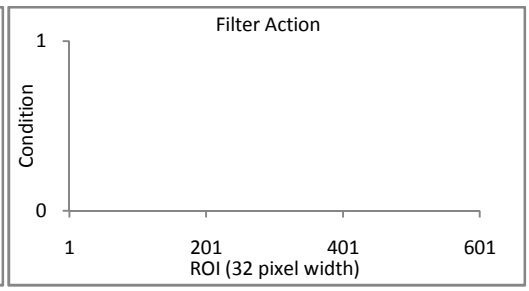

(f) Combined feature function yielded from d and e.

Figure 3.7 Results of statistical analysis yielded by $SynF_1$ and $SynF_2$ corresponding to figure 3.6.

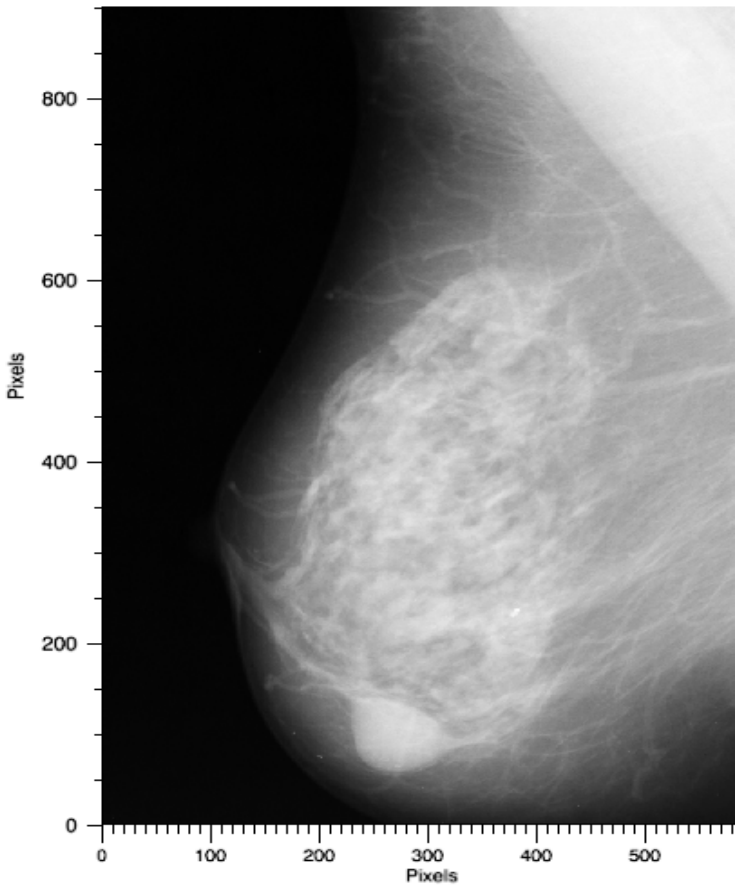

(a)

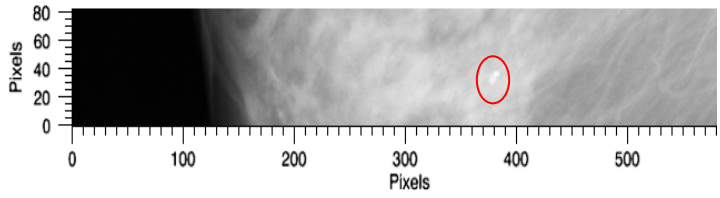

(b)

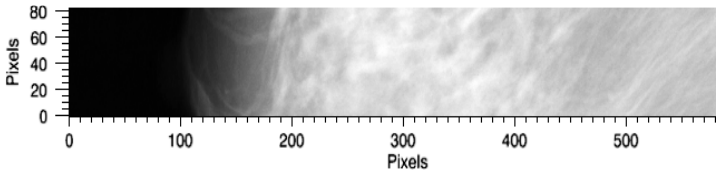

(c)

Figure 3.8 (a) Illustration of a mammogram containing a benign circumscribed mass embedded in fatty glandular tissue downloaded from MIAS database (b) section of mammogram containing abnormality analysed by statistical feature functions (c) healthy segment of mammogram analysed by feature functions.

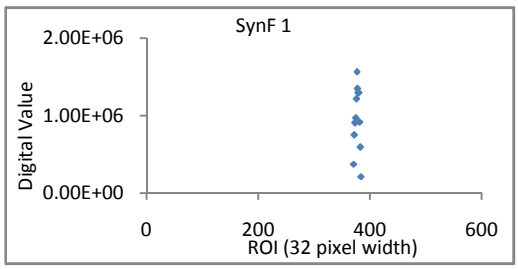

(a) Results from $SynF_1$ pertaining to 3.7b

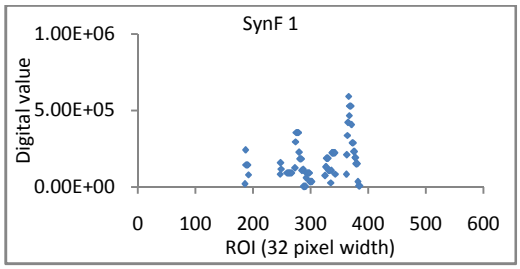

(d) Results from $SynF_1$ pertaining to 3.7c

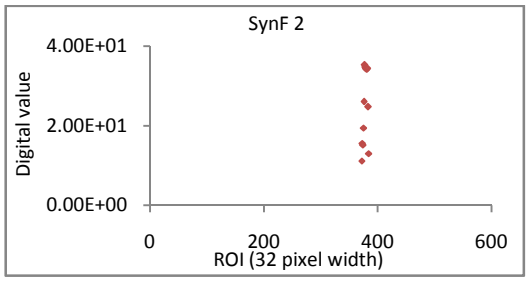

(b) Results from $SynF_2$ pertaining to 3.7b

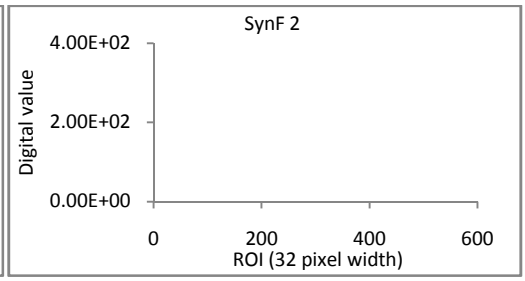

(e) Results from $SynF_2$ pertaining to 3.7c

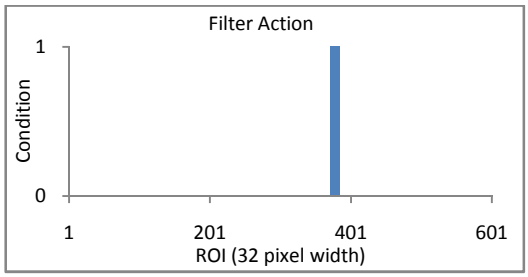

(c) Combined feature function from a and b

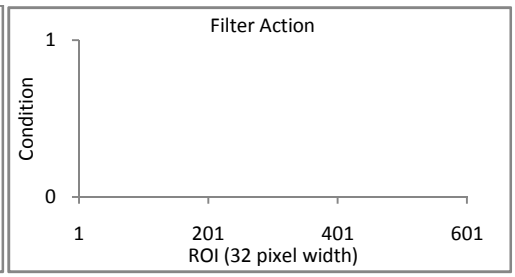

(f) Combined feature function from d and e

Figure 3.9 Results of statistical analysis yielded by $SynF_1$ and $SynF_2$ corresponding to figure 3.8.

From the results it has been demonstrated that the two selected feature functions, $SynF_1$ and $SynF_2$, are able to consistently highlight the abnormalities within the mammograms. The results imply that more than one feature function would increase specificity as it was seen that both feature functions at some point unnecessarily flagged healthy regions within the image. It was also

observed that the tissue-background border did not prove problematic (i.e. leading to false indications). This was due to the fact that these regions could only result in a decrease in pixel intensity; however, this consequently implies that such behaviour may possibly result in abnormalities close to the skin/background border going undetected. It has been demonstrated that abnormality detection using low complexity statistical feature functions is possible when at least two of the discussed functions are combined, therefore acting to reduce the proportion of healthy tissue unnecessarily highlighted. For the remainder of this investigation, $SynF_1$ and $SynF_2$ will be used in the combined fashion as shown above as a statistical information extraction tool.

3.4 Imaging parameter modulation

The previous section demonstrated the ability of the statistical feature functions to highlight abnormalities within the database mammograms; the next section reports the testing of the feature functions using mammogram segments obtained using the I-ImaS sensors in a conventional transmission imaging system.

During the initial phase of the I-ImaS project, the design and specification of the I-ImaS imaging system was investigated. The main objective during this phase was to identify the key aspects of a medical image which correspond to the level of diagnostic information contained within it enabling abnormality detection. This objective lead to the production of an End User Survey (EUS) which enabled the opinions of 62 medical imaging professionals (34 radiologists, 21 physicists and 7 radiographers) to be considered. The majority of the replies demonstrated that contrast resolution was the main feature both the radiologists and the physicists' thought needed improving. The results of the EUS concluded that an

increase in patient dose was undesirable and hence should be avoided; however, maintaining dose at current levels was acceptable providing an increase in diagnostic information was seen. All respondents agreed that lowering the patient dose was desirable provided that a significant reduction occurred (≥20%) (I-ImaS (2004)). It was also thought (85% of radiologists) that a very useful feature a new imaging system would possess would be the ability to optimally expose local regions of tissue therefore potentially leading to having optimal contrast at all points in the image.

The final I-ImaS design addressed the above issues. It was decided that a system with the ability to modulate the photon flux could potentially enable a more efficient way of exposing the breast. This would enable suspicious tissue regions to be imaged with a higher exposure than healthy regions, reducing the dose to the patient whilst potentially increasing image contrast. Intelligent imaging techniques that could be used to modulate the exposure required that a line scanning system be used enabling techniques such as modulation of the scan speed, where the scan speed would be slowed when imaging a suspicious region and speeded up when a non-suspicious regions is imaged; or modulation of the x-ray beam using attenuation filters. As the EUS reported a dose reduction of at least 20% was desirable, the use of attenuation filters would enable corresponding intensity reductions to be achieved. Modulation of the kVp was also considered, however it was thought that as the system is to perform in real time, rapid modulation of the kV would be challenging as the time required for it to be decreased and allowed to settle would be limited. Spatial resolution was also considered as a means of increasing the image quality to corresponding suspicious tissue regions. The benefit would only be fully appreciated in an imaging system using larger pixel sizes. Modulation of the spatial resolution also has the disadvantage of having no effect on patient dose.

It was decided that the final I-ImaS system would implement a smaller pixel size than is currently used within mammography in order to achieve the desired spatial resolution. The use of x-ray beam attenuation filters corresponding to exposure decrements of 20%, 40%, 60% and 80% were selected. This enabled the shape of the incident spectrum to be modulated, ultimately optimising exposure distribution.

3.5 Feature extraction

3.5.1 Transmission imaging

Simulation of an intelligent I-ImaS image requires that an image be made up of several segments of other images each obtained using a different incident exposure. This therefore required that the I-ImaS system be used in a conventional manor to obtain images of the two breast tissue specimens at five different incident exposures. The exposures used were 3.7, 8.2, 13.3, 19.0 and 24.8μCkg^{-1} corresponding to filter positions one, two, three, four and five respectively; therefore five images with different image qualities were produced. Consequently, the simulation of intelligently acquired images where local parameter adjustments based solely on the statistical information extracted from within the sample was now possible. Regions highlighted by the feedback algorithm as suspicious would correspond to tissue segments acquired using the maximum exposure (24.8μCkg^{-1}) whereas the remainder of the tissue would correspond to segments imaged with only the scout exposure (either 3.7, 8.2, 13.3 or 19.0μCkg^{-1}).

The tungsten anode x-ray tube assumed inherent filtration of 1mm of Al was used to image the tissue samples. It was operated in fluoroscopy mode at 30kVp and 7mA, corresponding to an incident exposure of 24.8µCkg^{-1} measured using an ionisation chamber (15cc Fluke Biomedical) and an electrometer (Keithley 35050A). The ion chamber replaced the tissue sample for the exposure measurement at the end of the experiment after the samples had been imaged. The I-ImaS attenuation filters were used to image the samples reducing the incident exposure at each filtration step accordingly. The I-ImaS system was operated in scanning mode where the TCP scanned the sample across the dual sensor array in 832µm (±3µm) steps where the final stitched image consisted of 95 steps.

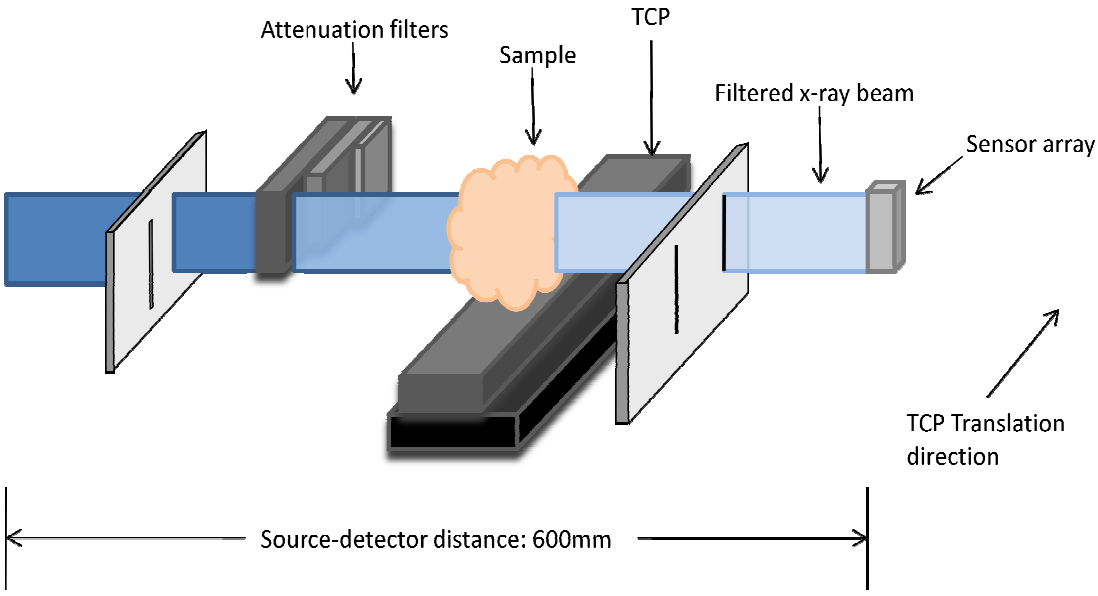

Figure 3.10 Simplified schematic illustrating the experimental setup used to acquire x-ray images of breast samples one and two using the I-ImaS system.

Figure 3.10 illustrates the experimental setup used to obtain the images. The samples were securely attached to a 5mm thick sheet of PMMA which was then fixed to the TCP. The PMMA sheet was used as it held the samples vertically whilst acting to eliminate any unwanted movement during the data acquisition phase. The final image was an average of 20 frames which were corrected pixel by pixel using equation 2.7 in order to compensate for x-ray beam non uniformities and sensor nonlinearities such as those introduced by the heel effect and pixel-pixel gain mismatches respectively. White fields were acquired using radiation without the sample present under identical exposure conditions, dark fields acquired with no x-ray exposure.

3.6 Working limitations of the combined feature function

As the combined feature function is required to perform on images acquired using some fraction of the incident exposure used to obtain conventional images (images acquired with a single exposure using no x-ray beam filtration), a range of incident exposures were investigated in order to have determined at what exposure level the combined feature function stopped reliably functioning. Eight different regions of interest from within breast sample one and two were selected for statistical investigation as can be seen from figure 3.11. Figures 3.11a – 3.11e are sections of tissue taken from breast sample one where images a - d are seen to comprise of both healthy and suspicious tissue. Figure 3.11e consists of healthy tissue alone. Image sections f - h are taken from tissue sample two and are all seen to consist of both healthy and suspicious tissue. The eight regions varied in size as suspicious tissue regions within each sample was limited. The heights of each segment corresponded to the height of the stepping ROI used (32 × 490 pixels). Each of the eight sample sections were imaged five times,

each time with a different incident exposure (see section 3.5.1), consequently resulting in the production and analysis of forty images. Each image containing a suspicious region was taken from the section of the breast marked as suspicious by the radiologist (see section 2.6).

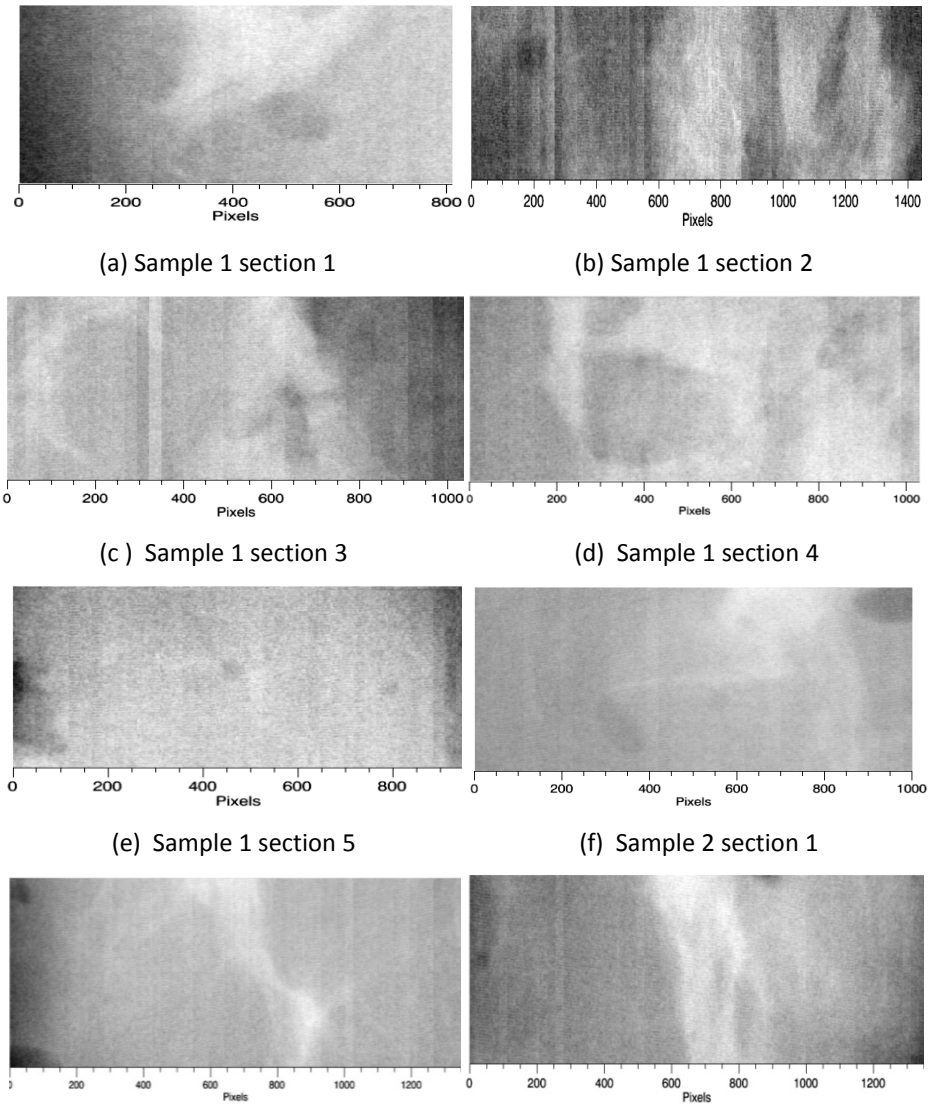

(a) Sample 1 section 1 (b) Sample 1 section 2

(c) Sample 1 section 3 (d) Sample 1 section 4

(e) Sample 1 section 5 (f) Sample 2 section 1

(g) Sample 2 section 2 (h) Sample 2 section 3

Figure 3.11 Regions of interest obtained from breast samples one and two used to evaluate the abnormality detection algorithm. Images obtained conventionally using the I-ImaS sensors implementing no intelligence at an incident exposure of 24.8µCkg^{-1}.

The image quality of all forty image segments was calculated in terms of the contrast to noise ratio (CNR) according to Young et al (2006) as shown in equation 3.12. This was done in order to have a means of comparison between each image segment at different exposure levels. The CNR would also serve as a

means of comparing the quality of these conventional images with the simulated intelligent I-ImaS images that are to be generated. The location of the ROI allocated for CNR determination within each tissue sample remained constant regardless of exposure used to acquire the image and can be seen within images a and f of figures 3.12, 3.13, 3.15 and 3.16.

$$\mathrm{CNR} = \frac{M_n - N_{sus}}{\sqrt{\frac{[sd_n^2 + sd_{sus}^2]}{2}}} \qquad \text{(Eq. 3.12)}$$

Where M_n, N_{sus}, sd^2_n and sd^2_{sus} represent the mean pixel value of the healthy ROI, mean pixel value of the suspicious ROI, standard deviation of the pixel values of the healthy ROI and the standard deviation of the suspicious ROI respectively.

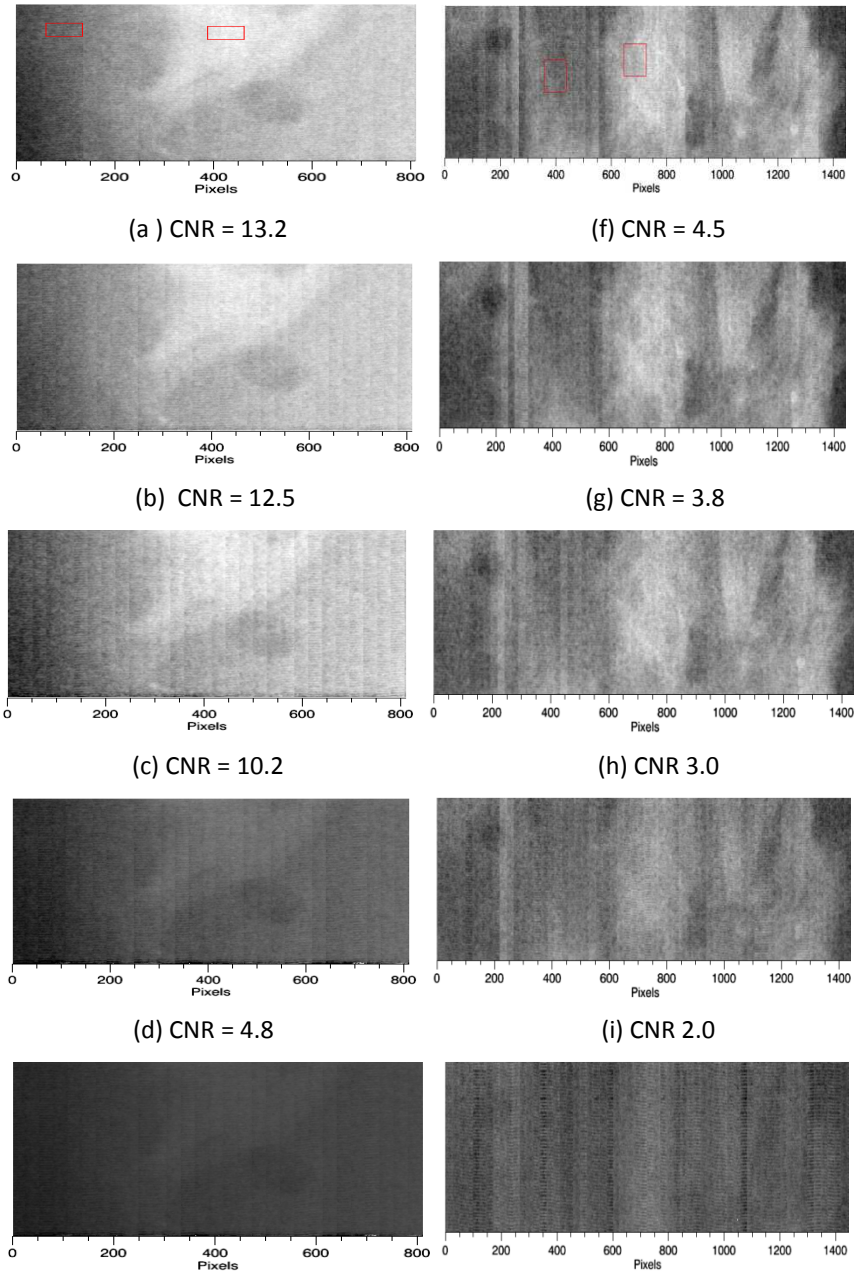

(a) CNR = 13.2 (f) CNR = 4.5

(b) CNR = 12.5 (g) CNR = 3.8

(c) CNR = 10.2 (h) CNR 3.0

(d) CNR = 4.8 (i) CNR 2.0

(e) CNR = 3.4. (j) CNR = 1.5

Figure 3.12 ROIs obtained from Sample 1 section 1 are illustrated in the left hand column, and ROIs obtained from Sample 1 section 2 are illustrated in the right hand column. All ROIs contain healthy and suspicious tissue types. Images a, b, c, d, e and f, g, h, i, j correspond to incident exposures of 24.8, 19.0, 13.3, 8.2 and 3.7µCkg^{-1} respectively.

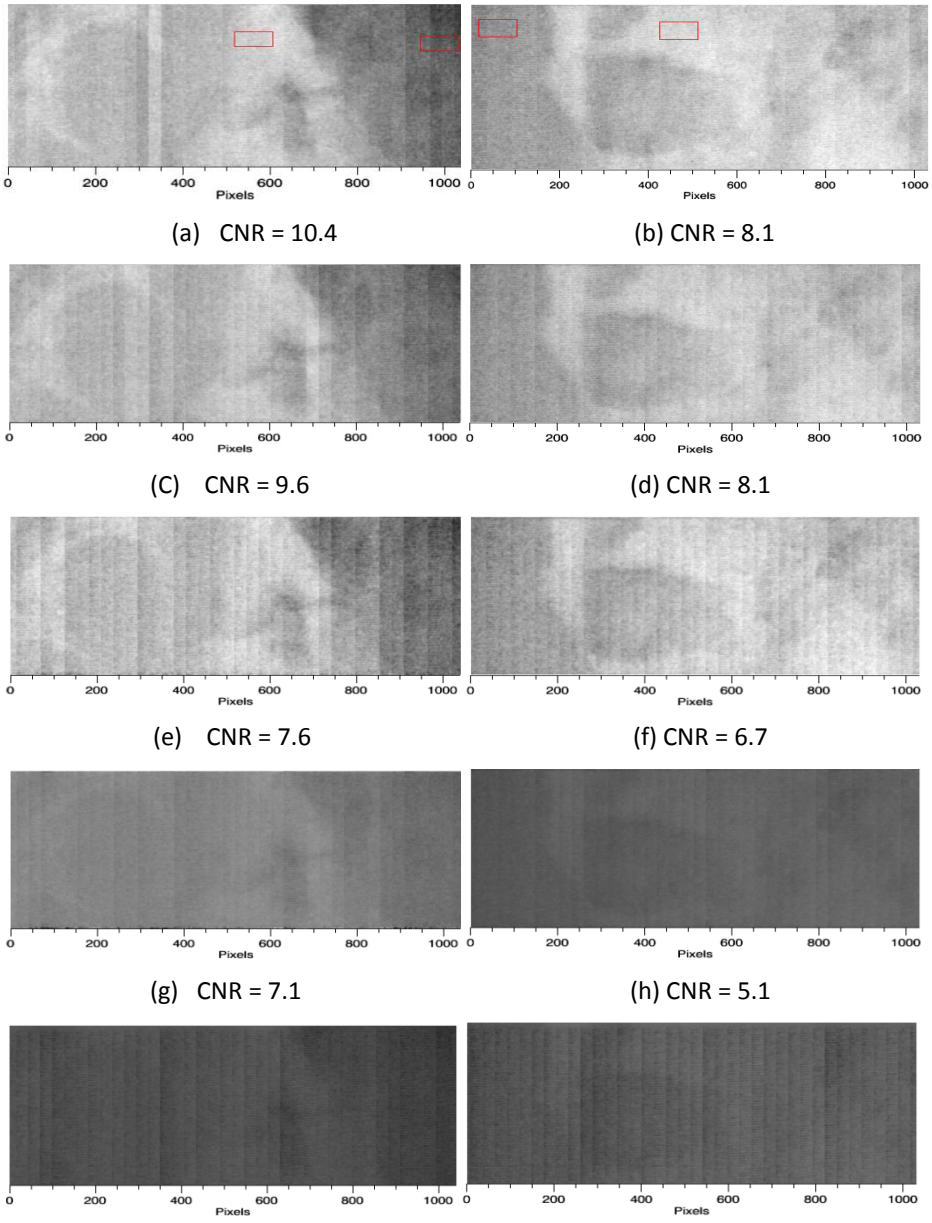

(a) CNR = 10.4 (b) CNR = 8.1

(C) CNR = 9.6 (d) CNR = 8.1

(e) CNR = 7.6 (f) CNR = 6.7

(g) CNR = 7.1 (h) CNR = 5.1

(i) CNR = 4.0 (j) CNR = 3.4

Figure 3.13 ROIs obtained from Sample 1 section 3 are illustrated in the left hand column, and ROIs obtained from Sample 1 section 4 are illustrated in the right hand column. All ROIs contain healthy and suspicious tissue types. Images a, b, c, d, e and f, g, h, i, j correspond to incident exposures of 24.8, 19.0, 13.3, 8.2 and 3.7µCkg^{-1} respectively.

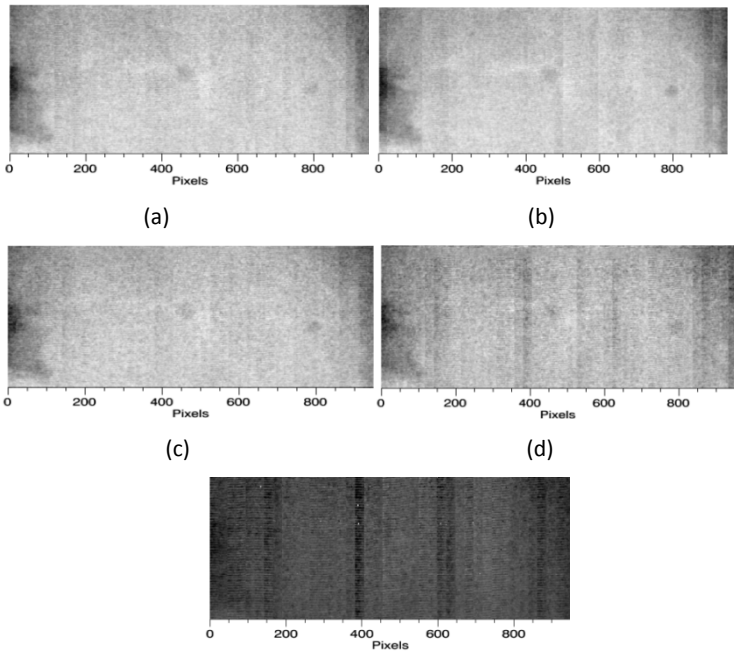

(a) (b)

(c) (d)

(e)

Figure 3.14 Sample 1 section 5 containing healthy tissue only. Images a, b, c, d and e corresponds to incident exposures of 24.8, 19.0, 13.3, 8.2 and 3.7µCkg^{-1} respectively.

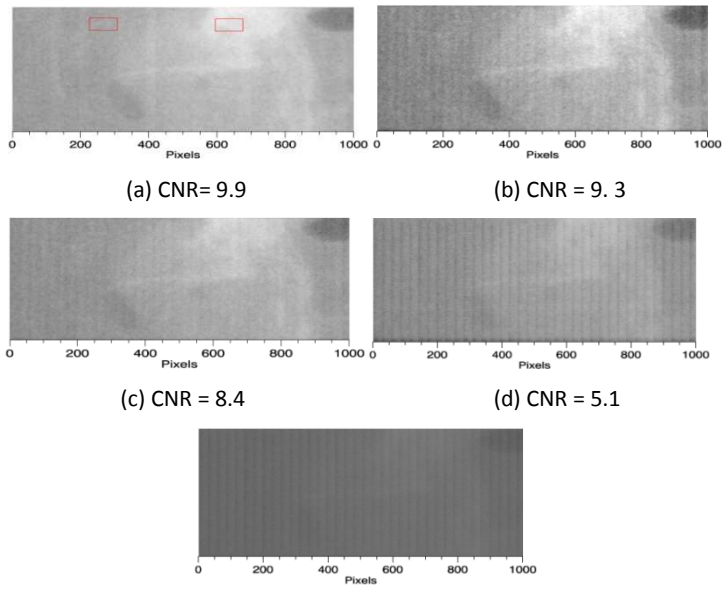

(a) CNR= 9.9 (b) CNR = 9. 3

(c) CNR = 8.4 (d) CNR = 5.1

(e) CNR = 4.1

Figure 3.15 Sample 2 section 1 containing healthy and suspicious tissue. Images a, b, c, d and e corresponds to incident exposures of 24.8, 19.0, 13.3, 8.2 and 3.7µCkg^{-1} respectively.

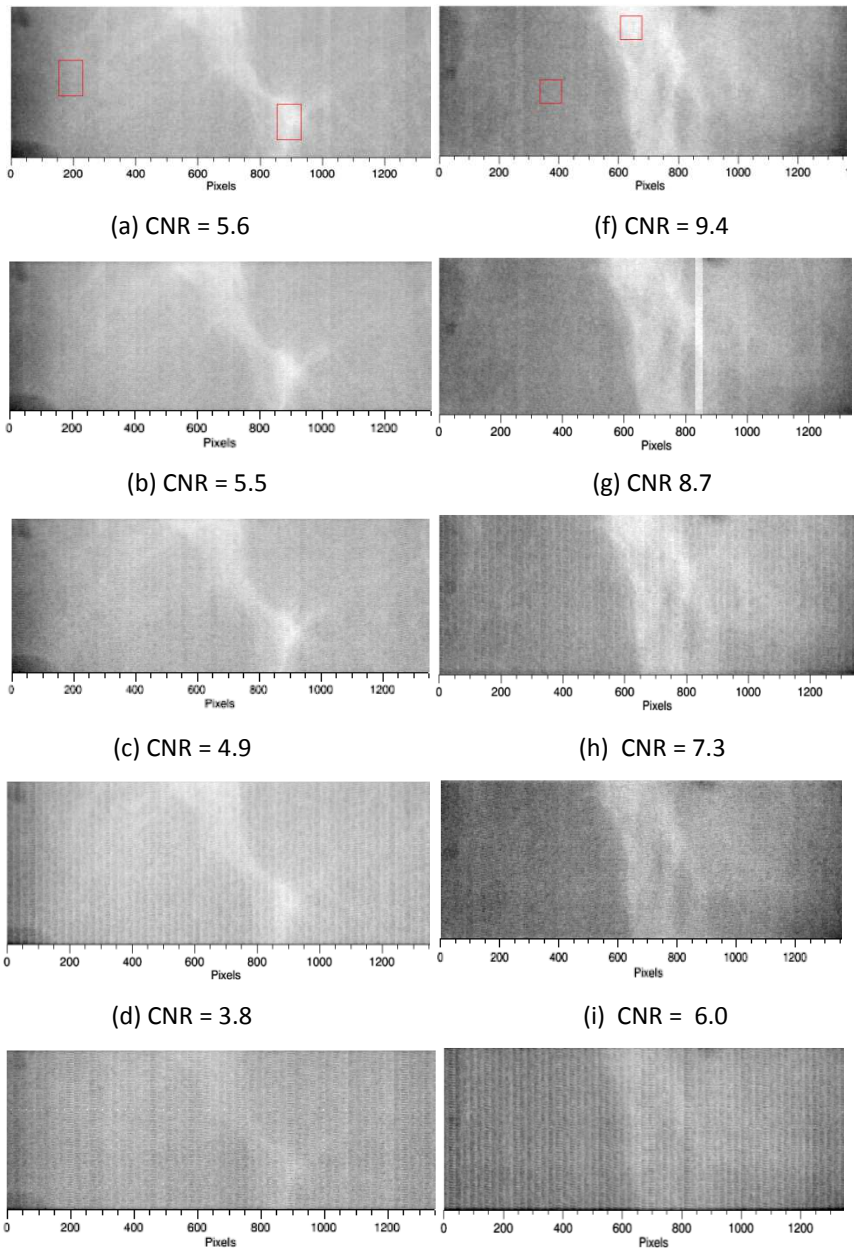

(a) CNR = 5.6 (f) CNR = 9.4

(b) CNR = 5.5 (g) CNR 8.7

(c) CNR = 4.9 (h) CNR = 7.3

(d) CNR = 3.8 (i) CNR = 6.0

(e) CNR = 1.7 (j) CNR = 3.2

Figure 3.16 ROIs obtained from Sample 2 section 2 are illustrated in the left hand column, and ROIs obtained from Sample 2 section 3 are illustrated in the right hand column. All ROIs contain healthy and suspicious tissue types. Images a, b, c, d, e and f, g, h, i, j correspond to incident exposures of 24.8, 19.0, 13.3, 8.2 and 3.7µCkg^{-1} respectively.

Presented in figures 3.17 - 3.21 are the results of the combined feature function i.e. intelligent algorithm. The graphs illustrate the regions of tissue flagged as suspicious for each of the forty image segments investigated (figures 3.12 - 3.16), where suspicious regions correspond to a value of one. Regions that have not exceeded the threshold do not satisfying the condition therefore consequently correspond to zero. These flagged regions correspond to sections within the image which are to be imaged with optimised imaging parameters.

The results obtained from sample 1 section 1 at each exposure level is shown in figure 3.17a-e and table 3.2. The combined feature function appears to be effective at highlighting the suspicious tissue region within this specific image segment where 100% of the suspicious region is highlighted at 24.8, 19.0 and 13.3μCkg^{-1} respectively. The amount of healthy tissue falsely flagged as suspicious appears to be proportional to the level of exposure incident on the sample; however an anomaly is seen at 19.0μCkg^{-1}. From the table, it is seen that using 19.0μCkg^{-1} as the scout exposure results in approximately 69% of the total image being exposed to an increased level of exposure, therefore resulting in 31% of the image being acquired with a reduced exposure (scout beam alone). This therefore indicates that an exposure level of 19.0μCkg^{-1} would be most suited for use as the scout exposure in this instance as it outperforms 13.3, 8.2 and 3.7μCkg^{-1}. It is observed from figure 3.17d, e and table 3.2 that at incident exposures below 13.3μCkg^{-1}, less than a fifth of the suspicious region is flagged. The image quality measurements depicted in figure 3.12 are as expected where a decline in the CNR is observed with increasing filtration. This is due to the increase in quantum mottle. The combined statistical feature function performs well on this specific section of breast sample one.

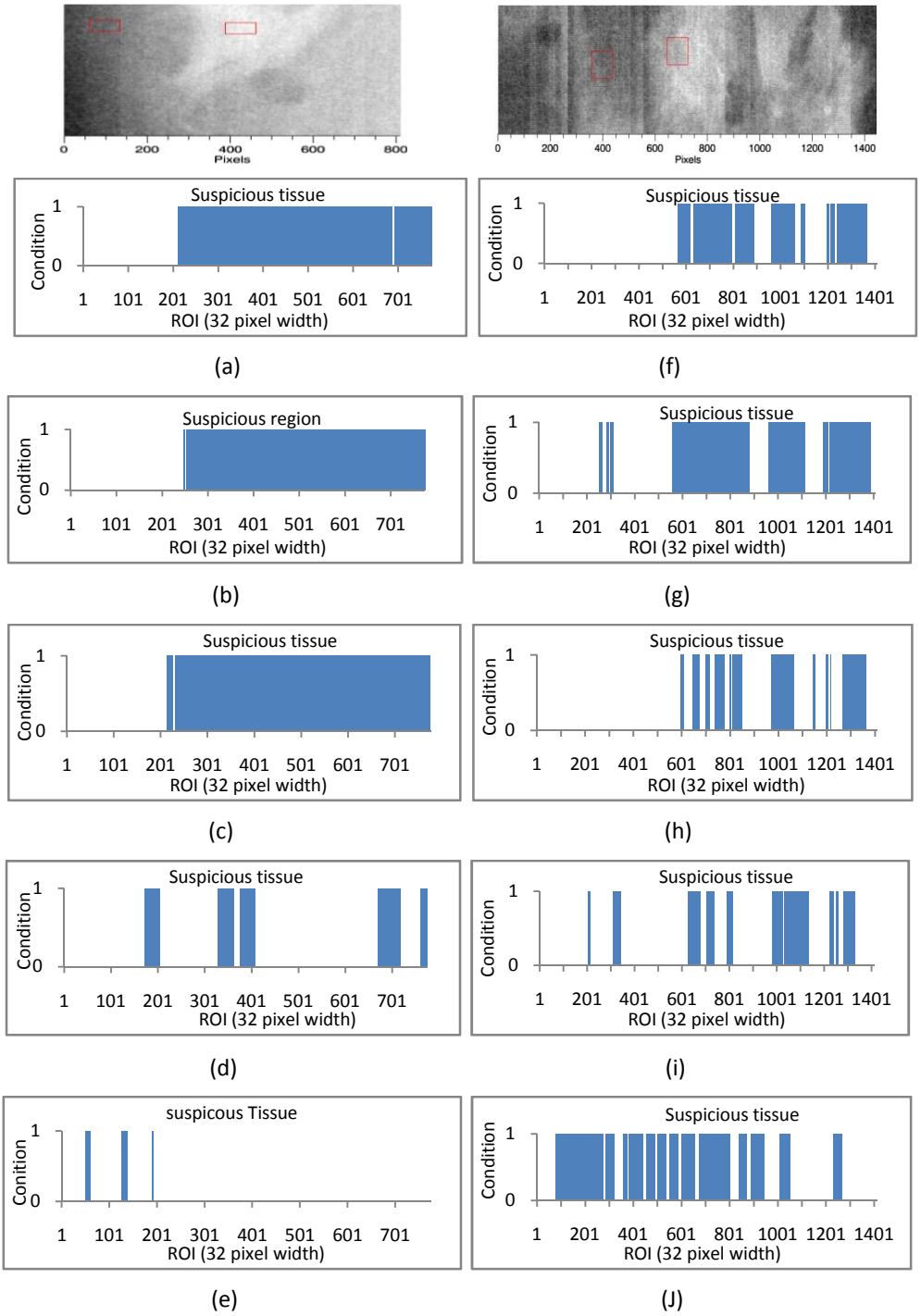

Figure 3.17 Results from the regions of tissue analysed by the combined feature function pertaining to sample 1 section 1 (left column) and sample 1 section 2 (right column). Images a, b, c, d, e and f, g, h, i, j correspond to incident exposures of 24.8, 19.0, 13.3, 8.2 and 3.7μCkg^{-1} respectively.

Table 3.2 Results obtained from Sample 1 section 1 analysis illustrating proportion of tissue highlighted as suspicious for a given level of exposure.

Incident Exposure (μCkg^{-1})	Abnormal region flagged as suspicious (%)	Healthy region flagged as suspicious (%)	Proportion of imaged flagged as suspicious (%)
24.8	100	46.3	73.6
19.0	100	40.8	69.0
13.3	100	44.5	72.7
8.2	16.5	31.8	24.0
3.7	0.0	7.0	3.4

Table 3.3 Results obtained from Sample 1 section 2 analysis illustrating proportion of tissue highlighted as suspicious for a given level of exposure.

Incident Exposure (μCkg^{-1})	Abnormal region flagged as suspicious (%)	Healthy region flagged as suspicious (%)	Proportion of imaged flagged as suspicious (%)
24.8	66.4	0.0	41.0
19.0	82.3	11.0	55.1
13.3	39.7	0.0	24.6
8.2	40.6	7.8	28.1
3.7	43.8	70.9	54.1

Figure 3.17f - j and table 3.3 depicted the results obtained from sample 1 section 2. The intelligent algorithm appears to work well in this instance as a maximum of approximately 82% of the suspicious tissue is flagged whilst only 11% of the healthy tissue is falsely highlighting as suspicious. There appears to be no logical trend seen within table 3.3 however, as a minimum of approximately 40% of the suspicious region is flagged regardless of the exposure level, it can be said that the feature functions functionality is challenged but still proves to be beneficial in differentiating tissue types. In this instance, an incident exposure level of 19.0μCkg^{-1} would be most suited for use as the scout exposure consequently reducing the exposure to 45% of the image whilst highlighting the majority of the suspicious tissue region.

Figure 3.18 along with table 3.4 provide indication that an exposure level of 19.0μCkg^{-1} would be the most suited exposure level to be implemented as the

scout exposure in this instance. It can be seen from figure 3.18c (sample 1 section 3) and table 3.4 that a larger proportion of the image is highlighted as suspicious in comparison to any other exposure level. Although 68% of the healthy tissue is unnecessarily flagged as suspicious, 100% of the suspicious region is detected. This only equates to a 7% increase in the amount of suspicious tissue flagged compared to when an exposure of 19.0μCkg^{-1} or 24.8μCkg^{-1} is used. This is accompanied by a 37% increase in the amount of healthy tissue highlighted, therefore an exposure level of 19.0μCkg^{-1} is deemed as most fitting. Table 3.5 corresponding to sample 1 section 4 shows that approximately 98% of the suspicious tissue region may be highlighted when an exposure of 13.3μCkg^{-1} is used. This is accompanied by a 10% proportion of healthy tissue being wrongly flagged as suspicious. As there is minimal difference between the results obtained using exposure levels of 24.8, 19.0 and 13.3μCkg^{-1}, 13.3μCkg^{-1} would be the most appropriate exposure level to assign as the scout exposure in this instance. The ratio of tissue correctly flagged as suspicious in tables 3.2, 3.3, 3.4 and 3.5 for exposure levels corresponding to 19.0μCkg^{-1} and 13.3μCkg^{-1} appear to be significantly high where on average, 88% of the suspicious regions is highlighted.

As this breast sample (breast sample 1) was initially diagnosed as having a severe fibrocystic content by the radiologist, it was therefore anticipated that these specific regions would challenge the combined feature function's functionality. However, from the results presented above, the feature function appears to perform well.

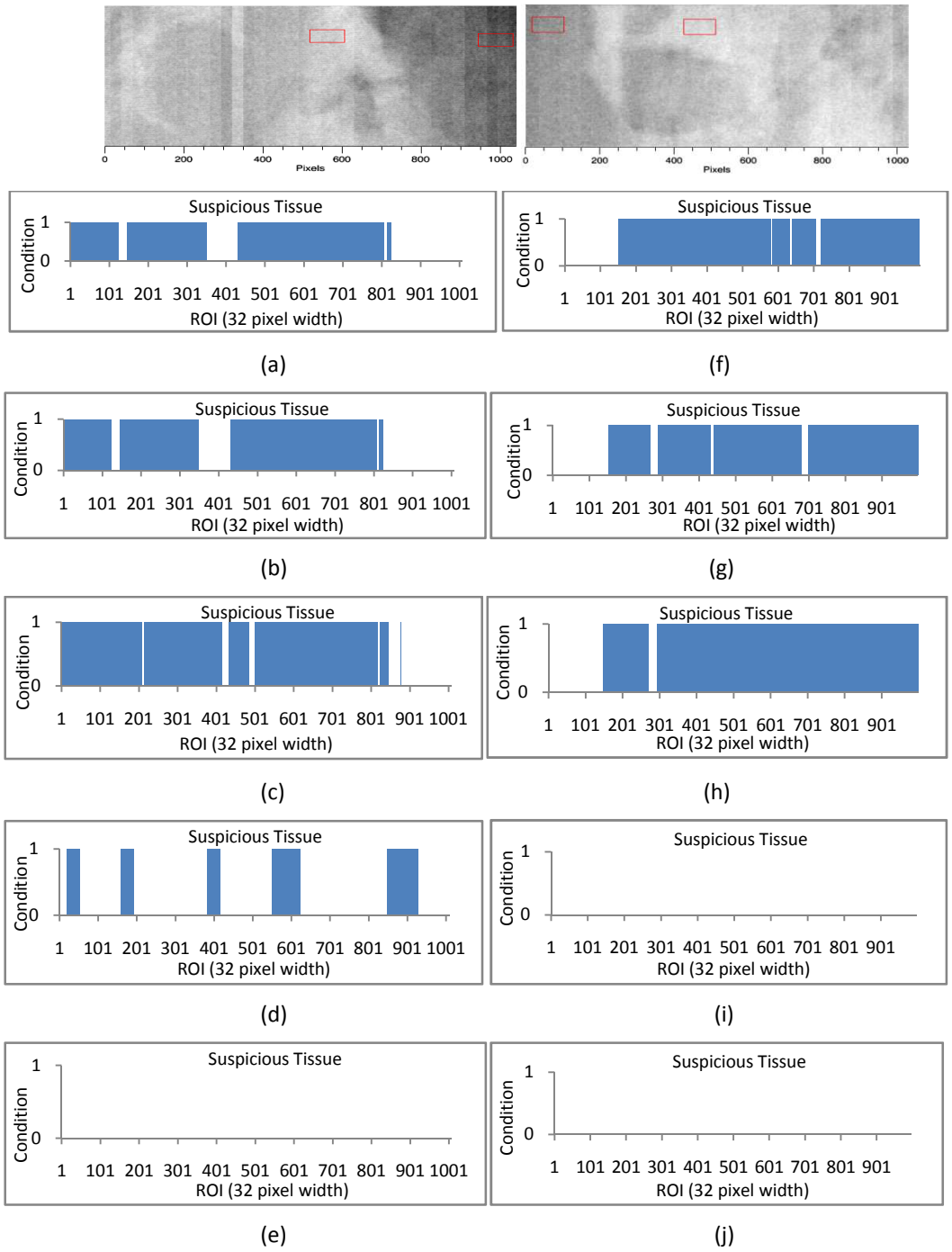

Figure 3.18 Results from the regions of tissue analysed *by the combined feature function pertaining to sample 1 section 3 (left column) and sample 1 section 4 (right column). Images a, b, c, d, e and f, g, h, i, j correspond to incident exposures of 24.8, 19.0, 13.3, 8.2 and 3.7μCkg^{-1} respectively.*

Table 3.4 Results obtained from Sample 1 section 3 analysis illustrating proportion of tissue highlighted as suspicious for a given level of exposure.

Incident Exposure (μCkg^{-1})	Abnormal region flagged as suspicious (%)	Healthy region flagged as suspicious (%)	Proportion of imaged flagged as suspicious (%)
24.8	93.0	43.3	68.6
19.0	93.0	43.3	68.6
13.3	100.0	68.4	84.5
8.2	24.1	25.6	24.9
3.7	0.0	0.0	0.0

Table 3.5 Results obtained from Sample 1 section 4 analysis illustrating proportion of tissue highlighted as suspicious for a given level of exposure.

Incident Exposure (μCkg^{-1})	Abnormal region flagged as suspicious (%)	Healthy region flagged as suspicious (%)	Proportion of imaged flagged as suspicious (%)
24.8	97.1	8.4	82.8
19.0	94.4	6.6	80.3
13.3	97.5	9.6	83.4
8.2	0.0	0.0	0.0
3.7	0.0	0.0	0.0

The final region to be investigated from sample 1 is presented in figure 3.19 and table 3.6. This segment of tissue comprises of healthy tissue only. Considering the images acquired using an incident exposure of 8.2, 13.3, 19.0 and 24.8μCkg^{-1}, the intelligent algorithm performs well as none of the image is highlighted as suspicious. This is due to the fact that the initial region (32 pixel columns) used to determine the threshold value for $SynF_1$ contains both high and low pixel intensities in comparison to the rest of the image, hence resulting in a high range. As $SynF_1$ uses the range as a scaling factor, the threshold for this feature function is set high consequently resulting in none of the image being flagged. From table 3.6 it can be seen that although there are no abnormalities present, approximately 77% of the image is flagged as suspicious when an exposure level of 3.7μCkg^{-1} is used. This is a significant proportion of the image and is due to the performance limitations of both the individual feature functions $SynF_1$ and $SynF_2$ making up the combined feature function. As the mean value used to compute

$SynF_2$ for each ROI was high relative to the maximum pixel value for each of the highlighted columns (due to the pixel rescaling mention in section 3.3.1), the threshold corresponding to $SynF_2$ proved to be too low hence ineffective.

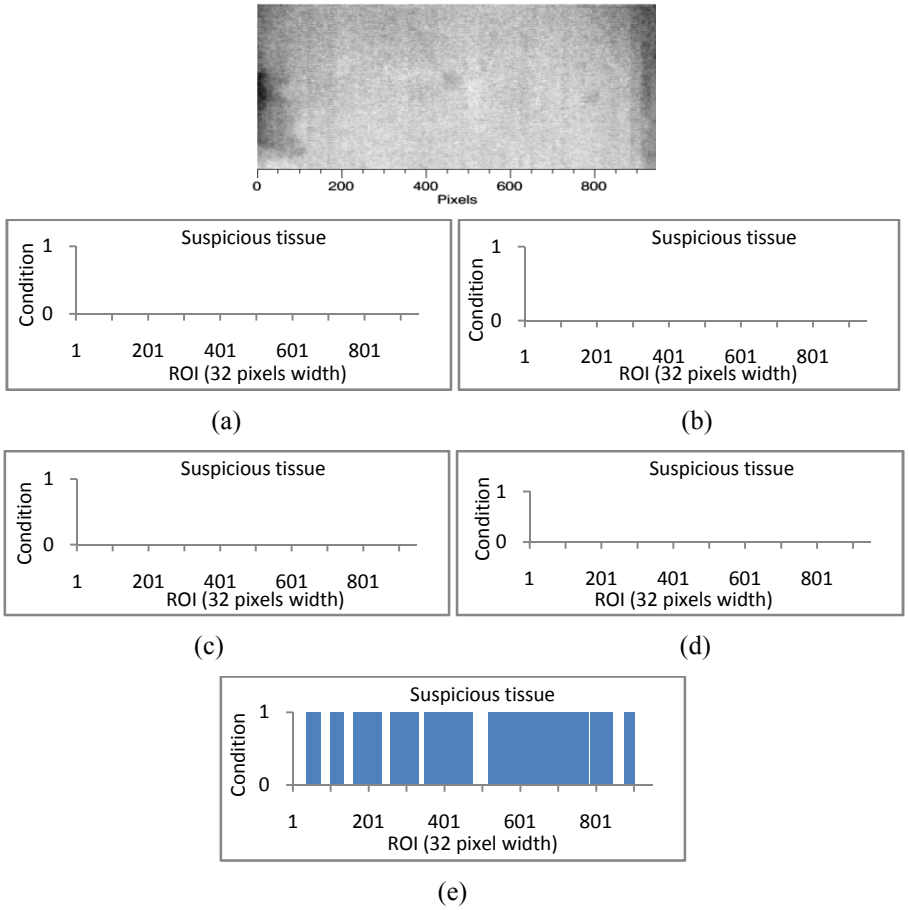

Figure 3.19 Regions of tissue flagged as suspicious by the combined feature function pertaining to Sample 1 section 5. Images a, b, c, d, e corresponds to incident exposures of 24.8, 19.0, 13.3, 8.2 and 3.7μCkg^{-1} respectively.

Table 3.6 Results obtained from Sample 1 section 5 analysis illustrating proportion of tissue highlighted as suspicious for a given level of exposure.

Incident Exposure (μCkg^{-1})	Abnormal region flagged as suspicious (%)	Healthy region flagged as suspicious (%)	Proportion of imaged flagged as suspicious (%)
24.8	0.0	0.0	0.0
19.0	0.0	0.0	0.0
13.3	0.0	0.0	0.0
8.2	0.0	0.0	0.0
3.7	0.0	77.3	77.3

Figure 3.20 and table 3.7 show the results obtained from sample 2 section 1. From the figure it becomes apparent that the proportion of suspicious tissue highlighted decreases with decreasing exposure. This trend appears to continue until none of the suspicious tissue is highlighted. From the table it becomes clear that a reduction in suspicious tissue detection is experienced with each exposure decrement. In this instance, an exposure value of $19.0\mu Ckg^{-1}$ is best suited for use as the scout exposure where 100% of the suspicious tissue region marked as suspicious by the radiologist is flagged. This corresponds with less than a quarter of the healthy tissue being incorrectly highlighted.

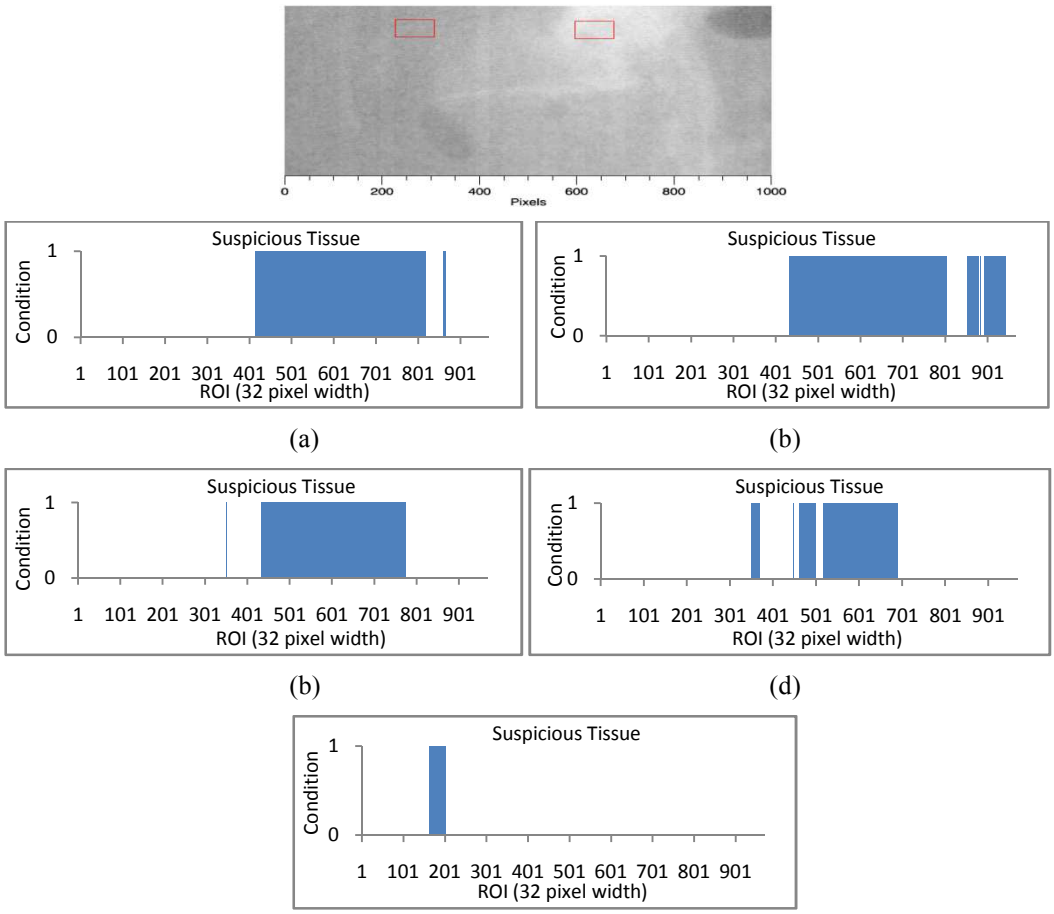

Figure 3.20 Regions of tissue flagged as suspicious by the combined feature function pertaining to Sample 2 section 1. Images a, b, c, d, e corresponds to incident exposures of 24.8, 19.0, 13.3, 8.2 and 3.7μCkg^{-1} respectively.

Table 3.7 Results obtained from Sample 2 section 1 analysis illustrating proportion of tissue highlighted as suspicious for a given level of exposure.

Incident Exposure (μCkg^{-1})	Abnormal region flagged as suspicious (%)	Healthy region flagged as suspicious (%)	Proportion of imaged flagged as suspicious (%)
24.8	100.0	15.7	41.0
19.0	100.0	21.7	45.3
13.3	92.0	9.7	34.4
8.2	57.6	8.0	22.9
3.7	0.0	5.5	3.9

Figure 3.21 depicts the results of the intelligent algorithm obtained from sample 2 sections 2 and 3. From the results presented in table 3.8, it can be seen that as the level of exposure is reduced, both the amount of suspicious tissue flagged along with the proportion of healthy tissue unnecessarily flagged is reduced; however an anomaly is seen at 19.0μCkg^{-1}. 100% and 92% of the suspicious tissue region is highlighted for incident exposure values of 19.0μCkg^{-1} and 13.3μCkg^{-1} respectively. As the proportion of healthy tissue flagged reaches a maximum of approximately 30% and 15% for these two exposures respectively, a maximum of approximately 50% of the total image is highlighted as suspicious. This therefore means the remaining 50% of the sample can be imaged with a reduced exposure. Consequently, this result indicates that a scout exposure of 19.0μCkg^{-1} would be well suited for use as the scout exposure. The CNR declines as expected as seen from figure 3.16.

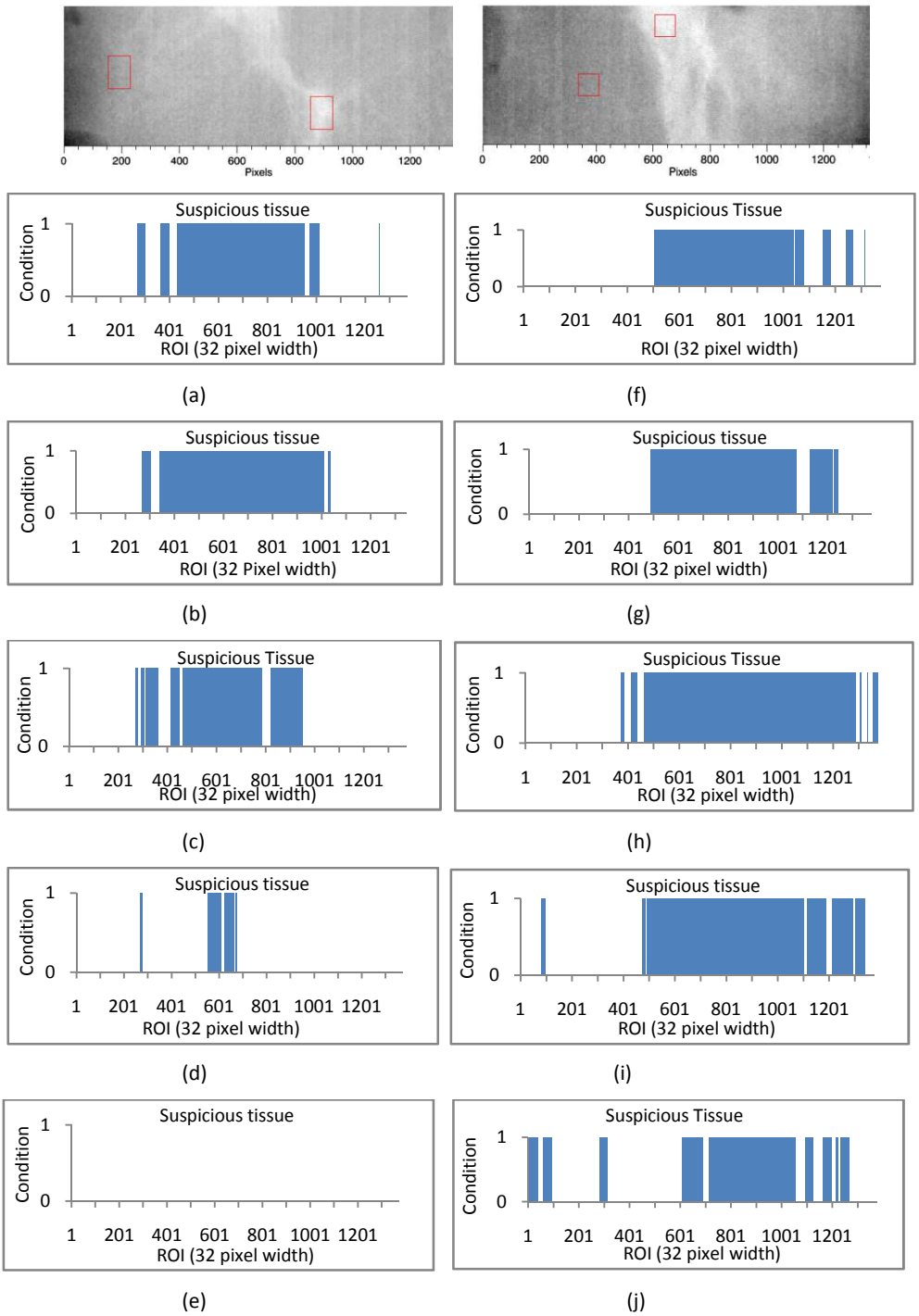

Figure 3.21 Results from the regions of tissue analysed by the combined feature function pertaining sample 2 section 2 (left column) and sample 2 section 3 (right column). Images a, b, c, d, e and f, g, h, i, j correspond to incident exposures of 24.8, 19.0, 13.3, 8.2 and 3.7μCkg^{-1} respectively.

Table 3.8 Results obtained from Sample 2 section 2 analysis illustrating proportion of tissue highlighted as suspicious for a given level of exposure.

Incident Exposure (μCkg^{-1})	Abnormal region flagged as suspicious (%)	Healthy region flagged as suspicious (%)	Proportion of imaged flagged as suspicious (%)
24.8	100.0	18.7	44.7
19.0	100.0	29.2	51.8
13.3	92.2	15.0	39.7
8.2	22.8	1.1	8.1
3.7	0.0	0.0	0.0

Table 3.9 Results obtained from Sample 2 section 3 analysis illustrating proportion of tissue highlighted as suspicious for a given level of exposure.

Incident Exposure (μCkg^{-1})	Abnormal region flagged as suspicious (%)	Healthy region flagged as suspicious (%)	Proportion of imaged flagged as suspicious (%)
24.8	99.3	18.3	44.2
19.0	100.0	24.7	48.8
13.3	100.0	48.4	64.9
8.2	100.0	38.6	58.2
3.7	70.8	32.2	44.6

The results presented in figure 3.21 obtained from sample 2 section 3 show that the suspicious tissue region is easily highlighted by the combined feature function. Table 3.9 above shows that approximately 100% of the suspicious region is flagged when an exposure as low as $8.2\mu Ckg^{-1}$ is used. It is also noticed that the proportion of healthy tissue unnecessarily highlighted increases with a reduction in incident exposure to a point ($13.3\mu Ckg^{-1}$). This therefore indicates that an exposure of $19.0\mu Ckg^{-1}$ would be best suited for use as the scout exposure as it highlights 100% of the suspicious regions whilst reducing the amount of healthy tissue flagged by approximately 50% and 36% in comparison to when $13.3\mu Ckg^{-1}$ and $8.3\mu Ckg^{-1}$ is used respectively.

Similarly to the results obtained from the database image investigation (section 3.3.2), the results presented in this section indicate that the feature function is able to differentiate between healthy and suspicious tissue regions within

mammograms. Regions diagnosed as suspicious by a qualified radiologist were detected in 29 of the 35 low exposure suspicious tissue containing images investigated. It was seen that in 33 instances, less than 50% of the healthy tissue regions were incorrectly flagged as suspicious.

A trend was seen throughout this investigation where the proportion of the suspicious tissue flagged was suddenly decreased between an exposure level of 13.3μCkg^{-1} and 8.2μCkg^{-1}. This occurred in four of the seven sample sections investigated containing suspicious tissue regions (sample 1 sections 1, 3, 4 and sample 2 sections 2). This is believed to be due to the change in spectral shape of the x-ray beam as it is at this point that the attenuation filters go from being comprised of solely PMMA to including 0.6mm of Al.

3.7 Effect of the scanning ROI size used for statistical analysis

The effect the size of the ROI used to step across the scout image analysing pixel values has on abnormality detection has been investigated in an attempt to determine the optimum ROI size to be used in intelligent image production. All of the image sections containing suspicious tissue regions that were previously allocated within samples one and two were investigated using the combined feature function. An incident exposure of 19.0μCkg^{-1} was used as the scout exposure. The ROI used to analyse pixel intensities was stepped across the scout image in one pixel column steps. The results obtained from the combined feature function for this investigation are presented in tables 3.10 – 3.16.

Table 3.10 Performance characteristics of scanning ROI size investigation for sample 1 section 1 using an incident exposure of 19.0μCkg^{-1}.

ROI width (pixel columns)	Abnormal region flagged as suspicious (%)	Healthy region flagged as suspicious (%)	Proportion of imaged flagged as suspicious (%)
16	94.1	28.2	60.4
32	100.0	40.8	69.0
64	100.0	51.7	73.9
128	100.0	83.0	88.0
256	100.0	100.0	100.0

Table 3.11 Performance characteristics of scanning ROI size investigation for sample 1 section 2 using an incident exposure of 19.0μCkg^{-1}.

ROI width (pixel columns)	Abnormal region flagged as suspicious (%)	Healthy region flagged as suspicious (%)	Proportion of imaged flagged as suspicious (%)
16	69.6	3.0	44.2
32	82.3	11.0	55.1
64	92.9	27.2	67.4
128	100.0	55.4	83.0
256	100.0	97.4	99.0

Table 3.12 Performance characteristics of scanning ROI size investigation for sample 1 section 3 using an incident exposure of 19.0μCkg^{-1}.

ROI width (pixel columns)	Abnormal region flagged as suspicious (%)	Healthy region flagged as suspicious (%)	Proportion of imaged flagged as suspicious (%)
16	54.9	30.5	42.9
32	93.0	43.3	68.6
64	100.0	45.0	72.8
128	100.0	66.4	83.5
256	100.0	100.0	100.0

Table 3.13 Performance characteristics of scanning ROI size investigation for sample 1 section 4 using an incident exposure of 19.0μCkg^{-1}.

ROI width (pixel columns)	Abnormal region flagged as suspicious (%)	Healthy region flagged as suspicious (%)	Proportion of imaged flagged as suspicious (%)
16	72.9	0.0	61.2
32	94.4	6.6	80.3
64	100.0	26.6	88.3
128	100.0	65.4	94.3
256	100.0	100.0	100.0

Table 3.14 Performance characteristics of scanning ROI size investigation for sample 2 section 1 using an incident exposure of 19.0μCkg^{-1}.

ROI width (pixel columns)	Abnormal region flagged as suspicious (%)	Healthy region flagged as suspicious (%)	Proportion of imaged flagged as suspicious (%)
16	99.0	13.2	39.0
32	100.0	21.7	45.3
64	100.0	49.2	64.5
128	100.0	48.0	76.3
256	100.0	60.0	90.3

Table 3.15 Performance characteristics of scanning ROI size investigation for sample 2 section 2 using an incident exposure of 19.0μCkg^{-1}.

ROI width (pixel columns)	Abnormal region flagged as suspicious (%)	Healthy region flagged as suspicious (%)	Proportion of imaged flagged as suspicious (%)
16	100.0	20.7	46.1
32	100.0	21.7	45.3
64	100.0	45.0	62.6
128	100.0	64.1	75.6
256	100.0	85.9	90.0

Table 3.16 Performance characteristics of scanning ROI size investigation for sample 2 section 3 using an incident exposure of 19.0μCkg^{-1}.

ROI width (pixel columns)	Abnormal region flagged as suspicious (%)	Healthy region flagged as suspicious (%)	Proportion of imaged flagged as suspicious (%)
16	97.7	18.4	43.8
32	100.0	24.7	48.8
64	100.0	39.9	59.2
128	100.0	64.8	76.1
256	100.0	80.4	86.7

It can be seen from tables 3.10 – 3.16 that a general trend emerges where it is seen that the amount of tissue highlighted as suspicious is proportional to the size of the scanning ROI. It is observed that ROI widths of 128 and 256 pixel columns enables 100% of the suspicious tissue region to be highlighted, however, consequently a minimum of approximately 50% of healthy tissue regions are also unnecessarily flagged. This increases considerably for a scanning

ROI of 256 where at least 80% of the healthy tissue regions are incorrectly highlighted as suspicious tissue.

An ROI of either 32 or 64 pixel columns results in at least 82% of the suspicious tissue regions being correctly highlighted. From tables 3.11 and 3.13, it is shown that a 32 pixel column ROI only incorrectly flags 11% and 6% of the surrounding healthy tissue regions respectively. This increases to approximately just over a fifth of the healthy regions in tables 3.14, 3.15 and 3.16. Tables 3.10 and 3.12 are the only two instances where the proportion of healthy tissue highlighted reaches maximums of approximately 41% and 43% respectively. An ROI width of 64 pixel columns unnecessarily highlights between approximately 27% and 52% of the healthy tissue regions.

It can also be seen from the results that an ROI size of 16 pixel columns highlights a minimum of approximately 55% of the suspicious tissue regions within the samples. This is lower than that of the 32 pixel column wide ROI, however, a lower proportion of the healthy tissue present within the sample was flagged as suspicious. It therefore becomes apparent that a trade off is required between the amount of suspicious tissue detected and the amount of healthy tissue unnecessarily highlighted as suspicious. As a 32 pixel column wide ROI is able to highlight a minimum of 82% of the suspicious tissue regions, whilst allowing up to a 55% reduction in the proportion of healthy tissue flagged as suspicious, it will be used for the remainder of the investigation within subsequent sections of this chapter.

3.8 Feature function threshold optimisation

3.8.1 $SynF_1$ threshold optimisation

As the threshold value governing $SynF_1$ is derived from a region of interest of fixed size taken from an immediate region within the breast, which is assumed to comprise of healthy tissue only, the effects of the size of this 'reference point' used on suspicious tissue detection has been investigated. So far, the size of this region (1mm × 15mm) has remained constant throughout the investigation having a similar size to that of the active area of a single I-ImaS sensor. This section explores the effects of changing the size of this ROI (its width only) where seven different sizes are considered. The size of the scanning ROI used (32 pixel columns) remained constant throughout this investigation along with the scout exposure (19.0µCkg^{-1}). The results are presented in tables 3.17 – 3.20 which correspond to four tissue segments (sample 1 sections 1 and 3 and sample 2 sections 1 and 2) randomly chosen for analysis.

Table 3.17 Results obtained from sample 1 section 1 depicting effect of threshold ROI size analysis for $SynF_1$ using an incident exposure of 19.0µCkg^{-1}.

ROI width (mm)	Abnormal region flagged as suspicious (%)	Healthy region flagged as suspicious (%)	Proportion of imaged flagged as suspicious (%)
1	100.0	40.8	69.0
2	100.0	40.8	69.0
3	87.1	19.0	45.0
4	75.4	0.0	38.2
5	5.8	0.0	2.9
6	0.0	0.0	0.0
7	0.0	0.0	0.0

Table 3.18 Results obtained from sample 1 section 3 depicting effect of threshold ROI size analysis for $SynF_1$ using an incident exposure of 19.0μCkg^{-1}.

ROI width (mm)	Abnormal region flagged as suspicious (%)	Healthy region flagged as suspicious (%)	Proportion of imaged flagged as suspicious (%)
1	93.0	43.3	68.6
2	16.4	0.0	8.3
3	0.0	0.0	0.0
4	0.0	0.0	0.0
5	0.0	0.0	0.0
6	0.0	0.0	0.0
7	0.0	0.0	0.0

Table 3.19 Results obtained from sample 2 section 1 depicting effect of threshold ROI size analysis for $SynF_1$ using an incident exposure of 19.0μCkg^{-1}.

ROI width (mm)	Abnormal region flagged as suspicious (%)	Healthy region flagged as suspicious (%)	Proportion of imaged flagged as suspicious (%)
1	100.0	21.7	45.3
2	100.0	21.0	44.7
3	81.0	9.4	31.0
4	81.0	9.4	31.0
5	81.0	9.4	31.0
6	81.0	9.4	31.0
7	81.0	9.4	31.0

Table 3.20 Results obtained from sample 2 section 2 depicting effect of threshold ROI size analysis for $SynF_1$ using an incident exposure of 19.0μCkg^{-1}.

ROI width (mm)	Abnormal region flagged as suspicious (%)	Healthy region flagged as suspicious (%)	Proportion of imaged flagged as suspicious (%)
1	100.0	29.2	51.8
2	63.3	0.0	20.2
3	41.7	0.0	13.3
4	5.7	0.0	1.8
5	0.0	0.0	0.0
6	0.0	0.0	0.0
7	0.0	0.0	0.0

It can be seen from the four tables above that the smaller the ROI used to derive the threshold corresponding to $SynF_1$, the higher the proportion of suspicious tissue highlighted. An ROI of 1mm enables over 90% of the suspicious tissue

region to be correctly flagged whilst only highlighting a maximum of approximately 44% (table 3.18) of the surrounding healthy tissue. This consequently results in approximately a minimum of 56% of the healthy tissue regions being exposed to a reduced incident exposure.

Tables 3.17 and 3.20 show gradual decreases in the proportion of suspicious tissue highlighted corresponding to increases in ROI size. This is due to the fact that the initial 7mm used to obtain this threshold value from the images gets progressively more intense. This consequently resulting in the threshold being set too high, rendering it ineffective past a given point (5mm and 6mm respectively). Tables 3.18 and 3.19 together illustrate the robustness of the feature functions ability to function in opposite extreme conditions. The threshold value pertaining to table 3.18 (sample 1 section 3) was taken from the end of this image segment as it corresponded to the edge of the sample replicating the region directly below the skin (as indicated by the smaller rectangle in figure 2.9a). From this table it can be seen that the ability to highlight any suspicious tissue stops at 2mm, beyond this point, the immediate tissue intensity increases corresponding to the suspicious tissue region. This therefore renders the ROI ineffective. Table 3.19 show that it is possible for the suspicious tissue region to be detected using larger ROI's than was previously seen. This corresponds well with the fact that the tissue sample used to obtain these results (sample 2 section 1) consists of smooth adipose tissue where there is minimal pixel intensity change within the initial 7mm. As a result, this enables the continual functioning of the feature function.

From the tables, a trend was observed where derivation of the threshold value from a region larger than 2mm had a negative effect on the proportion of suspicious tissue flagged. This reduction is believed to be due to the fact that as

the ROI increases, it will eventually begin to include the suspicious tissue regions, hence higher pixel values consequently resulting in the threshold value being set too high. As a result, the threshold becomes ineffective. A 1mm ROI is therefore used in subsequent investigations

3.8.2 $SynF_2$ threshold optimisation

The magnitude of the threshold value governing the ability of $SynF_2$ to highlight suspicious tissue regions was also investigated. The initial value assigned as the threshold throughout this investigation thus far was determined experimentally; this value corresponded to 250a.u (arbitrary units). In an attempt to optimise this value, the effect of both increasing and decreasing it by 20% was investigated. All seven samples were used, the scout exposure remained constant at 19.0µCkg^{-1} along with the size of the scanning ROI (32 pixel columns wide) and the width of the ROI (1mm) governing $SynF_1$. The results obtained are presented below (tables 3.21 – 3.27).

Table 3.21 Results obtained from sample 1 section 1 depicting effect of $SynF_2$ threshold analysis using an incident exposure of 19.0µCkg^{-1}.

Threshold Value (DN)	Abnormal region flagged as suspicious (%)	Healthy region flagged as suspicious (%)	Proportion of imaged flagged as suspicious (%)
200	100.0	76.4	85.0
250	100.0	40.8	69.0
300	30.4	0.0	15.4

Table 3.22 Results obtained from sample 1 section 2 depicting effect of $SynF_2$ threshold analysis using an incident exposure of 19.0μCkg^{-1}.

Threshold Value (DN)	Abnormal region flagged as suspicious (%)	Healthy region flagged as suspicious (%)	Proportion of imaged flagged as suspicious (%)
200	82.3	11.0	55.1
250	82.3	11.0	55.1
300	62.8	9.0	42.3

Table 3.23 Results obtained from sample 1 section 3 depicting effect of $SynF_2$ threshold analysis using an incident exposure of 19.0μCkg^{-1}.

Threshold Value (DN)	Abnormal region flagged as suspicious (%)	Healthy region flagged as suspicious (%)	Proportion of imaged flagged as suspicious (%)
200	93.0	44.7	69.3
250	100.0	21.7	45.3
300	5.2	6.2	5.7

Table 3.24 Results obtained from sample 1 section 4 depicting effect of $SynF_2$ threshold analysis using an incident exposure of 19.0μCkg^{-1}.

Threshold Value (DN)	Abnormal region flagged as suspicious (%)	Healthy region flagged as suspicious (%)	Proportion of imaged flagged as suspicious (%)
200	94.4	6.6	80.3
250	94.4	6.6	80.3
300	2.0	0.0	1.7

Table 3.25 Results obtained from sample 2 section 1 depicting effect of $SynF_2$ threshold analysis using an incident exposure of 19.0μCkg^{-1}.

Threshold Value (DN)	Abnormal region flagged as suspicious (%)	Healthy region flagged as suspicious (%)	Proportion of imaged flagged as suspicious (%)
200	100.0	22.6	52.6
250	100.0	21.7	45.3
300	51.6	0.0	15.5

Table 3.26 Results obtained from sample 2 section 2 depicting effect of $SynF_2$ threshold analysis using an incident exposure of 19.0μCkg^{-1}.

Threshold Value (DN)	Abnormal region flagged as suspicious (%)	Healthy region flagged as suspicious (%)	Proportion of imaged flagged as suspicious (%)
200	100.0	42.8	61.1
250	100.0	21.7	45.3
300	25.3	0.0	8.1

Table 3.27 Results obtained from sample 2 section 3 depicting effect of $SynF_2$ threshold analysis using an incident exposure of 19.0μCkg^{-1}.

Threshold Value (DN)	Abnormal region flagged as suspicious (%)	Healthy region flagged as suspicious (%)	Proportion of imaged flagged as suspicious (%)
200	100.0	14.2	41.6
250	100.0	24.7	48.8
300	60.8	0.0	19.4

It can be seen from the results directly above that a threshold value of either 200Arb.U or 250Arb.U is preferable over 300Arb.U. This is due to the fact that only a maximum of approximately 63% of the suspicious tissue is highlight (table 3.22) compared to as much as 100% by 200Arb.U and 250Arb.U (tables 3.21, 3.25, 3.26 and 3.27). The feature functions performance for both 200Arb.U and 250Arb.U are similar throughout this investigation, however, as the proportion of healthy tissue flagged as suspicious is generally lower for 250Arb.U than for 200Arb.U, it becomes apparent that 250Arb.U is the more appropriate value to be used in the final algorithm.

3.9 Summary

From the results presented above, it can be concluded that the ability to highlight suspicious tissue regions by extracting information using simple statistical feature functions from a low exposure mammogram is possible

(section 3.5). As a result of combining the results obtained from the MIAS database investigation (section 3.3.2) with the results obtained from the transmission image investigation above, an optimum set of intelligent imaging parameters have become apparent. These parameters have been seen (sections 3.5 – 3.7) to increase detection of suspicious tissue regions within the breast tissue samples whilst also enabling differentiation between tissue regions comprising solely of healthy tissue and those containing suspicious tissue.

It becomes apparent that allocating a specific level of exposure to the scout scan results in a trade off between the percentage of the suspicious tissue highlighted and the proportion of healthy tissue unnecessarily subjected to an increased incident exposure. A scout incident exposure level of 19.0μCkg^{-1} appeared to sufficiently flag the suspicious regions within the images whilst reducing the total exposure incident on the breast in comparison to the conventional unfiltered image (24.8μCkg^{-1}).

3.10 EDXRD Introduction

The concept of using an EDXRD image as a means of identifying suspicious tissue regions from within a breast sample and using it to optimise the imaging parameter settings used to obtain a mammogram is explored below. The effect changing an individual parameter setting has on suspicious tissue detectability is investigated. The effect of changing the system optics, statistical quality of the data, threshold value used to differentiate between suspicious and healthy tissue regions and the size of the stepping ROI used to analyse each pixel column was investigated. This consequently provided indication as to the optimum parameters to be used within an intelligent system.

3.11 Methodology

3.11.1 Diffraction profiles

Depicted in figure 3.22 is an example of the raw spectra obtained from tissue sample one from a region containing both healthy and suspicious tissue types. It can be seen that adipose tissue has a narrower, taller peak than that of the superimposed suspicious tissue region which appears broader and shorter with a less distinct peak. As concluded by Ryan and Farquharson (2007), this phenomenon is due to the decreased structural order of the collagen fibrils seen with cancer invasion consequently resulting in a disturbance in the atomic structure of the diseased tissue. This consequently leads to less periodic scattering hence lower detected counts for a given spectral window. The diffraction profile corresponding to the diseased tissue region does not peak at $1.5nm^{-1}$ - $1.6nm^{-1}$ as previous authors' have reported (Castro et al (2004), Castro et al (2005) and Royle et al (1999)), however this is thought to be due to the presence of more than one tissue component contributing to the scattered signature. Kidane et al (1999) reported similar findings where it was also demonstrated that the scattered signature for diseased tissue was dependent on the proportion of the tissue components present. 40% of the carcinoma containing tissue regions investigated by Kidane et al (1999) peaked at an average momentum transfer value of $1.14nm^{-1}$ where the diseased tissue component made up a maximum of 25% of the tissues present. The characteristic peak of $1.6nm^{-1}$ was seen for ROI's containing at least a 65% malignant tissue component. This indicates that the diffraction profile is heavily dependent on the tissue type ratio present in the scatter volume. As figure 3.22 fails to illustrate a distinct peak at $1.6nm^{-1}$, it can be concluded that the suspicious regions in sample one also contained superimposed healthy tissue

therefore unlike the carcinoma peak usually seen at momentum transfer values of 1.5nm^{-1} - 1.6nm^{-1}, a broad plateau is seen instead.

Clinically, as sample thicknesses of approximately 5cm (compressed breast) will be encountered, a change in the type of optics used to obtain the diffraction signal is required along with the need for an array of x-ray scatter detectors. The use of a multi-slit collimator would enable multiple scatter volumes to be investigated simultaneously along the path of the x-ray beam through the sample. The affect of beam hardening would increase as attenuation effects are encountered before and after the scatter volume consequently altering the diffraction profile. At mammographic energies on a Mo/Mo anode filter combination, EDXRD would not be possible due to the mono-energetic nature of the x-ray beam hence would be restricted to use on the thicker breasts imaged with a W anode.

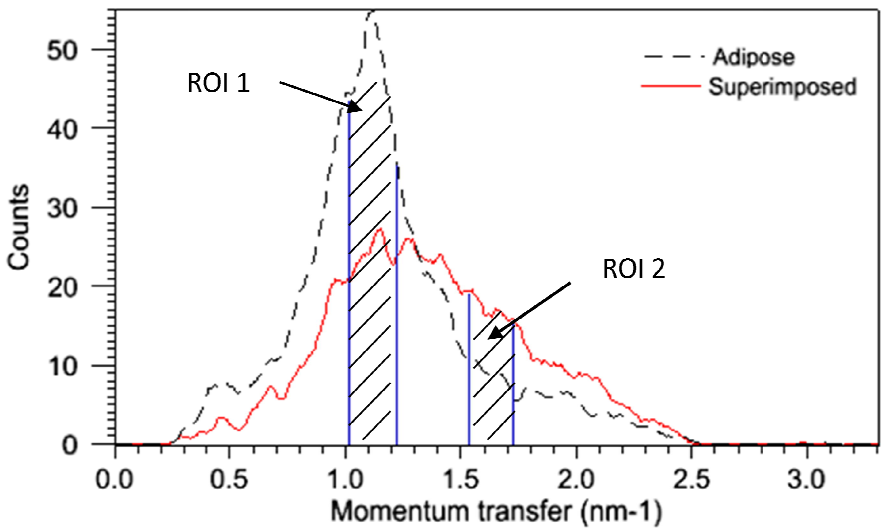

Figure 3.22 Diffraction profile obtained from suspicious tissue region within sample one demonstrating the effect of tissue superimposition within the scattering volume. ROI's obtained with momentum transfer windows 1.02nm^{-1} – 1.2nm^{-1} and 1.52nm^{-1} – 1.71nm^{-1} depicted.

The shift in momentum transfer displayed by the diseased region in figure 3.22 may also be due to the nature of the formalin fixation used to preserve the specimen. Cook (2008) investigated the effects of such preservation techniques using pork muscle as a breast equivalent material. It was concluded that the concentration of the formalin might affect the diseased diffraction profile most significantly where a shift in momentum transfer was seen from 1.5nm^{-1} to 1.2nm^{-1} corresponding well with figure 3.22. It was also demonstrated that the momentum transfer value for adipose tissue was unaffected regardless of the formalin concentration used therefore its characteristic peak remained unchanged corresponding to a momentum transfer value of 1.1nm^{-1}.

3.11.2 EDXRD imaging

EDXRD images corresponding to three suspicious tissue regions (referred to as samples 1, 2a and 2b) within the two breast samples were acquired using three different optical setups (corresponding to solid angles of 0.23, 0.43 and 0.98msr). This consequently allowed the effects of momentum transfer resolution to be investigated. Each tissue region was imaged using all three setups and all at a range of exposure levels. The diffraction profiles of each ROI making up the diffraction images was obtained using a laboratory based EDXRD system as described in chapter 2 section 2.4.

The samples were individually mounted on a translation stage (Newport, M-IMS600CC and M-IMS300V) connected via a controller (Newport) to a PC. This enabled the samples to be scanned in a raster like fashion where appropriate increments both vertically and horizontally were made (governed by the solid angle in use). Automated scanning of the tissue samples was achieved using the input/output facilities on the MCA and controller. The motors were controlled by

LabView software (National Instruments, USA), in which the 2D scan start point, end point and step size could all be set. Depending on the optics in use, the x-ray tube was operated in fluoroscopy mode at either a potential of 60kVp and 5mA, 60kVp and 1mA or 60kVp and 0.5mA (corresponding to 0.23, 0.43 and 0.98msr respectively) as to ensure a detector dead time below 10%.

Having obtained the diffraction profiles of the tissue samples, background corrections were made using data obtained from a sample free setup. The background signal was subtracted from each of the measured spectra therefore allowing the removal of any unwanted scatter contributions from surrounding materials. Diffraction images were constructed by summing the counts in a momentum transfer window and then allocating that point in the image an appropriate grey level value between 0 and 255. This therefore meant that all of the EDXRD images regardless of imaging parameter setting, was normalised to 8 bits. Momentum transfer windows that maximised the contrast between the suspicious and healthy tissue regions were selected for analysis. Figure 3.22 depicts the windows used where the region from $1.02nm^{-1}$ - $1.21nm^{-1}$ and $1.52nm^{-1}$ - $1.71nm^{-1}$ is shown corresponding to thirty MCA channels. Cook (2008) investigated the effect of window channel size on EDXRD image contrast between healthy and diseased tissue regions, and found there to be less than a 8% difference between a 1.53keV (10 channels) and a 15.34keV (100 channels) energy window. It was observed that this difference was due to the location of the window centre which is affected by the window width. The wider the window, the lower the contrast, however, this contrast decrease was compensated by an increase in count rate. The chosen window widths in this investigation corresponded to an energy window of 4.6keV.

Ratio images where obtained by normalising the suspicious tissue region intensities with the healthy regions in order to have comparable images. Suspicious tissue regions were displayed with a higher pixel intensity (appearing whiter) than the adipose tissue which appeared darker within the EDXRD images as shown in figure 3.23 below. The grey area surrounding the suspicious (white) tissue represents glandular tissue which appears to have a similar scatter intensity to the suspicious tissue in comparison to the adipose tissue.

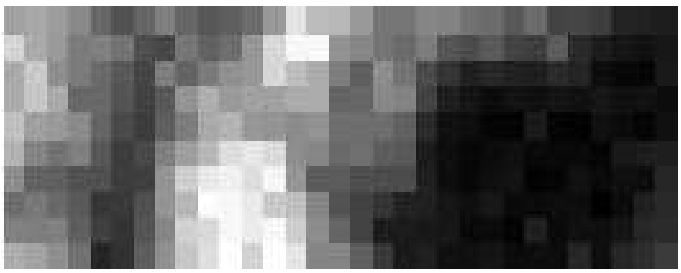

Figure 3.23 EDXRD image of an ROI located within breast sample one obtained using a solid angle of 0.23msr. Suspicious tissue regions correspond to a high (white) pixel intensity.

The momentum transfer window corresponding to suspicious tissue was selected using the range of values used previously by several authors including Cook (2008) and Kidane et al (1999). A momentum transfer value with central position of 1.6nm^{-1} was used throughout this investigation

3.11.3 Data analysis procedure

As the information contained within the EDXRD images were presented in the form of grey level pixel values, the mean function was used as a method of extracting feature information. A one column wide stepping ROI was used to step across the image in one pixel column steps averaging all the pixels within a

single column (fig 3.24). As the ROI gave rise to a single value, this value was then used as a means of comparison against a predetermined threshold value (see section 3.3.2) which determined whether the ROI was suspicious. If the ROI was deemed as suspicious, a parameter change would be made attempting to increase image quality.

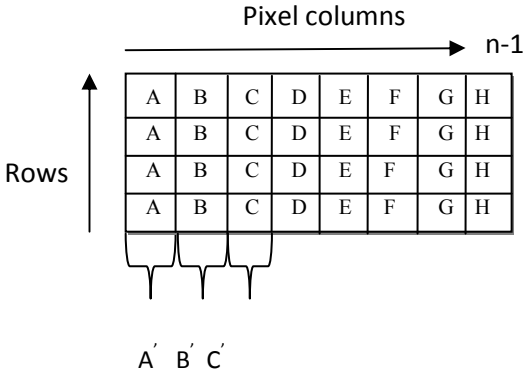

Where A′, B′ and C′ to n′ – 1 represents the average pixel value of each individual column.

Figure 3.24 Schematic of stepping ROI where pixels within a single column are averaged.

3.12 Setup optimisation

3.12.1 Threshold determination

The EDXRD images were used to set the exposure level incident on the sample, where above a given threshold, the exposure would be changed. Three diffraction images of size 31mm × 10mm were obtained from samples one and two using an x-ray beam collimation size of 1mm × 2mm corresponding to a solid angle of 0.23msr (fig 3.25). All tissue regions were chosen as they were known to partially contain healthy and suspicious tissue types. Column averages were used to decide whether or not a suspicious region existed in that column of the image.

All images were byte scaled and a threshold value of 100DN (40% of the dynamic range) was used. This value appeared to be the most appropriate threshold value as it would enable positive identification, consequently parameter optimisation, of a high proportion of the suspicious tissue regions with minimal effect on the surrounding healthy tissue (table 3.28, 3.29 and 3.30). Although a threshold of 50DN (20% of the dynamic range) enabled 100% identification of the suspicious tissue region to be flagged, over 25% of the flagged columns were falsely highlighting surrounding healthy tissue.

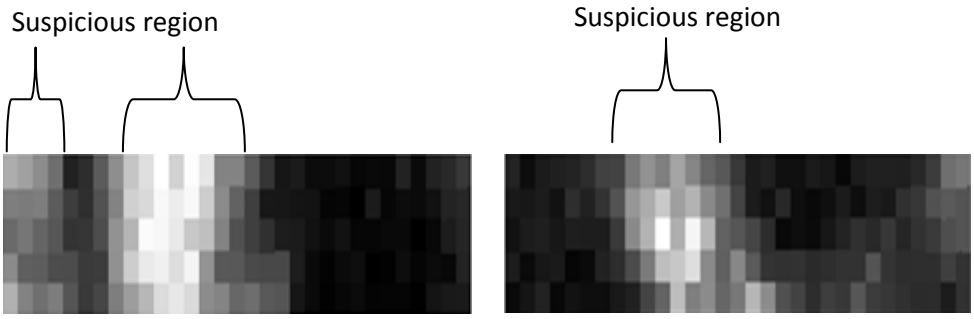

(a) Sample 1 (b) sample 2a

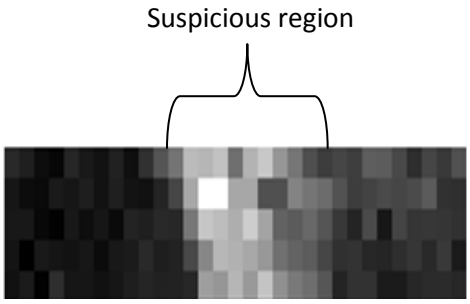

(c) sample 2b

Figure 3.25 EDXRD image of sample 1, 2a and 2b corresponding to a, b and c respectively.

Table 3.28 Effect of threshold settings on breast sample 1 suspicious tissue detection.

Statistical threshold value (DN)	Proportion of image flagged as suspicious (%)	Proportion of suspicious tissue flagged (%)	Flagged columns in suspicious region (%)
50	58.0	100.0	72.2
100	41.9	100.0	100.0
150	19.3	42.8	100.0
200	12.9	28.5	100.0

Table 3.29 Effect of threshold settings on breast sample 2a suspicious tissue detection.

Statistical threshold value (DN)	Proportion of image flagged as suspicious (%)	Proportion of suspicious tissue flagged (%)	Flagged columns in suspicious region (%)
50	48.3	100.0	66.7
100	22.5	70.0	100.0
150	9.6	30.0	100.0
200	0	0	0

Table 3.30 Effect of threshold settings on breast sample 2b suspicious tissue detection.

Statistical threshold value (DN)	Proportion of image flagged as suspicious (%)	Proportion of suspicious tissue flagged (%)	Flagged columns in suspicious region (%)
50	61.2	100.0	57.8
100	29.0	81.8	100.0
150	16.1	45.4	100.0
200	0	0	0

It can be seen from tables 3.28, 3.29 and 3.30 that the choice of the threshold value implemented affects not only the proportion of suspicious tissue highlighted but also the exposure incident on healthy tissue regions. A trend is seen where the efficiency of the exposure deposition with respect to the suspicious tissue regions increases with threshold value (as indicated from the last column). However, this is inversely proportional to the amount of suspicious tissue highlighted. When a threshold value of 100DN is used 100% of the flagged ROI's are located within the desired tissue region where 100.0%, 70.0% and 81.8% of the abnormality is highlighted for samples 1, 2a and 2b respectively.

Although a threshold value of 150DN (60% of the dynamic range) allows detection of 100% of the suspicious tissue regions, the proportion of suspicious tissue actually highlighted is significantly less compared to 100DN for any given image; consequently, a threshold value of 100DN will be used in all proceeding investigations.

3.12.2 Statistical quality of data

The previous section demonstrated the importance the predetermined threshold value assigned to govern the tissue differentiation performance of the mean function had on suspicious tissue detection. This section explores the effect the number of photons detected over the diffraction profile has on suspicious tissue detection. EDXRD images of breast sample one were acquired at four different statistical qualities (fig 3.26) as shown in table 3.31 where a count summation momentum transfer window corresponding to diseased tissue ($1.52nm^{-1}$ - $1.71nm^{1}$) was used.

Table 3.31 Experiment results obtained from sample one depicting the statistical quality of the four images investigated.

Image (fig 3.31)	Count time (Sec)	No. Of photons in profile	Sample incident exposure (μCkg^{-1})
A	8	122900	30.9
B	4	63100	15.4
C	2	31500	7.8
D	1	15200	3.9

The images consisted of thirty one 1mm × 10mm columns as shown in figure 3.26 enabling a 1 pixel column × 5 pixel row ROI to be stepped across the image in one pixel column steps averaging pixel intensities within the ROI. From the figure, it can be seen that the pixel intensity of the suspicious regions decreases relative to the surrounding healthy regions, as the statistical quality of the data

decreases. This is also demonstrated in figure 3.27. It is believed that the number of counts detected may potentially have a significant effect on the detectability of subtle abnormalities.

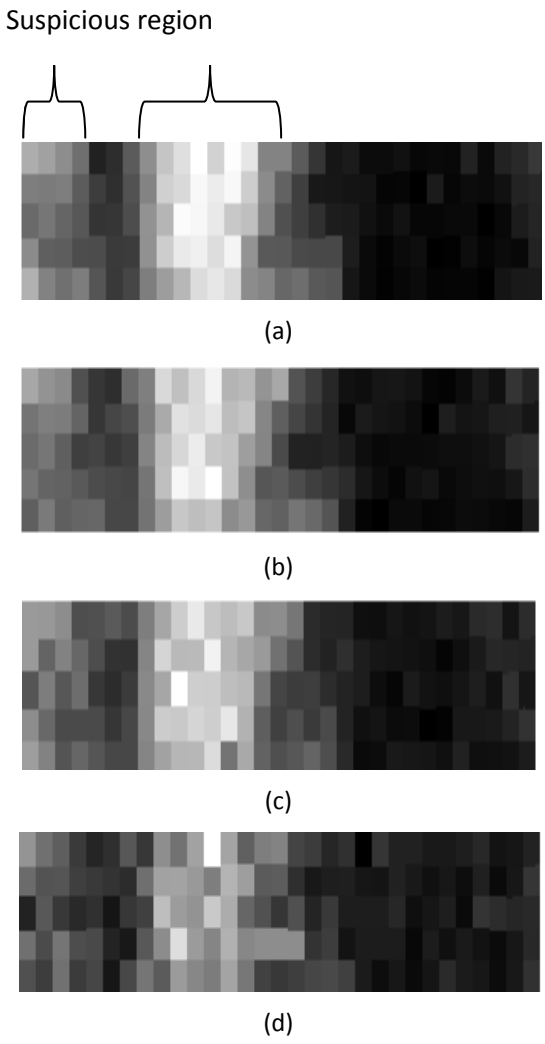

Figure 3.26 Effect the number of photon counts has on visibility of suspicious tissue region in sample one. Images a, b, c and d corresponding to 122900, 63100, 31500 and 15200 photon counts respectively.

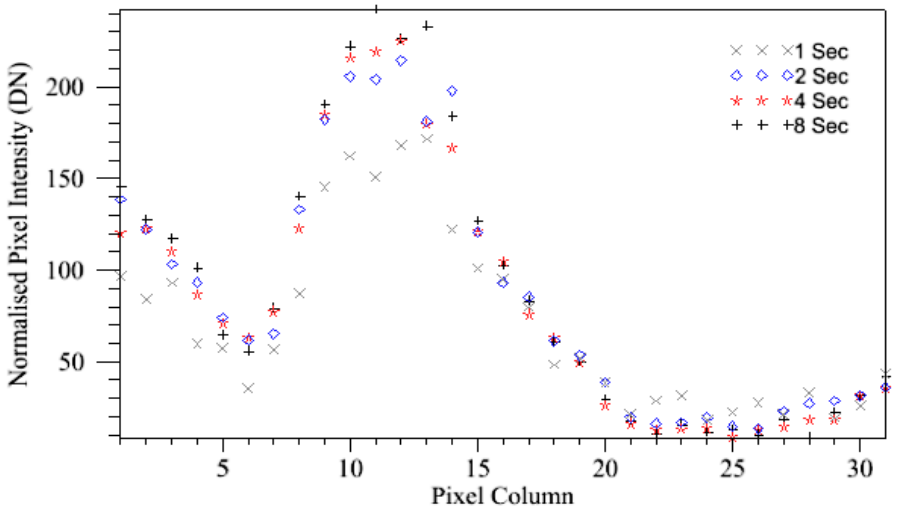

Figure 3.27 Results from sample one image analysis depicting the normalised effect the number of photon counts has on pixel column intensity.

A reduction in the number of photons detected limits the pixel intensity difference between the healthy and suspicious tissue regions. This consequently reduces the detection of the suspicious tissue in the images acquired with fewer photon counts. It can be seen from table 3.32 that 53.8% of the suspicious tissue region is flagged when 15200 photons are detected corresponding to a photon flux of 7600 pho^{-1} sec^{-1} mm^2. This increases to 100% when a detector integration time of eight seconds is used with the same flux, therefore illustrating that a photon flux of approximately 61450 pho^{-1} sec^{-1} mm^2 corresponding to a photon count of 122900 would be ideal in this instance as detector integration times of less than a second are desirable.

Table 3.32 Effect of the statistical quality of data used to obtain EDXRD images of sample 1 on abnormality detection.

Detector Count time (secs)	No. Of photons in profile	Proportion of image flagged as suspicious (%)	Proportion of diseased tissue flagged (%)	Flagged columns in diseased region (%)
8	122900	41.9	100.0	100.0
4	63100	38.7	92.3	100.0
2	31500	35.4	84.6	100.0
1	15200	22.5	53.8	100.0

Ideally, the higher the count rate the better, however in practice a compromise must be established between the detector integration time, angular resolution, sensitivity and specificity. An increased integration time would increase the number of photons detected therefore pontentially increasing both the sensitivity and specificty. This would however consequently result in longer imaging times, where in mamography, this is undesirable. Increasing the angular resolution would also have the desired effect, only to compromise system resolution consequently reducing the probability of detecting smaller masses. As the purpose of this work is to demonstrate EDXRD can be used as an intelligent imaging parameter controller, and not to exhaustively determine the ideal conditions under which it is to work, the remainder of this investigation makes use of the EDXRD images of each breast tissue region obtained using the maximum number of photon counts (corresponding to an eight second detector integration per pixel).

3.12.3 The effect of x-ray beam collimation size

The angular resolution of an imaging system determines whether small objects, i.e. masses are to be detected. In conventional digital mammography systems, x-ray detection comes in the form of either a pixelated CCD array or amorphous

selenium flat panel detector. The spatial resolution is thus governed by both the pixel size and coupled scintillator, or if a direct system is in use, the pixel size. As spatial resolution in diffraction imaging is determined by the angular resolution of the system, the effect of x-ray beam collimation size on the detectability of suspicious tissue regions has been investigated. All three breast tissue regions were imaged three times using the beam optics described in section 2.3.4. A stepping ROI size of one pixel column was used to investigate the pixel intensities of each image (therefore a 1mm × 10mm ROI corresponding to the 1mm wide collimation system, a 2mm × 10mm ROI for the 2mm wide collimation system and 3mm × 10mm ROI for the 3mm wide collimation system was used). The resultant EDXRD images are displayed in figures 3.28, 3.29 and 3.31 where both, momentum transfer windows corresponding to adipose tissue and diseased tissue are displayed.

(a) Transmission x-ray image

(b) Summation window: 1.52 nm^{-1} – 1.71 nm^{-1}

(c) Summation window: 1.02 nm^{-1} – 1.21 nm^{-1}

(d) Summation window: 1.52 nm^{-1} – 1.71 nm^{-1}

(e) Summation window: 1.02 nm^{-1} – 1.21 nm^{-1}

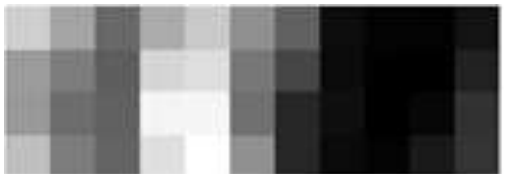

(f) Summation window: 1.52 nm^{-1} – 1.71 nm^{-1}

(g) Summation window: 1.02 nm^{-1} – 1.21 nm^{-1}

Figure 3.28 (a) A 31mm × 10mm x-ray transmission image of a region of tissue obtained from sample 1 used to obtain EDXRD images (b-g) Corresponding EDXRD images of the tissue region imaged using a solid angle of 0.23,0.43 and 0.98msr for images b-c, d-e and f-g repectively.

From the transmission image above (fig 3.28a), it can be seen that breast sample one contains both healthy and suspicious tissue types where the suspicious region is seen in the form of an irregularly shaped mass (left side of image). This region has been previously marked as suspicious by a radiologists (section 2.6).

From figure 3.28b, d and f, it can be seen that the images acquired using a summation window of $1.52nm^{-1}$ – $1.71nm^{-1}$ appear to consist of higher intensity pixels within the first half (left side) of the image hence indicating the presence of an abnormality. The opposite is clearly seen when a momentum transfer window of $1.02nm^{-1}$ – $1.21nm^{-1}$ is used. Figures 3.28 d-g correspond with that of figures 3.28b and 3.28c where it can be seen that the suspicious tissue mass is still distinguishable from healthy tissue based on grey level values.

The effect the solid angle has on the suspicious tissue detectability present in sample one is shown in tables 3.33. It can be seen that the proportion of suspicious tissue highlighted is maximised when a small solid angle is used. It is observed that up to 100% of the suspicious tissue is able to be correctly flagged whilst all the highlighted ROI's are located in the suspicious regions. Past 0.43msr, it appears that healthy tissue regions begin to be treated as suspicious as only 80% of the flagged ROI's are located in the suspicious tissue area.

Table 3.33 Effect solid angle has on abnormality detection within sample one.

Solid Angle (msr)	Proportion of image flagged as suspicious (%)	Proportion of suspicious tissue flagged (%)	No. of Flagged columns in suspicious region (%)
0.23	41.9	100.0	100.0
0.43	37.5	84.6	100.0
0.98	45.4	84.6	80.0

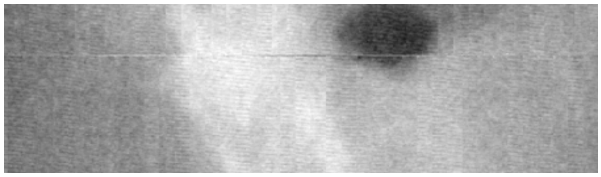

(a) Transmission x-ray image

(b) Summation window: 1.52nm^{-1}–1.71nm^{-1}

(c) Summation window: 1.02nm^{-1}–1.21nm^{-1}

(d) Summation window: 1.52nm^{-1}–1.71nm^{-1}

(e) Summation window: 1.02nm^{-1} – 1.21nm^{-1}

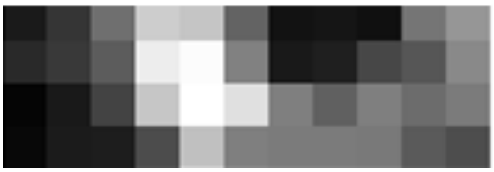

(f) Summation window: 1.52nm^{-1}–1.71nm^{-1}

(g) Summation window: 1.02nm^{-1}–1.21nm^{-1}

Figure 3.29 (a) A 31mm × 10mm x-ray transmission image of a region of tissue obtained from sample 2a used to obtain EDXRD images (b-g) Corresponding EDXRD images of the tissue region imaged using a solid angle of 0.23,0.43 and 0.98msr for images b-c, d-e and f-g repectively.

Tissue sample 2a (fig 3.29), like sample one, contains both healthy and suspicious tissue types. The suspicious region in this sample takes the form of an irregularly shaped mass occupying the second quarter of the image. Although the mass is not seen to visually penetrate the enitire thickness of the sample, hence is

superimposed within healthy tissue, the EDXRD technique is still able to highlight it, where the statistical analysis procedure is able to detect and classify this region as suspicious (fig 3.30). It can be seen from figure 3.30 that the region between 9-15 pixel columns exceeds the threshold level (100DN) therefore consequently will be treated as suspicious. This sample is made up predominatly of adipose tissue as is seen from fig 3.29b and c.

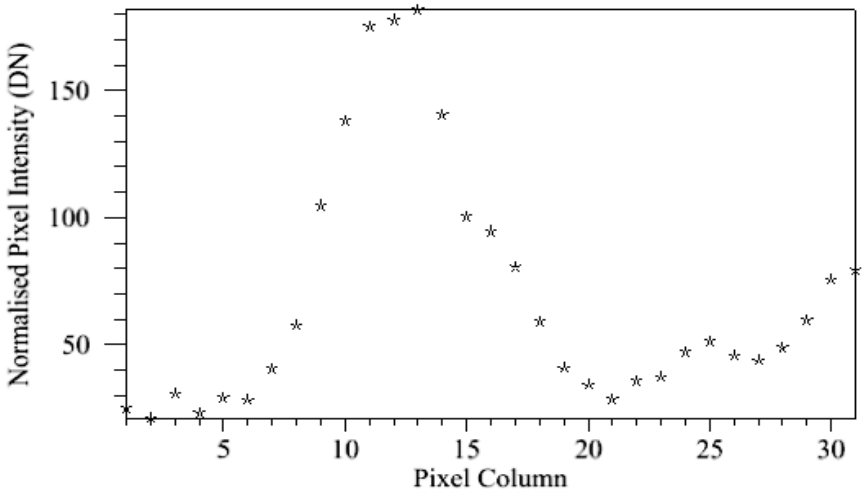

Figure 3.30 Results obtained from figure 3.29b illustrating the column intensity profile of sample 2a.

Table 3.34 suggests that a smaller solid angle is desirable as it is able to highlight an increased proportion of the suspicious tissue compared to larger angles. An improvement in exposure distribution is also observed where less healthy tissue is being flagged as suspicious when the solid angle is reduced as can be seen from the proportion of the total image highlighted.

Table 3.34 Effect solid angle has on abnormality detection within sample 2a.

Solid Angle (msr)	Proportion of image flagged as suspicious (%)	Proportion of suspicious tissue flagged (%)	Flagged columns within suspicious region (%)
0.23	22.5	70.0	100.0
0.43	25.0	61.5	100.0
0.98	27.2	61.5	100.0

The final region investigated also came from tissue sample two and is referred to as sample 2b. Like sample 2a, this segment also consists predominantly of adipose tissue (fig 3.31). A suspicious section is located centrally within the image. The quantitative results (table 3.35) suggest that a solid angle of 0.43msr out performs both smaller and larger angles with respects to suspicious tissue flagging and exposure distribution efficiency respectively.

Table 3.35 Effect solid angle has on abnormality detection within breast sample 2b.

Solid Angle (msr)	Proportion of image flagged as suspicious (%)	Proportion of suspicious tissue flagged (%)	Flagged columns within suspicious region (%)
0.23	29.0	81.8	100.0
0.43	31.2	90.9	100.0
0.98	36.3	90.9	100.0

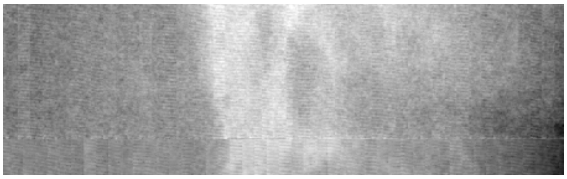

(a) Transmission x-ray image

(b) Summation window: 1.52nm^{-1}–1.71nm^{-1}

(c) Summation window: 1.02nm^{-1} – 1.21nm^{-1}

(d) Summation window: 1.52nm^{-1} – 1.71nm^{-1}

(e) Summation window: 1.02nm^{-1} – 1.21nm^{-1}

(f) Summation window: 1.52nm^{-1} – 1.71nm^{-1}

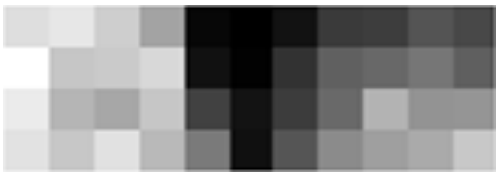

(g) Summation window: 1.02nm^{-1} – 1.21nm^{-1}

Figure 3.31 (a) A 31mm × 10mm x-ray transmission image of a region of tissue obtained from sample 2b used to obtain EDXRD images (b-g) Corresponding EDXRD images of the tissue region imaged using a solid angle of 0.23,0.43 and 0.98msr for images b-c, d-e and f-g repectively.

It has been shown that the system optics used within an EDXRD system is of crucial importance and governs the efficiency to which the intelligent feedback parameter works. Ideally a small solid angle would be used as it limits the amount of healthy tissue unnecessarily flagged as suspicious hence increasing

exposure distribution efficiency. However, it should be noted that this would consequently result in an increase in the data acquisition time as the photon flux decreases with solid angle. Using a smaller solid angle would also increase the chances of detecting smaller abnormalities that would otherwise go undetected by the larger angles.

3.13 Stepping ROI size

Throughout the previous EDXRD investigations the size of the scanning ROI used to analyse the tissue regions has remained constant for a given collimation size (solid angle). A one pixel column wide ROI has been used accompanied by the maximum possible height (10mm as this is the height of the image section). All images examined thus far have been identical in size for a given solid angle. The effects of varying the size of the ROI and hence the quantity of data within each region, is investigated below. Three different ROI sizes have been used to analyse the EDXRD images obtained from all three breast samples. Each image totally or partially incorporated previously identified suspicious tissue regions. This investigation therefore required the further acquisition of larger diffraction images than was previously used in order to investigate the effects of increasing the ROI size (height) beyond 10mm. These larger images would therefore enable changes in the tissue type ratio present within a single pixel column. Images were acquired using identical imaging parameters previously used (see section 2.3). The height (y axis) of each pixel column was changed. Firstly it was doubled from 10mm to 20mm as this enabled the suspicious tissue region to be imaged with ample amounts of surrounding healthy tissue. Secondly, it was then approximately halved from 10mm to 6mm removing this abundance of surrounding healthy tissue. 6mm was used as opposed to 5mm as a collimation

slit height of 2mm was used (hence height being a multiple of 2). A solid angle of 0.23msr was used as it out performed its competitors along with the images obtained using the maximum number of photons investigated (corresponding to an eight second detector count time) ensuring an adequate number of counts was achieved. Figure 3.32, 3.33 and 3.34 display the regions analysed by the three ROI sizes. The stepping ROI size used to analyse the mean pixel intensity of each column for images a, b and c were 1 pixel column x 10 pixels , 1 pixel column × 5 pixels and 1 pixel column × 3 pixels respectively.

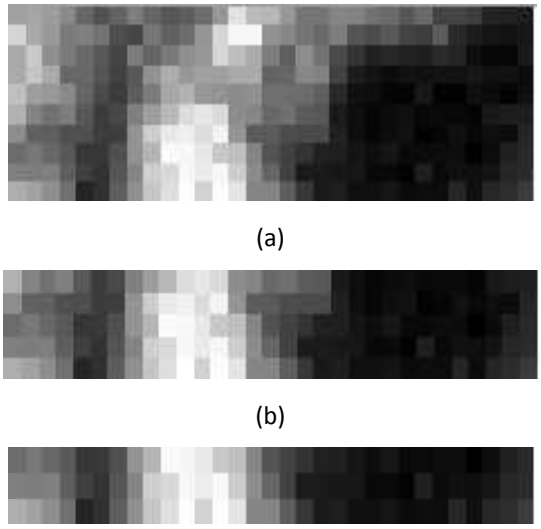

(a)

(b)

(c)

Figure 3.32 EDXRD images of sample 1 corresponding to the area's analysed by three different scanning ROI sizes where a 1 pixel column by 10 pixels, 5 pixels and 3 pixels was used to analyse images a, b and c respectively.

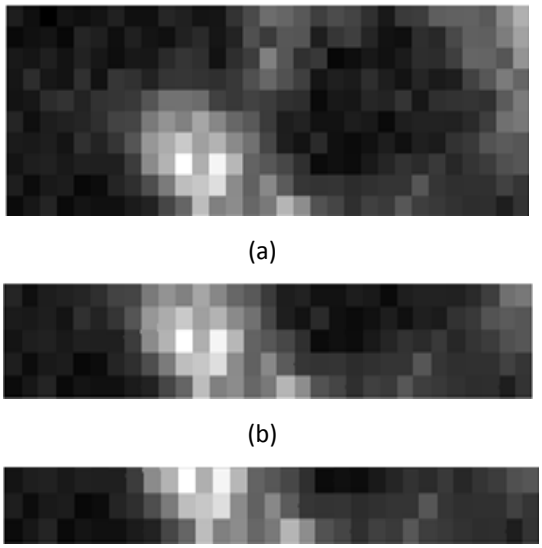

(a)

(b)

(c)

Figure 3.33 EDXRD images of sample 2a corresponding to the area's analysed by three different scanning ROI sizes where a 1 pixel column by 10 pixels, 5 pixels and 3 pixels was used to analyse images a, b and c respectively.

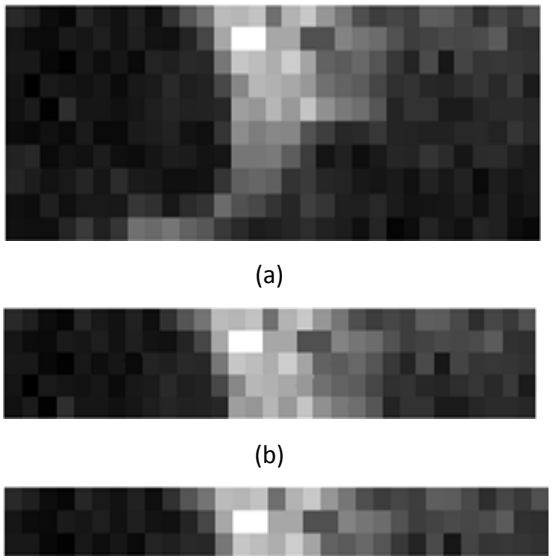

(a)

(b)

(c)

Figure 3.34 EDXRD images of sample 2b corresponding to the area's analysed by three different scanning ROI sizes where a 1 pixel column by 10 pixels, 5 pixels and 3 pixels was used to analyse images a, b and c respectively.

From figure 3.32, 3.33 and 3.34, the partial volume effect became apparent where the area of the ROI occupied by the suspicious tissue region increases as the stepping ROI decreases. This consequently results in the average pixel column intensity increasing, therefore potentially increasing the probability of detecting suspicious tissue regions. However, from figure 3.32, it appears that although the ratio of suspicious tissue with respects to healthy tissue contained within an ROI increases as the ROI size decreases, table 3.36 suggests that due to the intense pixels of the surrounding glandular region being similar to that of the suspicious region, the mean column intensity between an ROI containing just suspicious tissue (3.32b and c) is similar to the larger ROI (3.32a) containing both healthy and suspicious tissue types. This consequently results in 100% of the suspicious region being flagged for the largest ROI size along with the surrounding healthy tissue.

Tables 3.36 and 3.38 demonstrate that the ability to highlight suspicious tissue regions is reduced by at least 45% when an ROI size of 1 pixel column × 10 pixels is used as oppose to a smaller one. In one instance it was observed that 25% of the highlighted regions where unnecessarily flagged as suspicious where only 30% of the suspicious region was highlight (table 3.37). Thus an ROI size of 1 pixel column × 10 pixels is unsuitable for use. Such findings are due to the partial volume effect where the intense pixel grey levels of the suspicious regions are statistically compromised by that of the healthy tissue. Such an effect is reduced when a smaller ROI is used as mentioned above. In contrast, the difference between an ROI size of 1 pixel column × 5 pixels and 1 pixel column × 3 pixels was minimal where only a 10% difference was seen in the proportion of suspicious tissue highlighted (table 3.37). The results were identical for table 3.36 and 3.38.

Table 3.36 Performance characteristics of three different ROI sizes used to investigate the suspicious tissue region within sample 1.

ROI size (Pixel column × Pixel rows)	Proportion of image flagged as suspicious (%)	Proportion of suspicious tissue flagged (%)	Flagged columns within suspicious region (%)
1 × 10	45.1	100.0	92.8
1 × 5	41.9	100.0	100.0
1 × 3	41.9	100.0	100.0

Table 3.37 Performance characteristics of three different ROI sizes used to investigate the suspicious tissue region within sample 2a.

ROI size (Pixel column × Pixel rows)	Proportion of image flagged as suspicious (%)	Proportion of suspicious tissue flagged (%)	Flagged columns within suspicious region (%)
1 × 10	12.9	30.0	75.0
1 × 5	22.5	70.0	100.0
1 × 3	25.8	80.0	100.0

Table 3.38 Performance characteristics of three different ROI sizes used to investigate the suspicious tissue region within sample 2b.

ROI size (Pixel column × Pixel rows)	Proportion of image flagged as suspicious (%)	Proportion of suspicious tissue flagged (%)	Flagged columns within suspicious region (%)
1 × 10	16.1	45.4	100.0
1 × 5	29.0	81.8	100.0
1 × 3	29.0	81.8	100.0

The results suggest that a stepping ROI size of either 1 pixel column × 5 pixels or 3 pixels should be used throughout the remainder of this investigation as they highlight a higher proportion of the suspicious masses.

3.14 Summary

From the EDXRD results presented above, it can be deduced that the use of EDXRD signals in the form of EDXRD images obtained from the breast, can be used to extract useful tissue characterising information therefore leading to the identification of suspicious tissue regions. It has been shown that by using the mean function to analyse the pixel intensity of these EDXRD images, it is possible to differentiate between the two tissue regions consequently promoting real time imaging parameter optimisation.

The results of the above investigations have lead to the identification of a set of optimum intelligent imaging parameters. It has been demonstrated (section 3.12.1) that a threshold value corresponding to 40% of the dynamic range of the EDXRD images is an ideal value assigned to govern the differentiation of the tissue types by the mean function as it is seen to maximise the proportion of suspicious tissue highlighted whilst minimising the amount of healthy tissue incorrectly flagged. Section 3.12.3 has shown that the smaller the solid angle (x-ray beam collimator slit widths) used the greater the exposure distribution efficiency hence the tissue differentiation capability of the feedback algorithm. It can be seen from section 3.13 that the smaller the stepping ROI used to analyse the EDXRD image, the greater the amount of suspicious tissue highlighted.

Table 3.32 demonstrates that suspicious tissue region detection is possible when as few as 15200 photons are detected (corresponding to an incident exposure of $3.9\mu Ckg^{-1}$). This therefore suggesting a linear array of energy resolving detectors integrating for one second spanning the length of the image would be sufficient for I-ImaS system integration. As statistical quality of the data is proportional to photon flux, a wider collimation system may be useful increasing the number of

counts detected however will compromise the achievable spatial resolution of the system.

Chapter Four

Intelligent Images

4.1 Intelligent Image production

The previous chapter demonstrated that tissue information could be extracted and analysed, therefore potentially enabling a real time image optimisation technique to be implemented into the data acquisition phase of the image acquisition procedure. This optimisation technique attempts to enhance the diagnostic quality of mammograms. The combined feature function used the grey level pixel intensity of small regions of interest to determine whether a specific tissue region contained suspicious tissue. It was demonstrated that by using appropriate thresholds and/or scout images, the suspicious tissue regions within a low exposure mammogram or EDXRD image could be successfully differentiated from the surrounding healthy regions. The intelligent images presented within this chapter were simulated using a single threshold value were the incident exposure was modulated by x-ray beam attenuation filters in an attempt to investigate the maximum CNR achievable using the proposed methods.

The I-ImaS system used to acquire images within this investigation was unable to be implemented in real-time mode consequently resulting in the simulation of I-ImaS intelligent images. The simulating of these intelligent I-ImaS images were governed by the results obtained from the experimental investigations undertaken in the previous chapter in an attempt to produce optimised I-ImaS intelligent images. In order to simulate a real-time change in incident exposure, a set of conventional images were acquired using the I-ImaS system each at a different incident exposure as discussed in section 3.5.1.

4.2 Combined feature function results

Seven of the eight tissue regions presented in section 3.6 were used to generate intelligent images. The 8th sample section comprised of healthy tissue only. An exposure level of 19.0μCkg^{-1} was used as the scout exposure whilst the threshold governing SynF_1 was derived from a rectangle 1mm × 15mm in size located directly under the skin. This corresponded to the approximate size of an individual I-ImaS sensor (32 pixels × 512 pixels). The threshold pertaining to SynF_2 was set to 250Arb.U. The scout images were analysed using the combined feature function described in section 3.3.2. The size of the scanning ROI used to extract statistical information from the scout images was 32 pixel columns wide by 490 pixel columns high. This ROI was stepped across the image in one pixel column steps. As the ratios of suspicious and unsuspicious tissue making up each intelligent image was known, along with the corresponding exposures used to obtain each region, the total exposure level used to obtain each intelligent image could be calculated.

Figure 4.1 shows the results of the intelligent algorithm in the form of exposure maps. These maps correspond to the regions of tissue flagged as suspicious by the algorithm therefore are the tissue regions to be imaged with an increased incident exposure. The black regions within each image segment represent the tissue areas that were not highlighted as suspicious, hence imaged with a scout exposure only. These exposure maps also show the intensity of each pixel within the suspicious region where it is observed that the feature function combination highlights the most intense (i.e. suspicious) regions well in all instances.

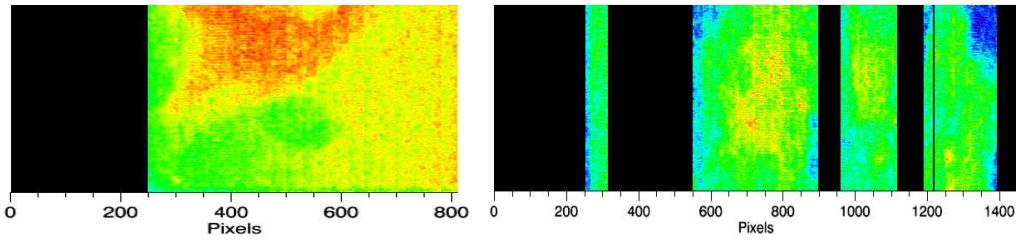

(a) Exposure map: sample1 section 1 (b) Exposure map: sample 1 section 2

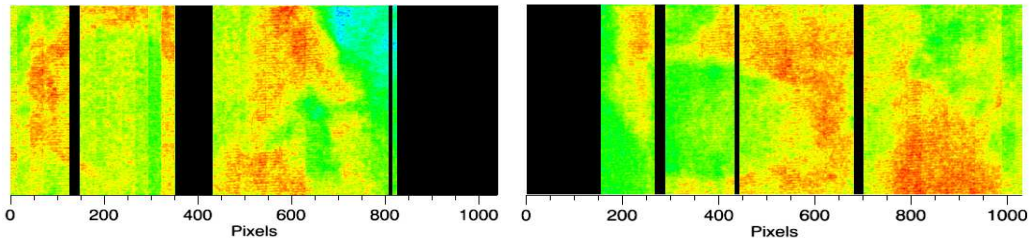

(c) Exposure map: sample 1 section 3 (d) Exposure map: sample 1 section 4

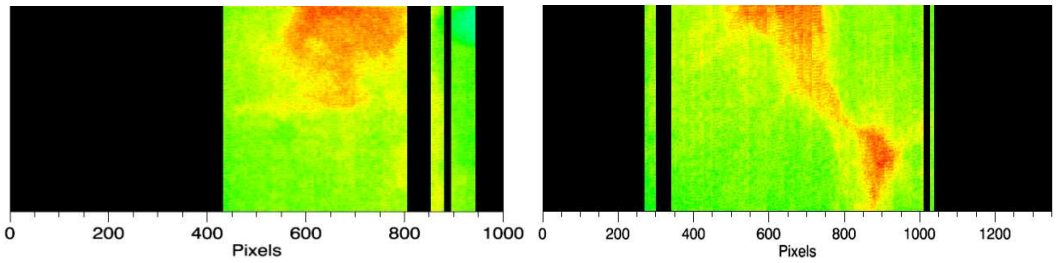

(e) Exposure map: sample 2 section 1 (f) Exposure map: sample 2 section 2

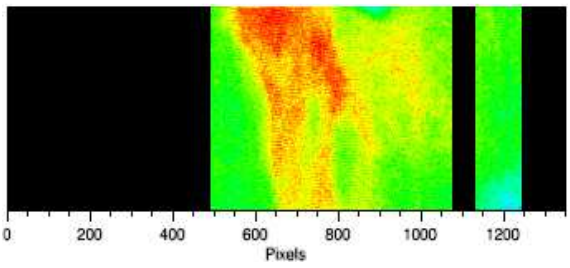

(g) Exposure map: sample 2 section 3

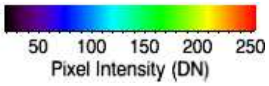

Figure 4.1 Exposure maps obtained from scout images depicting the regions highlighted as suspicious by the intelligent algorithm. The black areas represent the regions not flagged as suspicious.

Once the exposure maps were obtained, intelligent Images were simulated according to equation 4.1.

$$\text{Intelligent I-ImaS image} = \text{Scout image at all points} + \text{Adapted exposure image at suspicious points} \quad \text{(Eq. 4.1)}$$

The parts of the images corresponding to the suspicious regions, that is, the regions corresponding to the exposure maps, were imaged with an increased level of exposure ($24.8\mu Ckg^{-1}$). This increase corresponded to a single attenuation filter step where an exposure level of $19.0\mu Ckg^{-1}$, the scout exposure, was the last step prior to the maximum unfiltered exposure level ($24.8\mu Ckg^{-1}$). Figure 4.2 illustrates the first optimised intelligent images of real breast tissue produced by the I-ImaS imaging system. By means of comparison, it can be seen from figures 4.2 and 4.3 that all of the information relating to the suspicious regions is retained. The CNR calculated according to Young et al (2006) along with the exposure comparisons for each image is depicted in table 4.1.

Three of the seven (42%) intelligently produced images resulted in an increase in the CNR. Two of the four image sections investigated from within sample 1 (Sample 1 sections 1 and 2) demonstrated increases of 5.3% and 2.2% respectively. These increases were accompanied by decreases in the exposure level used to obtain the images as seen in table 4.1. Although sample 1 section 3, 4 and sample 2 sections 1 and 2 do not show an increase in the CNR when compared to the conventionally acquired images, three of the four show similar CNR's whilst the exposure incident on all sections has been reduced. Sample 2 section 3 demonstrated a CNR increase of approximately 4.2%. Again, this image was acquired using an approximate exposure reduction of 10%.

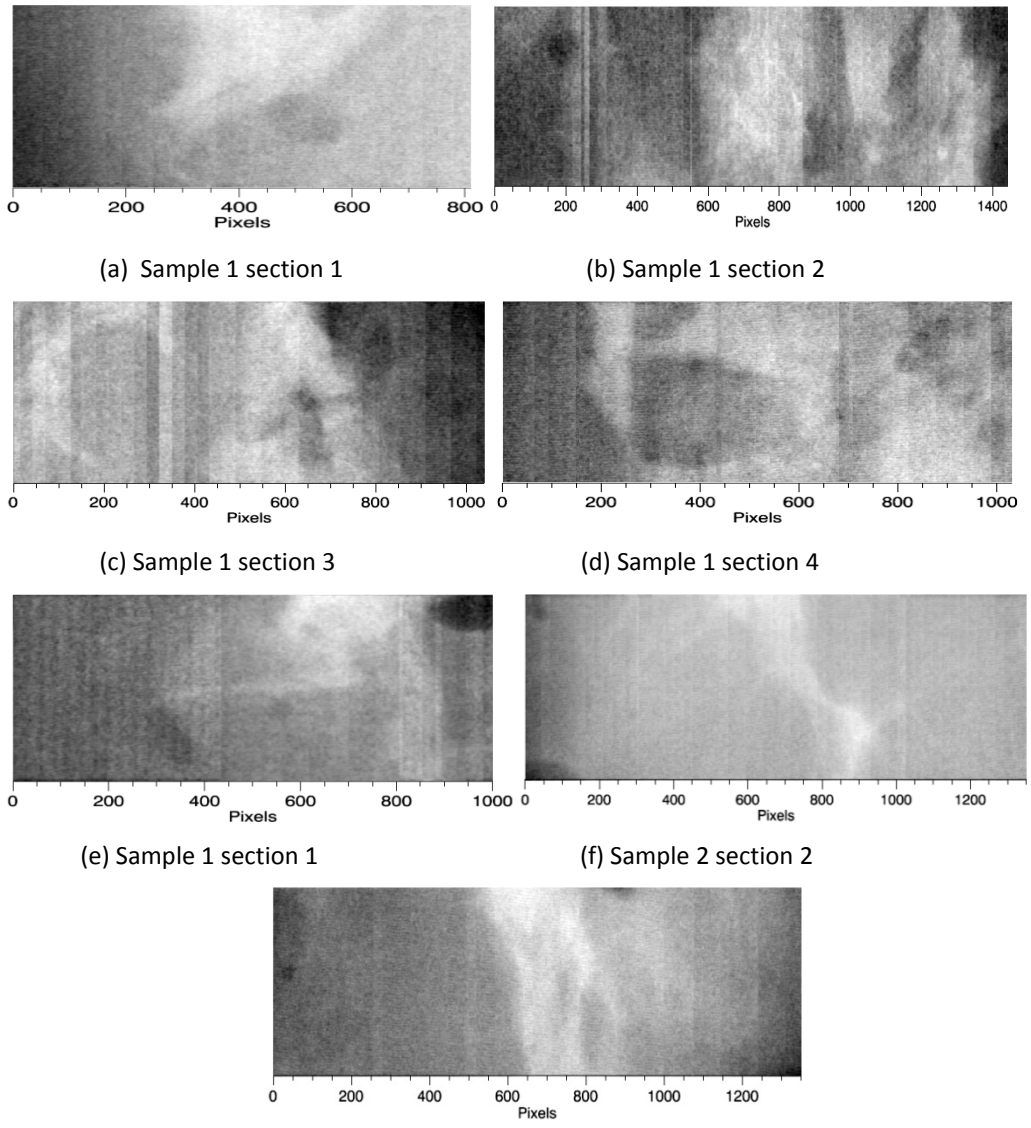

(a) Sample 1 section 1

(b) Sample 1 section 2

(c) Sample 1 section 3

(d) Sample 1 section 4

(e) Sample 1 section 1

(f) Sample 2 section 2

(g) Sample 2 section 3

Figure 4.2 I-ImaS intelligent images produced using exposure maps derived from the statistical content extracted from breast tissue one and two using a scout exposure of 19.0μCkg^{-1}.

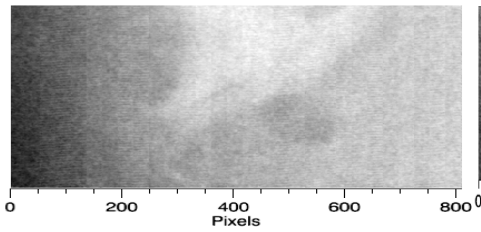

(a) Sample 1 section 1

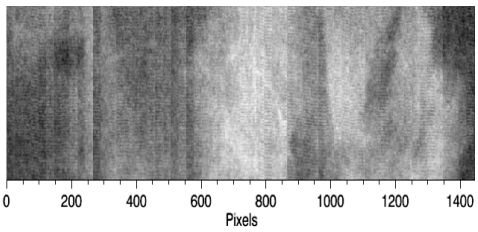

(b) Sample 1 section 2

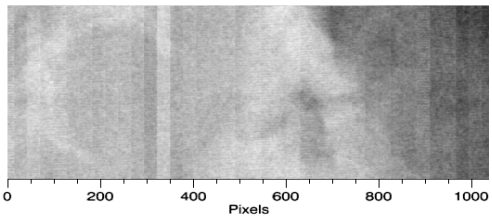

(c) Sample 1 section 3

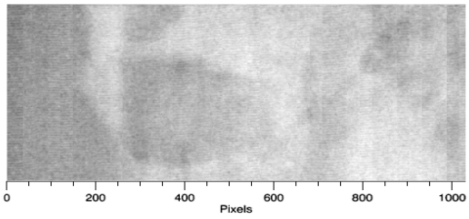

(d) Sample 1 section 4

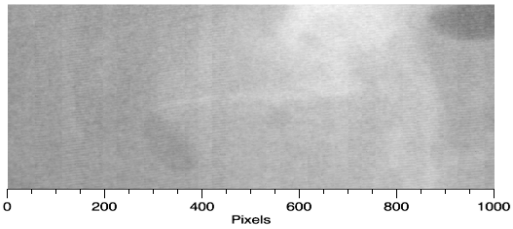

(e) Sample 2 section 1

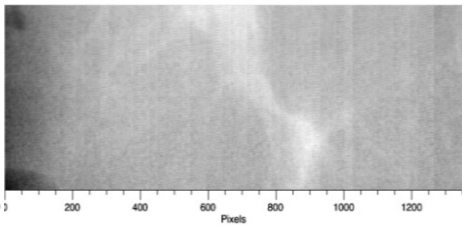

(f) Sample 2 section 2

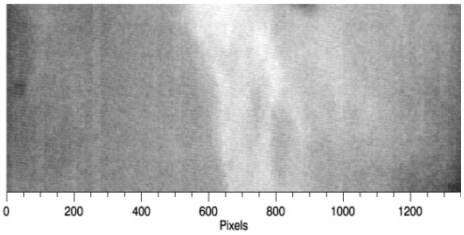

(g) Sample 2 section 3

Figure 4.3 Conventional images acquired using an exposure of 24.8µCkg^{-1} (no exposure reduction) implementing no feedback intelligence.

Table 4.1 Image quality and incident exposure results obtained from breast samples one and two intelligent images obtained using a scout exposure of 19.0μC/kg.

Sample	Intelligent image CNR	Conventional image CNR (filter 5)	Intelligent image exposure (μCkg^{-1})	Conventional image exposure (μCkg^{-1})	Total exposure reduction (%)	CNR difference (%)
Sample 1 section 1	13.9	13.2	22.9	24.8	7.7	5.3 increase
Sample 1 section 2	4.1	4.0	22.0	24.8	11.3	2.5 increase
Sample 1 section 3	10.1	10.4	22.1	24.8	10.9	2.9 decrease
Sample 1 section 4	8.0	8.1	19.5	24.8	21.4	1.0 decrease
Sample 2 section 1	7.2	9.9	22.9	24.8	7.7	27.3 decrease
Sample 2 section 2	5.5	5.6	22.0	24.8	11.3	1.8 decrease
Sample 2 section 3	9.8	9.4	22.3	24.8	10.1	4.2 increase

From the results present above, it can be deduced that the use of grey level pixel value feature extraction, leading to the production of intelligently optimised I-ImaS images, is beneficial. An improved CNR as well as an incident exposure reduction is achieved.

Figure 4.4 illustrates the pixel intensity profiles taken from sample 2 section 3. The plot compares the pixel intensities from the intelligent I-ImaS image and the conventional image acquired implementing no exposure modulation using a scout exposure of 19.0μCkg^{-1}. It is observed that the I-ImaS profile tends to exhibit higher pixel intensities than that of the conventional image. This corresponds to the region imaged with an increased incident exposure (24.8μCkg^{-1}) consequently giving rise to the increase CNR seen in table 4.1. The exact regions used to compute the CNR for each image section in the table are identical to those initially used in section 3.4.2 and are shown throughout figures 3.12 – 3.15.

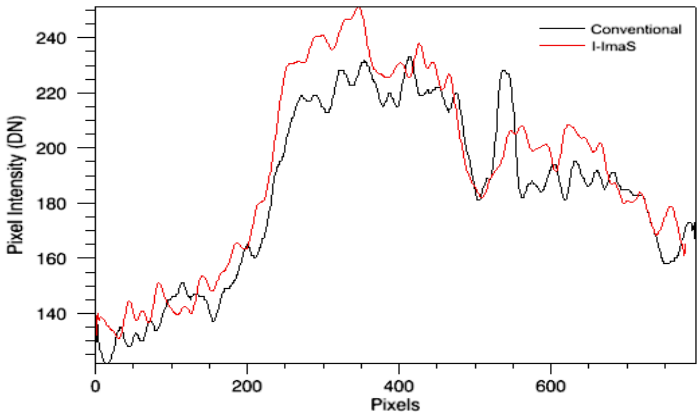

(a)

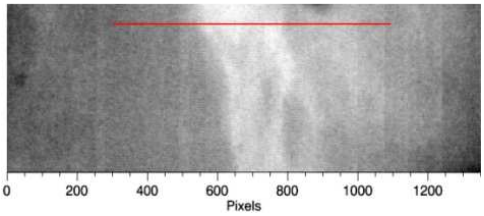

(b)

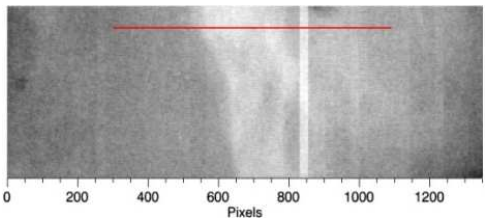

(c)

Figure 4.4 (a) Line profiles across suspicious tissue region in sample 2 section 3 obtained from the intelligent I-ImaS image and the conventionally acquired image implementing no exposure modulation (b)Region of tissue used to obtain line profile in intelligent I-ImaS image (c) region of tissue used to obtain line profile in conventional image.

4.3 Summary

An increase in the CNR for five of the seven intelligently simulated I-ImaS images obtained using a scout exposure of 19.0μCkg^{-1} was observed in comparison to

the conventional transmission images obtained using an exposure of 24.8μCkg^{-1}. A total exposure reduction was demonstrated in all instances.

4.4 EDXRD results

The simulated intelligent I-ImaS images obtained from the EDXRD investigation are presented below. Three regions of interest from within the area deemed as suspicious by the radiologist (section 2.6) were selected from samples one and two to be imaged using the EDXRD technique. The optimum parameters yielded from the previous chapter were used. Figure 4.5 illustrates the corresponding x-ray exposure maps demonstrating the EDXRD techniques' ability to differentiate between healthy and diseased tissue types based on grey level pixel values. It can be seen that the algorithm used to differentiate tissue types enables a distinction between healthy and suspicious tissue regions to be made without the need for complex statistical feature functions; consequently minimal computational time and processing power is required. The figure shows that by using the mean function as a means of analysing each stepping ROI, the majority of the suspicious area within the tissues can be highlighted whilst minimising the flagging of the surrounding healthy regions. As a result of this, it therefore becomes possible to alter the incident exposure to these flagged regions only, whilst maintaining or reducing the exposure to the healthy regions.

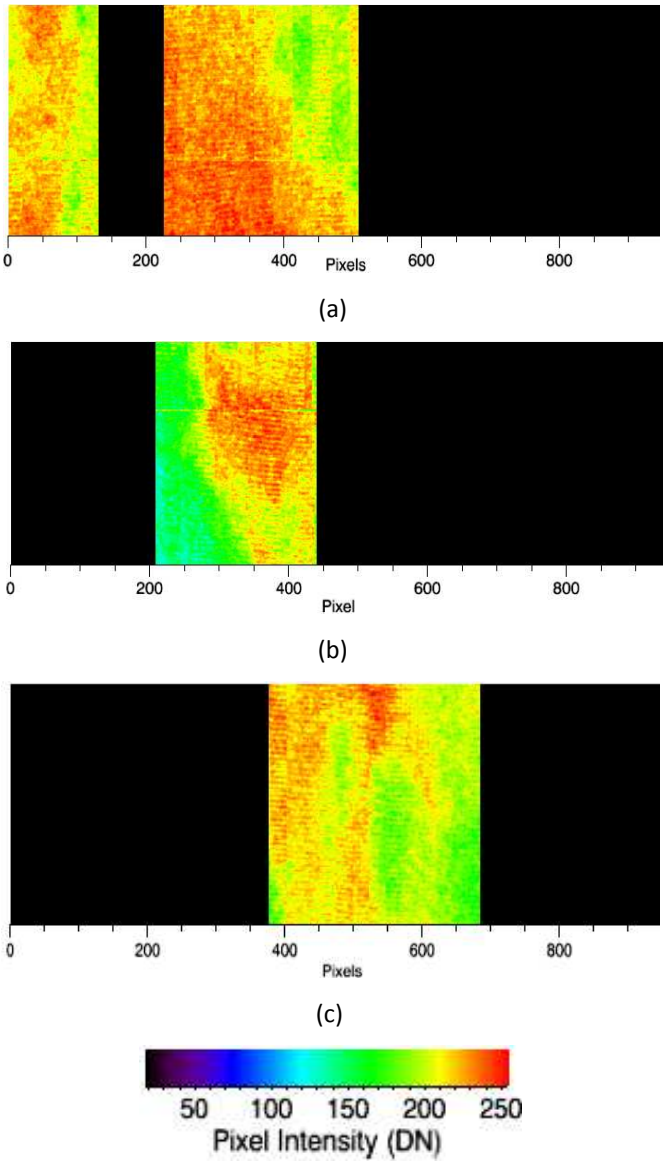

Figure 4.5 (a – c) Exposure maps corresponding to suspiciously flagged tissue regions obtained from samples 1, 2a, and 2b respectively where black region represents tissue regions not highlighted as suspicious.

An image made up of several different exposures would theoretically act to increase the image contrast between given regions therefore acting to possibly increase abnormality detection. However, as image qualities differ from region

to region, the CNR yield may possibly be reduced in the intelligent images as the noise in specific regions (those acquired with low exposures) will increase.

The simulated intelligent images comprised of a base exposure of 13.3μCkg^{-1} where this exposure was used for two main reasons. Firstly, because the suspicious regions in all the tissue sample sections investigated in section 3.5 imaged using this exposure were visible. Secondly, this exposure represents a single attenuation step decrease from the step used in the previous section (where a low exposure mammogram was statistically investigated), therefore, as the CNR was seen to increase using a scout exposure of 19.0μCkg^{-1}, this investigation would determine if a lower exposure could yield similar results. The exposure corresponding to the regions highlighted by the EDXRD signal (fig 4.5) were imaged using an increased incident exposure corresponding to 24.8μCkg^{-1}.

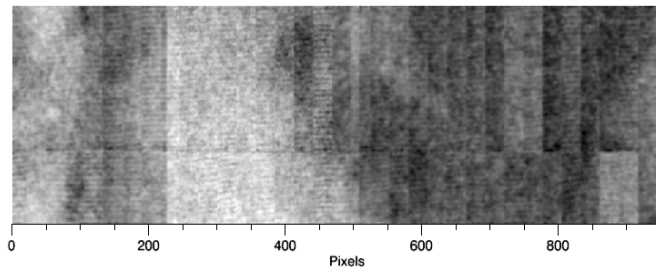

(a)

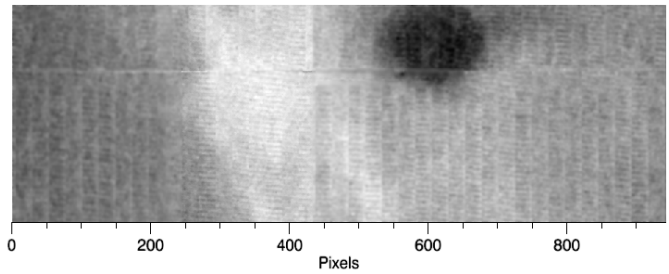

(b)

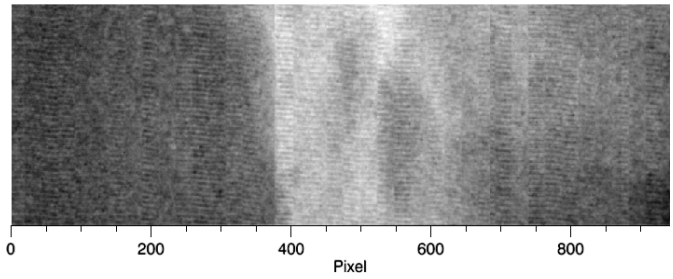

(c)

Figure 4.6 Intelligent images consisting of scout exposure transmission image columns (13.3μCkg^{-1}) and columns aqcuired with a higher incident exposure (24.8μCkg^{-1}). (a) sample 1 aqcuired with a total image incident exposure of 18.1μCkg^{-1} (b) sample 2a aqcuired with a total image incident exposure of 15.8μCkg^{-1} and (c) sample 2b aqcuired with a total image incident exposure of 16.6μCkg^{-1}.

The CNR between the suspicious and healthy regions of the intelligent images were 6.3, 8.0 and 3.9 corresponding to figures 4.6a, 4.6b and 4.6c respectively; compared to the conventionally acquired images acquired with no filtration displaying CNR's of 6.5, 10.4, and 4.1 for 4.7a, 4.7b and 4.7c respectively.

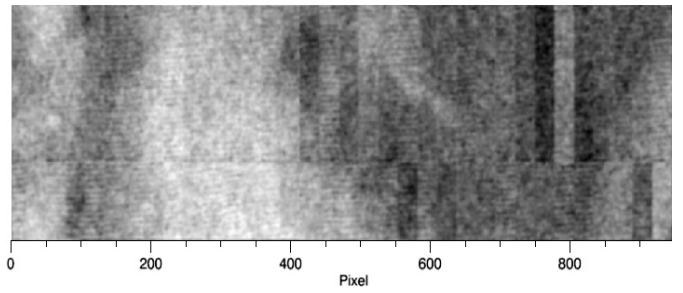

(a)

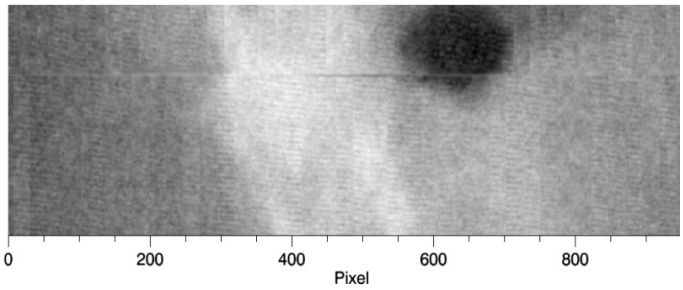

(b)

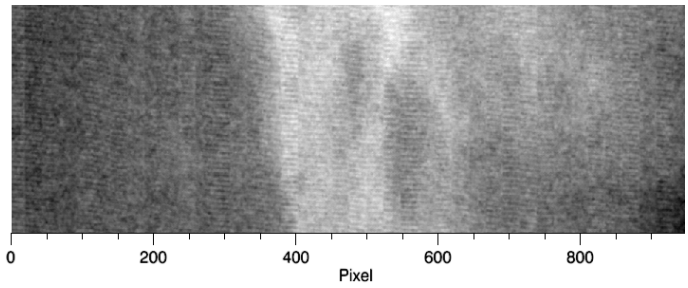

(c)

Figure 4.7 *(a - c) Conventional transmission images of sample 1, 2a and 2b* corresponding to a, b and c respectively. In all three instances an increased incident exposure was used (24.8μCkg^{-1}).

The radiosensitive nature of breast tissue means that during the imaging procedure, the incident exposure should be minimised as much as possible, however, a trade off becomes apparent with respects to image quality (CNR). The intelligently produced images above (fig 4.6) were acquired with a reduced total exposure incident on each sample in comparison to the conventionally acquired images.

Samples 1 and 2b showed only a minimal difference in CNR. This minimal difference was achieved with a 24.6% and a 33.0% reduction in the total image exposure. Sample 2a showed a 23.1% decrease in the CNR ratio from 10.4 to 8.0 for the conventional and intelligent image respectively. Qualitatively, there appears to be minimal difference in the diagnostic quality of the intelligent and conventional images. The lower CNR is due to the background area corresponding to the section of the image acquired with the base exposure. This lead to the intelligent image containing a higher noise component to that of the conventionally acquired image, where the standard deviations were 11.3% and 9.7% of the mean ROI pixel value respectively.

Higher CNR ratios are thought to be obtainable using an alternative EDXRD intelligent imaging concept. This alternative method would act to increase the incident exposure to diseased tissue whilst maintaining the conventional exposure to healthy tissue regions, as oppose to the demonstrated technique of attempting to increase the CNR by reducing the exposure to healthy tissue regions, from that of the conventional image, whilst maintaining the exposure incident on diseased regions. This alternative method would seek to increase the total image exposure in comparison to a conventional image, hence not reducing the total incident exposure to healthy tissue regions.

4.5 Comparison of both methods

From the results presented in this chapter thus far, it has been demonstrated that the use of a combined feature function or the EDXRD signal yielded by the breast can be used as a feedback mechanism within an adaptable imaging system. It has been shown that both methods act to highlight a significant

proportion of the suspicious tissue regions whilst maintaining an exposure reduction incident to the healthy regions.

The final work presented in this thesis is a comparison of the two information feedback techniques. The three tissue regions used to investigate the EDXRDs functionality (fig 4.7) have been analysed using the combined feature function (described throughout chapter 3 and used in chapter 4 section 4.2). This has enabled a direct performance comparison to be made. The results are present below (fig 4.8).

Figure 4.8 illustrates that although both modalities are able to highlight the suspicious tissue regions when embedded in fatty glandular tissue, the EDXRD technique appears to outperform the combined feature function when required to differentiate between suspicious tissue and dense glandular tissue. This can be seen from figures 4.8a and 4.8d. It is observed that none of image 4.8a is flagged as suspicious; therefore the suspicious tissue region present is gone undetected. The corresponding image (4.8d) obtained using the EDXRD feedback mechanism enabled approximately 93% of the suspicious region to be correctly flagged. This was achieved with approximately 60% of the total image remaining unsuspicious, hence being imaged with a reduced exposure.

Figure 4.8b and c demonstrate the ability of the combined feature function to correctly highlight 100% of the suspicious tissue regions in sample 2a and 2b respectively. In comparison, the EDXRD method flags 70% and 82% of the suspicious regions respectively. Although this is a lower proportion of the suspicious tissue, a 63% and 47% reduction in the total proportion of tissue flagged was observed. It can be seen from figures 4.8b and 4.8c that the

suspicious regions highlighted are accompanied by more surrounding healthy tissue than the corresponding EDXRD images (fig 4.8e and f).

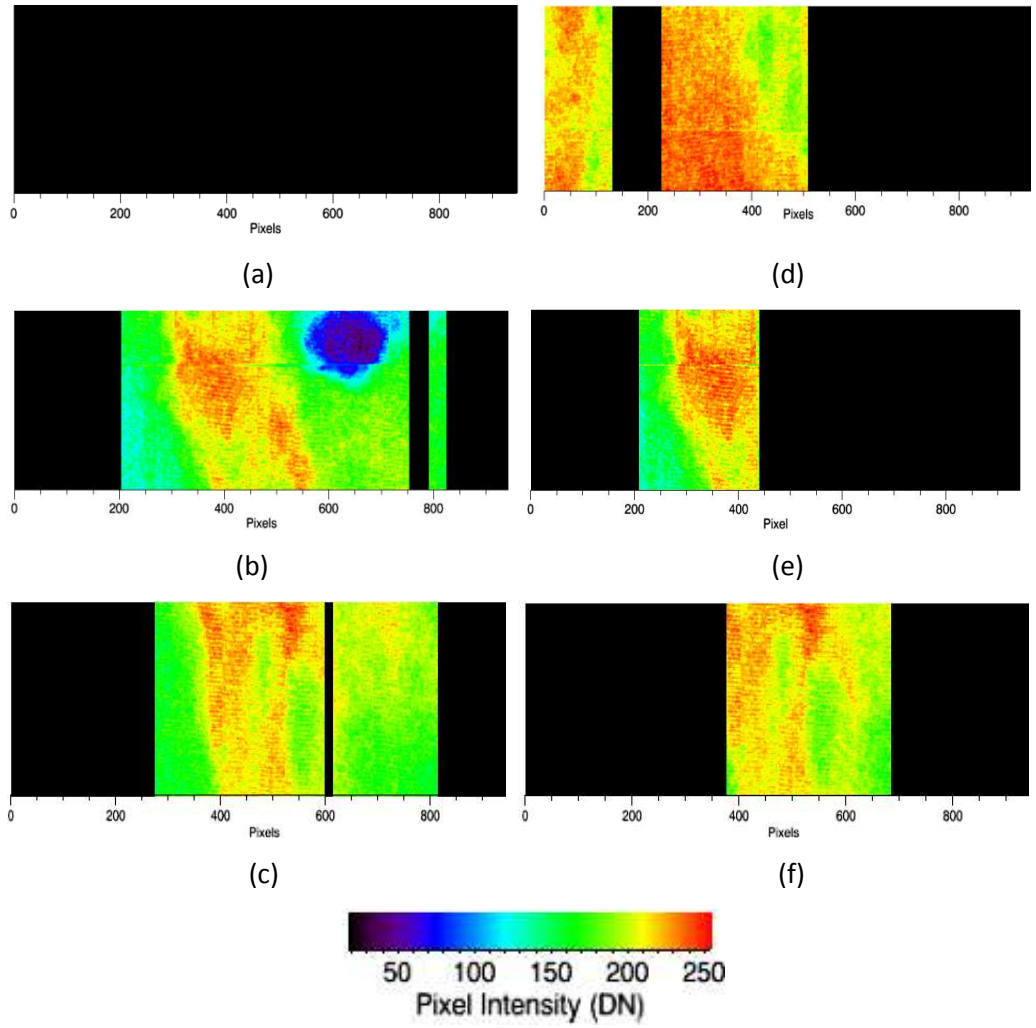

*Figure 4.8 Modality comparison (a - c) Exposure map of low exposure (19.0*µCkg^{-1}*) images analysed using the combined feature function. Images a, b and c correspond to EDXRD images of sample 1, 2a and 2b respectively. (d – f) Exposure maps of identical tissue regions analysed in a – c, regions analysed using EDXRD feedback mechanism.*

It is believed that the limitation of the combined feature function seen in figure 4.8a was due to a relatively high threshold being set to govern SynF_1. This was

due to the initial regions from where the threshold is derived consisting predominately of suspicious tissue.

4.6 Summary

The investigation as to whether EDXRD can be used within the I-ImaS feedback mechanism has been completed. The results displayed above demonstrate that a similar image quality to conventional transmission imaging is obtainable using the intelligent imaging concept. The use of the EDXRD signal as a parameter controller has lead to a 46% incident exposure reduction to at least 58% of the total image area for all images. The results from section 4.5 demonstrate that both techniques are able to detected suspicious tissue regions within the breast, however, EDXRD appears to perform well highlighting at least 70% of the suspicious regions in all instances.

Chapter Five

Conclusion

5.1 Overview

The aim of the investigation reported in this thesis was to demonstrate that the concept of imaging parameter optimisation, based solely on the statistical content of the breast sample being imaged, is beneficial within digital mammography. It enables a reduction in the level of exposure incident on healthy tissue regions whilst maintaining/increasing the exposure incident on diseased tissue regions. As a result, it is thought that these 'intelligently' acquired images will be of improved diagnostic quality to that of conventionally produced images or at least of equivalent quality at a reduced dose. Successful proof of concept would mean other applications such as homeland security could potentially benefit also; where an intelligent feedback mechanism could be used for example, to control the speed of a baggage scanner.

Currently, there is no such imager that has the ability to acquire mammograms in such a manner. The requirements of such a system would include the ability to acquire a low exposure image as well as a final image simultaneously. Secondly, the system would require a real time feedback mechanism enabling a means of data extraction, analysis and parameter optimisation. Finally, the feedback mechanism would have to be of low complexity complying with the stringent time constraints governing breast imaging. A potential solution is found within the bespoke I-ImaS system.

The ability of the I-ImaS system to acquire two mammograms simultaneously, each with a different exposure if required, fulfils the first requirement stated above. The second and third requirement are software issues with are limited by current technological advances therefore are possible and are demonstrated within this thesis.

Two very different information extraction techniques were tested. The first technique involved the statistical interrogation of a low exposure transmission image of the sample; whilst the second technique demonstrated the concept of using coherent scatter profiles. The techniques presented within this thesis, which are summarised below, can help identify new imaging techniques which may lead to future imaging enhancements, ideally, a more efficient x-ray exposure diagnosis.

5.2 Intelligent imaging based on low exposure scout images

The aim of this investigation was to determine whether the statistical information contained within a low exposure mammogram, could be extracted in real time during the image acquisition procedure. This information would form the basis of a feedback mechanism which would optimise the imaging parameters ultimately leading to an intelligently produced image. This image would possess a similar, if not increased, image quality to that of a conventional image, however, would be obtained with a lower exposure.

Transmission images of two breast samples were acquired using an aluminium filtered tungsten x-ray tube operated at 30kVp and 7mA. Images were acquired at five different exposure levels by the I-ImaS system. Each image was obtained using a single exposure leading to the production of five separate images consequently enabling the simulation of a single intelligently acquired image. The next step was to derive a means of feature extraction. Synthetic feature functions, $SynF_1$ and $SynF_2$, were used as they were seen to perform well

highlighting abnormalities throughout the preliminary database image investigation.

The statistical information from within the 'scout' image was then extracted using a stepping ROI which was stepped across the segmented mammogram whilst analysing pixel intensities. The effect the size (width) of this ROI had on suspicious tissue detectability was investigated where it was concluded that a 32 pixel wide (sensor sized) ROI was suitable for implementation as it highlight at least 82% of the suspicious tissue area in all image segments investigated.

Each ROI gave rise to a single, averaged intensity value which was then compared to a threshold value which ultimately determined whether the ROI was suspicious or not. The suspicious tissue regions gave rise to higher intensity pixel values than that of the surrounding healthy regions consequently enabling them to be distinguished. The final feature function thresholds were experimentally determined and selected based on performance.

The CNR for three (42%) of the intelligent images increased. These images were obtained using a scout image exposure corresponding to 23% below that of the unfiltered conventional image ($24.8\mu Ckg^{-1}$). These CNR increases were also accompanied by an incident exposure decrease on average of 9%. Although the remaining two images experienced CNR decreases, an average exposure reduction of approximately 13% was seen. These results demonstrate, firstly, that the use of simple feature functions can be used to extract, analyse and therefore identify tissue regions within a breast sample that were deemed as suspicious by a qualified radiologist. Secondly, it has been demonstrated that an increase in image quality is achievable accompanied by a reduction in the level of

exposure incident on the healthy tissue regions; therefore the majority of the breast, when the investigated concept is used.

5.3 EDXRD based intelligent imaging

It was thought that as breasts containing cancerous tissue are composed of various tissue types, they therefore vary in structure and composition. A means of categorically differentiating tissue types during a breast scan could potentially lead to a more efficient way of imaging the radiosensitive breast. The exposure level the breast would be exposed to could be optimised. With this optimisation, the diagnostic quality of the image may also be enhanced, therefore the benefits are twofold.

As EDXRD provides a means of quantitatively identifying tissue types, its use within digital mammography could potentially prove highly beneficial. If the diffraction signal could be used as an imaging parameter controller, healthy tissue regions could be imaged with a reduced exposure in comparison to suspicious tissue regions. As a consequence, the total breast exposure would be reduced.

To satisfy the requirements of using the diffraction signal as a means of imaging parameter control, two separate experiments were setup. One to obtain transmission images of the breast samples and the other to obtain their x-ray diffraction signals. The combining of the two modalities would then enable intelligent image production.

The diffraction signal from the breast samples were obtained using a tungsten x-ray source operated at 60kVp. A nominal scatter angle of 6^{o} was selected as it had been shown to be optimal for EDXRD breast tissue studies (Kidane et al (1999)). The effects the statistical quality of the data, the angular resolution, stepping ROI size used to analyse the pixel intensities and the feature function threshold value had on suspicious tissue detectability were investigated. However, as the focus of this work was to prove the concept outlined earlier, parameter selection with regards to the above listed factors was based on performance rather than practicality, i.e. image acquisition time, data processing time, kVp etc.

Having simulated EDXRD guided intelligent images it became clear that the use of the diffraction signal as a parameter controller is beneficial as 70% of the suspicious tissue regions in each image was highlighted. Similar diagnostic quality images were able to be acquired using a lower incident exposure than those images acquired using no intelligence, i.e. conventional transmission images acquired using no filtration. The exposure incident on healthy tissue regions was seen to be reduced by up to 46%. However, it should be noted that this exposure accounts for the acquisition of the transmission images only and in order to produce EDXRD guided images in practice, a means of coherent scatter extraction using the already present transmission beam would ideally be devised.

5.4 Conclusion

Through experimental demonstration, real time imaging parameter optimisation has shown signs of being a beneficial, novel, breast imaging technique. It has been demonstrated that intelligently produced images acquired with the use of

x-ray beam attenuation filters can give rise to increased image qualities compared to conventional transmission (using no filtration) images. Increases in the CNR were seen for the majority of sample sections investigated using the technique described in chapter three. However, this investigation was hindered through breast sample limitations where many more breast tissue samples would be required in order to obtain statistically sound results. All possible breast tissue disease types would ideally need to be obtained in order to fully characterise the systems abnormality detection performance.

The design limitations of the current I-ImaS system quickly become apparent throughout this investigation. As its design does not accommodate for EDXRD data collection, a separate investigation had to be set up. Ideally, future I-ImaS system designs could possibly implement a single row of sensors, possible CMOS APS, dedicated to collection of diffraction data as this no longer has to be in the form of a cumbersome HPGe detector as demonstrated by Bohndiek et al (2008).

As the I-ImaS is a scanning system, breast tissue data is acquired in steps. This therefore means that only the data that has been currently acquired can be used for image analysis. This can limit the statistical analysis procedure. Ideally, a large flat panel would be used instead of two dual arrays which would capture an entire low exposure scout image immediately. As CMOS APS promote windowing, a linear array of pixel columns within the flat panel could be activated only, consequently enabling the 'filling in' of exposure to suspicious tissue regions as the sample is scanned past this array. This method would increase the time the statistical algorithm had to analyse the scout image as it would have been acquired before the initiation of the scanning phase. Such an imaging technique would also potentially lead to a reduction in scanning time as the system could be setup such that only the suspicious regions were scanned

with a reduced translation speed past the linear array as oppose to the entire sample moving at a constant speed.

Reference List

Åslund. M, Cederström. B, Lundqvist. M and Danielsson. M (2005), AEC for scanning digital mammography based on variation of scan velocity. *Med. Phys.* 33(11): pp. 3367-3374

Andersson. I, Ikeda. D.M, Zackrisson. S, Ruschin. M, Svahn. T, Timberg. P and Timberg. A (2008), Breast tomosynthesis and digital mammography: a comparison of breast cancer visibility and BIRADS classification in a population of cancer with subtle mammographic findings, *Euro Radiol* 18: pp. 2817-2825

Arvantis. C. D, Bohndiek. S. E, Royle. G, Blue. A, Liang. H. X, Clark. A, Prydderch. M, Turchetta. R and Speller. R (2007), Emperical elctro-optical and x-ray performance evaluation of CMOS active pixels sensors for low dose, high resolution x-ray medical imaging, *Med. Phys*. 34 (12), pp. 4612-4625

Astley. S. M. and Gilbert. F. J. (2004), Computer-aided detection in mammography. *Clinical Radiology* 59: pp. 390-399.

Bai. Y, Bernd. S. G, Hosack. J. R, Farris. M. C, Montroy. J. T and Bajaj. J (2003), Hybrid CMOS focal plane array with extended UV and NIR response for space applications, Presented at Spie's 48th Annual Meeting, 3-8 August, San Diego, California

Barroso. R. C, Oliveira. L. F, Castro. C. R. F, Lima. J. C, Braz. D, Lopes. R. T, Droppa. R, Tromba. G, Mancini. L, Zanini. F, Rigon. L and Dreossi. D (2007), Quantitative evaluation of bone-mineral density loss using x-ray coherent

scattering, *Nuclear Instuments and Methods in Physics Research* A 579, pp. 318-321

Batchelar. D. L, Davidson. M. T. M , Dabrowski. W and Cunningham. I. A (2006), Bone-composition imaging using coherent-scatter computed tomography: assessing bone health beyond bone mineral density, *Med. Phys*. 33 (4), pp. 904-915

Baum. F, Fiscer. U, Obenauer. S and Grabbe. E (2002), Computer-aided detection in direct digital full-field mammography: initial results. *Eur Radiol* 12: pp. 3015-3017

Belev. G and Kasap. S. O (2004), Amorphous selenium as an X-ray photoconductor. *Journal of Non-Crystalline solids* 345 & 346, pp. 484-488

Berns. E. A, R .E. Hendrick and Cutter. G. R (2002), Performance comparison of full-field digital mammography to screen-film mammography in clinical practice. *Med. Phys*. 29(5): pp. 830-834

Berns. E. A, R .E. Hendrick and Cutter. G. R (2003), Optimization of technique factors for a silicon diode array full-field digital mammography system and comparison to screen-film mammography with matched average glandular dose. *Med. Phys*. 30(3): pp. 334-340

Beutel. J, Kundel. H. L, Van Metter. R. L (2000), Handbook of Medical Imaging volume 1. Physics and psychophysics, Vol. 1, pp. 187-189, *SPIE Press*, Bellingham, Washington

Bigas. M, Cabruja. E, Forest. J and Salvi. J (2006), Review of CMOS image sensor. *Microelctronics Journal* 37 pp. 433-451

Bohndiek. S. E, Cook. E. J, Arvanitis. C. D, Olivo. A, Royle. G. J, Clark. A. T, Prydderch. M. L, Turchetta. R and Speller. R. D (2008), A CMOS active pixel sensor system for laboratory-based x-ray diffraction studies of biological tissue, *Phys. Med. Biol*. 53. pp. 655-672

Bono. C. M and Einhorn. T. A (2003), Overview of osteoporosis: pathophysiology and determinants of bone strength, *Eur Spine* J 12: pp. 90-96

Brandan. M-E and Ramírez-R. V (2006), Evaluation of dual-energy subtraction of digital mammography images under conditions found in a commercial unit, Phys. Med. Biol. 51, pp. 2307-2320

Buonocore. M, Grassi, M and Rufino. G (2005), APS-based miniature sun sensor for earth observation nanosatellites, *Acta Astonautica* 56: pp. 139-145

Castro. C. R. F, Barroso. R. C, Anjos. M. J, Lopes. R. T and Braz. D (2004), Coherent scatter characteristics of normal and pathological breast human tissues, *Radiation Physics and Chemistry* 71, pp. 649-651

Castro. C. R. F, Barroso. R. C, Oliveira. L. F and Lopes. R. T (2005), Coherent scattering x-ray imaging at the Brazilian national synchrotron laboratory: preliminary breast images. *Nuclear Instruments & Methods in Physics Research* A 548, pp. 116-122

Chan. Heang-Ping, Doi. K, Vyborny, Lam. Kwok- Leung and Schmidt. R. A (1988), Computer-aid detection of microcalcifications in mammograms: Methodolgy and preliminary clinical study, *Investigation Radiology* 23:664-671

Changizi. V, Oghabian. M. A, Speller. R, Sarkar. S and Kheradmand. A. A (2005), Application of small angle x-ray scattering (SAXS) for differentiation between normal and cancerous breast tissue, *Int. J. Med. Sci*. 2, pp. 118-121

Cook. E (2008), Private communications

Cooper III. V.N, Oshiro. T, Cagnon. C. H, Bassett. L. W, McLeod-Stockmann. T. M and Bezrukiy. N.V (2003), Evaluation of detector dynamic range in the x-ray exposure domain in mammography: A comparison between film-screen and flat panel detector systems, *Med. Phys*. 30 (10), pp. 2614-2621

Dance. D.R, Klang. A. T, Sandborg. M, Skinner. C. L, Castellano. I. A and Carlsson. G. A (2000), Influence of anode/filter material and tube potential on contrast, signal-to-noise ratio and average absorbed dose in mammography: a monte carlo study. *The British Journal of Radiology* 73: pp. 1056-1067

Dierickx. B, Meynants. G and Scheffer. D (1997), Near 100% fill factor CMOS active pixels, in Proc. IEEE Workshop an CCD's and AIS's, Brugge, Belgium

Dobbins lll. J. T (1995), Effect of undersampling on the proper interpretation of the modulation transfer function, noise power, spectra, and noise equivalent quanta of digital imaging systems. *Med. Phys*. 22(2): pp. 171-181

Dobbins III. J. T, Ergun. D. A, Rutz. L, Hinshaw. D. A, Blume. H and Clark. D. C (1995), DQE(f) of four generations of computed radiography acquisition devices. *Med. Phys*. Vol. 22(10): pp. 1581-1593

Dobbins III. J. T, Samei. E, Ranger. N. T and Chen. Y (2006), Intercomparison of methods for quality characterization. II. Noise power spectrum. *Med. Phys*. Vol. 33(5): pp.1466-1475

Dromain. C, Balleyguier. C, Adler. G, Garbay. J.R and Delaloge. S (2009), Contrast-enhanced digital mammography, *European Journal of Radiography* 69: pp. 34-42

Dromain. C, Balleyguier. C, Muller. S, Mathieu. M-C, Rochard. F, Opolon. P and Sigal. R (2006), Evaluation of tumor angiogenesis of breast carcinoma using contrast enhanced digital mammography, *AJR* 187: pp. 528-537

El Gamal A. and Eltoukhy H (2005), CMOS Image Sensors, *IEEE Circuits & Devices Magazine*, 21 (3), pp. 6–20.

Elbakri. I. A, Lakshminarayanan. A. V. and Tesic. M.M (2005), Automatic exposure control for a slot scanning full field digital mammography system. *Med. Phys*. 32(9): pp. 2763-2770

Elbakri. I. A, McIntosh. B. J and Rickey. D. W (2009), Physical characterization and performance comparison of active- and passive-pixel CMOS detectors for mammography, *Phys, Med. Biol.* 54: pp. 1743-1755

Fahrig. R and Yaffe. M. J (1994), Optimization of spectral shape in digital mammography: Dependence on anode material, breast thickness, and lesion type, *Med. Phys*. 21(9): pp. 1473-1481

Farquharson. M. J, Speller. R. D and Brickley. M (1997), Measuring bone mineral density in archaeological bone using energy dispersive low angle x-ray scatter techniques, *Journal of Archaeological Science* 24: 765-772

Fass. L (2008), Imaging and cancer: A review, *Molecular Oncology* 2, pp. 115-152

Fernandez. B. F (2000), The role of artificial intelligence technologies in the implementation of People-Finder knowledge management systems. *Knowledge-Based Systems* 13: pp. 315-320

Fischer. U, Baum. F, Obenauer. S, Luftner-Nagel. S, Heyden. D. V, Vosshenrich. R and Grabbe. E (2002), Comparative study in patients with microcalcifications: full-field digital mammography vs screen-film mammography. *Eur Radiol* 12: pp. 2679-2683

Fischer. U, Hermann. K. P and Baum. F (2005), Digital mammography: current state and future aspects. *Eur Radiol* 16: 38-44

Fossum E. R. (1997), CMOS Image Sensors: Electronic Camera-On-A-Chip, *IEEE Transactions on Electron Devices* 44 (10), pp. 1689–1698

Freer T. W, Ulissey. M. J (2001), Screening Mammography with Computer-aided Detection: Prospective study of 12,860 Patients in a Community Breast Center. *Radiology* 220: pp. 781-786

Fujita. H, Tsai. D-Y, Itoh. T, Doi. K, Morishita. J, Ueda. Katsuhiko and Ohtsuka. A (1992), A simple Method for Determining the Modulation Transfer Function in Digital Radiography", *IEEE Trans. Med. Imaging, Vol*. 11(1), pp. 34-39

Ge. J, Hadjiiski. L. M, Sahiner. B, Wei. J, Helvie. M. A, Zhou. C and Chan. H. P (2007), Computer-aided detection systems for clustered microcalcifications: comparison of performance on full-field digital mammograms and digitized screen-film mammograms. *Phys. Med*. *Biol*. 52: pp. 981-1000

Ghetti. C, Borrini. A, Ortenzia. O, Rossi, R and Ordóñez, P. L (2008). Physical characteristics of GE Senographe Essential and DS digital mammography detectors. *Med. Phys*. 35 (2): pp. 456-463

Gomi. T, Koshida. K, Miyati. T, Miyagawa. J and Hirano. H (2006), An Experimental Comparison of Flat-panel Detector Performance for Direct and Indirect Systems (Initial Experiences and Physical Evaluation). *Journal of Digital Imaging* 19(4): pp. 362-370

Griffiths J A, Royle G J, Hanby A M, Horrocks J A, Bohndiek S E and Speller R D (2007), Correlation of energy dispersive diffraction signitures and microCT of small breast samples with pathological analysis *Phys. Med. Biol*. 52 pp. 6151-64

Gur. D, Sumkin. J. H, Rockette. H. E, Ganott. M, Hakim. C, Hardesty. L, Poller. W. R, Shah. R, and Wallace. L (2004), Changes in Breast Cancer Detection and Mammography Recall Rates after the introduction of a Computer-Aided Detection System. *Journal of the National Cancer Institute* 96(3): pp. 185-190

Hermann. K. P, Obenauer. S, Funke. M, Grabbe. E. H (2002), Magnification mammography: a comparison of full-field digital mammography and screen-film mammography for the detection of simulated small masses and microcalcifications. *Eur Radiol* 12: pp. 2188-2191

Hoffman. A, Loose. M, and Suntharalingam. V (2006), CMOS Detector Technology, *Experimental Astronomy* 19, pp. 111–134

Hosticka. B. J, Brockherde. W, Bußmann. A, Heimann. T, Jeremis. R, Kemna. A, Nitta. C and Schrey. O (2003), CMOS imaging for automotive applications. *IEEE transactions on Electronic Devices*, 50 (1), pp, 173-183

Hukins. D. W. L (1983), X-ray Diffraction by Disordered and Ordered Systems, Butterworths, London

I-ImaS (2004), Key clinical requirements of dental and mammographic imaging, Work package 2, Deliverables 6

I-ImaS (2005), Translating information signatures to a sequence of well-defined processing functions. *Work package 3, Deliverable 8*

I-ImaS (2006), Intelliegent Imaging System, Work package 3, Deliverables 27

James. J. J (2004), The current status of digital mammography, *Clinical Radiology* 59, pp. 1-10

Janesick. J, Gunawan. F, Dosluoglu. T, Tower. J, and McCaffrey (2003), SCIENTIFIC CMOS PIXELS, *Experimental Astronomy* 14: pp. 33-43, Kluwer Academic Publisher

Janesick. J, and Putnam. G (2003), Development and application of high performance CCD and CMOS imaging arrays. *Annu. Rev. Nucl. Part. Sci.* 53**:** pp. 263-300

Johns. H. E. and Cunningham. J.R (1983), The Physics of Radiology, 4th ed, pp. 261-263, Thomas, Springfield, Illinois

Johns. P. C and Yaffe. M. J (1982), Coherent scatter in diagnostic radiology *Med. Phys*. 10(1), pp. 40-50

Justesen. J, Stenderup. K, Ebbesen. E. N, Mosekilde. L, Steiniche. T and Kassem. M (2001), Adipocyte tissue volume in bone marrow is increased with aging and in patients with osteoporosis, *Biogerontology 2*: pp. 165-171

Kandarakis. I, Cavouras. D, Panyiotakis. G. S, Triantis. D and Nomicos. C. D (1997), An experimental method for the determination of spatial-frequency=dependant detective quantum efficiency (DQE) of scintillators used in X-ray imaging detectors. *Nuclear Instruments & Methods in Physics Research* A 399, pp. 335-342

Kappadath. S. C and Shaw. C. C (2004), Quantitative evaluation of dual-energy digital mammography for calcification imaging. *Phys. Med. Biol*. 49: pp. 2563-2576

Kazantzi. A, Radiologist, Private communications.

KCARE, Comparative specifications of full field digital mammography systems (2005), Report 05037, www.mhra.gov.uk

Kidane. G, Speller. R. D, Royle. G. J and Hanby. A. M (1999), X-ray scatter signatures for normal and neoplastic breast tissues, *Phys. Med. Biol.* Vol. 44, pp. 1791-1802

Ko. J. M, Nicholas. M. J, Mendel. J. B and Slanetz. P. J (2006), Prospective Assessment of Computer-Aided Detection in Interpretation of Screening Mammography. *AJR* 187: pp. 1483-1491

Kosanetzky. J, Knoerr. B, Harding. G and Neitzel. U (1987), X-ray diffraction measurements of some plastic materials and body tissues. *Phys. Med.* Vol. 14(4). pp. 526-532

Lauria. A, Palmiero. R, Forni. G, Fantacci. M. E, Imbriaco. M, sodano. A, Indovina. P. I (2005), A study for two different CAD systems for mammography as an aid to radiological diagnosis in the search of microcalcification clusters. *European Journal of Radiology* 55: pp. 264-29

Lemacks. M. R, Kappadath. C, Shaw. C. C, Liu. X and Whitman. G. J (2002), A dual-energy subtraction technique for microcalcification imaging in digital mammography–A signal-to-noise analysis, *Med. Phys*. 29(8), pp. 1739-1751

Lewin. J. M, D'Orsi. C. J, Hendrick. R. E, Moss. L. J, Isaacs. P. K, Karellas. A and Cuter. G. R (2002), Clinical comparison of full-field digital mammography and

screen- film mammography for detection of breast cancer, *AJR*: 179: pp. 671-677

Lewin. J. M, Hendrick. R. D, D'Oris. C. J, Isaacs. P. K, Moss. L. J, Karellas. A, Sisney. G. A, Kuni. C. C and Cutter. G. R (2001), Comparison of Full-Field Digital Mammography with Screen-Film Mammography for Cancer Detection: Results of 4,945 Paired Examinations. *Radiology* 218, pp. 873-880

Luggar. R. D, Horrocks. J. A, Speller. R. D and Lacey. R. J (1996), Determination of the geometric blurring of an energy dispersive X-ray diffraction (EDXRD) system and its use in the simulation of experimentally derived diffraction profiles. *Nuclear Instruments & Methods in Physics Research* A 383, pp. 610-618.

Malich. A, Fischer. D. R and Böttcher. J (2006), CAD for mammography: the technique, results, current role and further development. *Eur Radiol* 16: pp. 1449-1460

Marx. C, Malich. A, Facius. M, Grebenstein. U, Sauner. D, Pfleiderer. S. O. R and Kaiser. W. A (2003), Are unnecessary follow-up procedures induced by computer-aided diagnosis (CAD) in mammography? Comparison of mammographic diagnosis with and without use of CAD. *European Journal of Radiology* 51: pp. 66-72

Meeson. S, Young. K. C, Ramsdale. M. L, Wallis. M. G and Cooke. J (1999), Analysis of optical density and contrast in mammograms, *The British Journal of Radiography* 72: pp. 670-677

Meyer. P, Buffard. E, Mertz. L, Kennel. Constantinesco. A and Siffert. P (2004), Evaluation of the use of six diagnostic x-ray spectra computer codes, *The British Journal of Radiology*, 77 pp. 224-230

Monnin. P, Gutierrez. D, Bulling. S, Guntern. D and Verdun. F. R (2007), A comparison of the performance of digital mammography systems, *Med. Phys.* 34 (3), pp. 906-914

Morton. M. J, Whaley. D. H. W, Brandt. K. R and Amrami. K. K (2006), Screening Mammograms: Interpretation with Computer-aided detection – Prospective evaluation. *Radiology* 239: pp. 375-383

National Health Service Breast Screening Programme (NHSBSP), accessed 2009, (http://www.cancerscreening.nhs.uk/breastscreen/)

Newton. M, Hukins. D. W. L, and Harding. G (1992), Bone composition measured by x-ray scattering, *Phys. Med. Biol*. 37, pp. 1339-1347

Nikl. M (2006), Scintillation detectors for x-rays, *Meas. Sci. Technol*, 17 R37-R54

Nishikawa. R. M (2007), Current and future directions of computer-aided diagnosis in mammography. *Computerized Medical Imaging and Graphics* 31: pp. 224-235

Nishikawa. R. M and Yaffe. M. J (1990), Model of the spatial-frequency detective quantum efficiency of phosphor screens. *Med. Phys*. 17(5): pp. 894-903

Nowotny R. and Hvfer A. (1985), 'Ein Program fur die Berechung von diagnostischen Roentgnespektren'. Fortschr Roentegenstr 142, pp. 685-689.

Obenauer. S, Hermann. K. P, Marten. K, Luftner-Nagel. S, Heyden. D. V, Skaane. P and Grabbe. E (2003), Soft Copy verse Hard Copy Reading in Digital Mammography. *Journal of Digital Imaging* 16(4): pp. 341-344

Obenauer. S, Luftner-Nagel. S, Heyden. D. V, Munzel. U, Baum. F and Grabbe. E (2002), Screening film vs. full-field digital mammography: image quality, detectability and characterization of lesions. *Eur Radiol* 12, pp. 1697-1702

Parikh. J (2005), Digital mammography: current capabilities and obstacles, *J Am Coll Radiol* (2) 9, pp. 759-767

Pisano. E.D and M. J. Yaffe (2005), State of the Art: Digital Mammography. *Radiology* 234: pp.353-363

Pisano. E. D, Gatsonis. C, Hendrick. E, Yaffe. M, Baum. J. K, Acharyya. S, Conant. E. F, Fajardo. L. L, Bassett. L, D'Orsi. C, Jong. R and Rebner. M (2005), Diagnostic performance of digital verses film mammography for breast-cancer screening, *N Engl J Med*, 353: pp. 1773-1783

Planmed, accessed 27 January 2008, (http://www.planmed.com)

Poletti. M. E, Goncalves. O. D and Mazzaro. I (2002), X-ray scatter from human breast tissue and breast-equivalent materials. *Phys. Med. Biol*. 47, pp. 47-63

Rangayyan. R. M, Ayres. F. J and Desautels. J. E. L (2006), A review of computer-aided diagnosis of breast cancer: Toward the detection of subtle signs. *Journal of the Franklin Institute* 344: pp. 312-348

Reiser. I, Nishikawa. R. M, Giger. M. L, Rafferty. T. W. E. A, Moore. R and Kopans. D. B (2006), Computerized mass detection for digital breast tomosynthesis directly from the projection images. *Med. Phys*. 33(2):pp. 482-491

Royle. G. J and Speller. R. D (1991), Low angle x-ray scattering for bone analysis. *Phys. Med. Biol* 36, pp. 383-389.

Royle. G. J, Farguharson. M, Speller. R.D, and Kidane. G (1999), Application of X-ray diffraction analysis in crystalline and amorphous body tissue. *Radiation Physics and Chemistry* 56, pp. 247-258

Ryan. E. A and Farquharson. M. J (2007), Breast tissue classification using x-ray scattering measurements and multivariate data analysis, *Phys. Med. Biol*. 52, pp. 6679-6696

Samei. E (2003), Imaging quality in two phosphor-based flat panel digital detectors. *Med. Phys*. Vol. 30(7): pp. 1747-1757

Samei. E and Flynn. M. J (2003), An experimental comparison of detector performance for direct and indirect radiography systems. *Med.Phys*. 30(4): pp. 608-622

Sandini. G, Questa. P, Scheffer. D, Dierickx. B and Mannucci. A (2000), Proc. of *IEEE Sensor Array and Multichannel Processing Workshop*, pp. 514-519

Schanz. M, Nitta. C, Bußmann. A, Hosticka. B. J and Wertheimer. R. K (2000), A high-dynamic-range CMOS image sensor for automotive applications, *IEEE Journel of Solid-State Circuits*, 35 (7), pp. 932-938

Schwarz. M, Hauschild. R, Hosticka. B. J, Huppertz, J, Kneip. T, Kolnsberg. S, Ewe. Lutz and Trieu. H. K (1999), Single-chip CMOS image sensors for retina implant system. *IEEE Transaction on Circuit and Systems* 2: Analog and digital processing, 46 (7), pp. 870-877

Sechopoulos. I and Ghetti (2009), Optimization of the acquisition geometry in digital tomosynthesis of the breast, *Med. Phys*. 36 (4), pp. 1199-1207

Sechopoulos. I, Suryanarayanan. S, Vedantham. S, D'Orsi and Kerellas. A (2007), Computation of the glandular radiation dose in digital tomosynethesis of the breast*, Med. Phys*. 34 (1), pp. 221-232

Siemens Health care, Electronic source accessed 27 January 2008, (http://www.medical.siemens.com)

Siewerdsen. J. H, Antonuk. L. E, El-Mohri. Y, Yorkston. J, Huang. W and Cunningham. I. A (1998), Signal, noise power spectrum, and detective quantum efficiency of indirect-detection flat-panel imagers for diagnosis radiology. *Med. Phys*. Vol. 25(5), pp. 614-628

Skaane. P and Skjennald. A (2004), Screen-film mammography verse full-field digital mammography with soft-copy reading: randomized trial in a

population-based screening program – the Oslo II study, *Radiology*, 232:197-204

Smith. G. E and Boyle. W. S (1970), Charge-coupled semiconductor devices. *Bell Syst. Tech. J*, 49: pp. 587-593

Speller. R. D (1999), Tissue Analysis Using X-Ray Scatter, *X-Ray Spectrom*. 28, pp. 244-250

Speller. R. D and Horrocks. J. A (1990), Photon scattering- a 'new' source of information in medicine and biology?, *Phys. Med. Biol*. Vol. 36, pp. 1-6

Stone. M. F, Zhao. W, Jacak. B.V, O'conner. P, Yu. B and Rehak. P (2002), The x-ray sensitivity of amorphous selenium for mammography. *Med. Phys*. 29(3): 319-324

Suckling. J et al (1994), The Mammographic Image Analysis Society Digital Mammogram Database" Exerpta Medica. International Congress Series 1069: pp. 375-378.

Taibi. A, Fabbri. S, Baldelli. P, di Maggio. C, Gennaro. G, Marziani. M, Tuffanelli. A and Gambaccini. M (2003), Dual-energy imaging in full-field digital mammography: a phantom study. *Med. Phys. Biol*. 48: pp. 1945-1956

Theodorakou. C and Farquharson. M. J (2008), Human soft tissue analysis using x-ray or gamma-ray techniques. *Phys. Med. Biol.* 53, R111-R149

Turchetta. R, Fant. A, Gasiorek. P, Esbrand. C, Griffiths. J. A, Metaxas. M. G, Royle. G. J, Speller. R. D, Venanzi. C, van der Stelt. P. F, Verheij. H, Li. G, Theodoridis. S, Georgiou. H, Cavouras. D, Hall. G, Noy. M, Jones. J, Leaver. J, Machin. D, Greenwood. S, Khaleeq. M, Schulerud. H, Østby. J, Triantis. F, Asimidis. A, Bolanakis. D, Manthos. N, Longo. R, Bergamaschi. A (2007), CMOS Monolithic Active Pixels Sensors (MAPS): developments and future outlooks", *Nuclear Instruments and Methods in Physics Research* A, Vol. 582(3), pp. 866-870

Turchetta. R, Fant. A, Gasiorek. P, Esbrand. C, Griffiths. J. A, Metaxas. M. G, Royle. G. J, Speller. R. D, Venanzi. C, van der Stelt. P. F, Verheij. H, Li. G, Theodoridis. S, Georgiou. H, Cavouras. D, Hall. G, Noy. M, Jones. J, Leaver. J, Machin. D, Greenwood. S, Khaleeq. M, Schulerud. H, Østby. J, Triantis. F, Asimidis. A, Bolanakis. D, Manthos. N, Longo. R, Bergamaschi. A (2007), A 1 ½ D CMOS Image Sensor for X-ray imaging, Proc. of 2007 International Image Sensor Workshop, 573, pp. 27-29

Vedantham. S, Karellas. A, Suryanarayanan. S, Albagli. D, Hun. S, Tkaczyk. E. J, Landberg. C. E, Granfors. P. R, Levis. I, D'Orsi. C. J and Hendrick. R. E (2000), Full breast digital mammography with an amorphous silicon-based flat panel detector: Physical characteristics of a clinical prototype. *Med. Phys.* 27(3): pp. 558-567

Vigeland. E, Klaasen. H, Klingen. T. A, Hofvind. S and Skaane. P (2007), Full-field digital mammography compared to screen film mammography in the prevalent round of a population-based screening programme: the Vestfold County Study*. Eur Radiol* 18. pp. 183-191

Vyborny. C. J and Giger. M. L (1994), Computer vision and artificial intelligence in mammography, *AJR* 162: pp. 699-708

Weckler. G (1967), Operation of p-n Junction Photodetectors in a Photon Flux Integrating Model, *IEEE Journal of Solid-State Circuits* 2(3), pp. 65–73

Wei. J, Sahiner. b, Hadjiiski. L. M, Chan. H. P, Petrick. N, Helvie. M. A, Roubidoux. M. A, Ge. J and Zhou. C (2005), Computer-aided detection of breast masses on full field digital mammograms. *Med. Phys* 32(9): pp. 2827-2838

White. D, R and Tucker. A, K (1980), A test object for assessing image quality in mammography. *British Journal of Radiology*. 53:331-335

Williams. M. B, Mangiafico.P . A and Simoni. P. U (1999), Noise power spectra of images from digital mammography detectors. *Med. Phys*. Vol. 26(7): 1279-1293

Williams. M. B, Raghunathan. P, More. M. J, Seibert. J. A, Kwan. A, Lo. J. Y, Samei. E, Ranger. N. T, Fajardo. L. L, McGruder. A, McGruder. S. M, Maidment, A. D. A, Yaffe. M. J, Bloomquist. A and Mawdsley. G. E (2008), Optimisation of exposure parameters in full field digtal mammography. *Med. Phys*. 35(6): pp. 2414-2423

Yadid-Pecht. O and Etienne-Cummings. R (2004), CMOS imagers: From phototransduction to image processing, Kluwer Academic Publisher, Boston

Yamada. T (2003), Comparison of Screen-film and Full-field Digital mammography: Image Contrast and Lesion Characterization. *Radiation Medicine*, 21 (4), pp. 166-171

Young. K. C (2006), Recent developments in digital mammography. *The British Institute of Radiology* 18(2): pp. 68-74

Young. K. C, Oduko. J. M, Bosmans. H, Nijs. K and Martinez. L (2006), Optimal beam quality selection in digital mammography. *British Journal of Radiology*. 79: pp. 981-990

Young. K. C, Ramsdale. M. L and Rust. A (1996), Dose and image quality in mammography with an automatic beam quality system. *British Journal of Radiology*, 69(822): pp. 555-562

Young. K. C, Ramsdale. M. L, Rust. A and Cooke. J (1997), Effect of automatic kV selection on dose and contrast for a mammographic X-ray system. *British Journal of Radiology.* 70: pp. 1036-1042

Zhao. W, Belvis. I, Germann. S, Rowland. J. A, Waechter. D and Huang. Z (1997), Digital radiology using active matrix readout of amorphous selenium: Construction and evaluation of a prototype real-time detector. *Med. Phys.* 24(12): pp. 1834-1843